University of Zurich[UZH]

Characterization of the Novel Hamamatsu R12699-406-M4 2" Photomultiplier Tube in Xenon for the DARWIN Experiment

Master Thesis in Physics

Maximinio Adrover

Supervised by
Prof. Dr. Laura Baudis
Alexander Bismark

November 29, 2023

Abstract

In preparation for the future DARWIN dark matter observatory, an in-depth study of a candidate photosensor is performed. The sensors selected will be employed in a xenon-based two-phase time projection chamber (TPC) and must be able to operate at cryogenic temperatures down to $-100\,^{\circ}\mathrm{C}$ and under high pressures of up to 3 bar while being submerged in liquid xenon. This thesis presents a characterization of eight units of the novel Hamamatsu R12699-406-M4 flat panel multianode photomultiplier tubes (PMT) in realistic experimental conditions. The instrument distinguishes itself from competing models by its compact form factor, multianode read-out capability, and quick signal response. Three different data acquisition campaigns were performed in the PMT testing facility MarmotX at the University of Zurich, to gauge the sensors' performance in vacuum at room temperature, as well as in gaseous and liquid xenon at a temperature of 174 K and a pressure of 1.8 bar. The single photoelectron response was extracted with two independent methods and amounts to a gain of $(3.22 \pm 0.65) \times 10^6$ and a resolution of $(31.3 \pm 4.5)\,\%$ in liquid xenon. The dark current estimate yielded a dark count rate of $(0.47 \pm 0.25)\,\mathrm{Hz\,cm^{-2}}$ recorded in the gas phase. The afterpulse rate, recorded with the PMTs submerged in liquid xenon, is $(1.11 \pm 0.54)\,\%$/PE. To further demonstrate the applicability of the instruments in xenon-based detectors, a kg-scale two-phase TPC was designed specifically to fit all eight units of the R12699-406-M4 tubes inside the MarmotX facility.

Contents

1 Introduction

The work presented in this thesis aims to contribute to an ongoing global effort to determine the properties of an elusive form of matter, discovered over the course of the past century. A number of independent astrophysical observations at various scales have led to the conclusion that the majority of matter present in the universe is in fact *dark*, meaning that it does not interact with light, or, if it does, only extremely weakly. Attempts to modify Newtonian dynamics to accommodate these observations so far fell short of consistently reproducing them at all relevant scales. Further motivation arises from the requirements of the standard models of cosmology and particle physics. The former is contingent on a large amount of non-baryonic mass in the early universe, in order for the matter to collapse into the pronounced structures observed today. The latter is currently under scrutiny, owing to a number of inconsistencies, such as the discovery of neutrino oscillations, implying that the massless standard model neutrinos are in fact massive, and the so-called hierarchy problem, entailing precise cancellations of corrections to the Higgs mass spanning multiple orders of magnitudes to arrive at the measured mass of the Higgs boson. One solution to the hierarchy problem states that the standard model of particle physics in its current state is but a low-energy limit of a more general theory. Various proposed extensions postulate new species of fundamental particles, providing an independently motivated source of candidates for this unknown form of matter.

Experiments all over the world are dedicated to probing the parameter space of *dark matter*, employing different techniques and approaches. One particular approach involves the use of liquid xenon as a target material for radiation detection. Its scintillating properties are exploited in two-phase time projection chambers, a type of detector with the goal of observing direct interactions of dark matter particles with the xenon target. The DARWIN experiment will employ such a detector with an active liquid xenon mass of 40 t. The scale of this project is unprecedented and requires an extensive R&D campaign. The work presented here is within the scope of this campaign and aims to provide a characterization of a light sensor, the Hamamatsu R12699-406-M4 multianode photomultiplier tube, which is considered as a candidate for the time projection chamber at the core of the DARWIN experiment. The feasibility of the sensor hinges on its performance in conditions prevailing in the actual experiment. These include cryogenic temperatures as low as 174 K, pressures up to 3 bar, and being submerged in gaseous and liquid xenon. To gauge the performance of the R12699 tube in these conditions, eight units were thoroughly tested in the PMT testing facility MarmotX at the University of Zurich. MarmotX includes a cryostat, able to stably contain > 10 kg of liquefied xenon. Three characterization campaigns were performed, testing four tubes at a time, in conditions mimicking the xenon-based two-phase TPC environment, i.e. at cryogenic temperatures as low as $-100\,^{\circ}$C and pressures up to 2 bar. In addition, the tubes are to be employed in a kg-scale detector designed for the MarmotX facility, as a proof of concept, and to further study their performance in actual TPC application.

The thesis is structured as follows: After a brief elaboration on the motivations for dark matter arising from the standard model of particle physics and the current cosmological paradigm in the following paragraphs, a compilation of compelling evidence for its existence, of candidate particles and experimental approaches toward their detection is laid out in Chapter 2. In Chapter 3, a description of the basic principles of xenon-based two-phase time projection chambers is presented, as well as an introduction to the scale and scope of the future DARWIN experiment. The working principle and characteristic properties of photomultiplier tubes are described in Chapter 4, followed by an introduction to the Hamamatsu R12699-406-M4 photomultiplier tube and why it makes for an interesting candidate. The various systems of the MarmotX facility are compiled in Chapter 5. Finally, the analysis approach and results are presented in Chapter 6,

before the thesis concludes in the discussion in Chapter 7.

The Standard Model of Particle Physics

The Standard Model of particle physics (SM) describes the constituents and interactions of what to date are known as fundamental particles. The fundamental constituents of matter are fermions that are characterized by their half-odd-integer spin. The interactions are mediated by integer spin particles, referred to as gauge bosons, each of which is associated with one of the fundamental forces. Gluons mediate the strong force, and the photon γ, $W^{\pm}$, Z^0, and the Higgs boson H mediate the electroweak interaction.

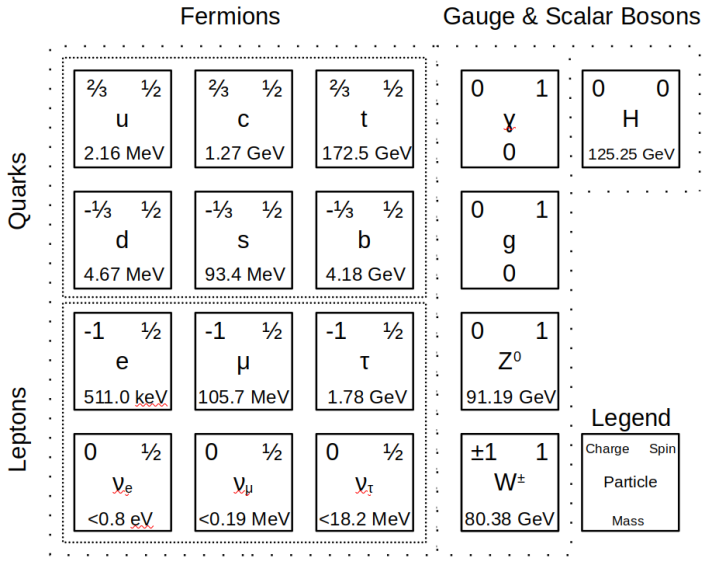

Figure 1: The constituents of the Standard Model of particle physics. Particle properties from [1]

The fermions are further subdivided into quarks that interact with all the known force carriers, and the leptons that are excluded from the strong interaction. Both families feature three generations of particle pairs, indicated by the columns in figure 1. The forces arise directly from the requirement of invariance under local gauge transformations. The underlying symmetry being

$$SU(3)_C \otimes SU(2)_L \otimes U(1)_Y \rightarrow SU(3)_C \otimes U(1)_Q \tag{1}$$

where Y denotes the weak hypercharge, Q the electric charge, and $SU(3)_C$ the underlying symmetry of the strong interaction, associated to the color charge C inherent to the quarks and the gluons. The arrow indicates the spontaneous breaking of the $SU(2)_L \otimes U(1)_Y$ symmetry that results in the generation of the massive $W^{\pm}$, Z^0 and Higgs field [2], and allows the inclusion of gauge invariant mass terms into the Standard Model Lagrangian. The spontaneous symmetry breaking thus introduces a mechanism to generate masses for the massive bosons, as well as the fermions, with the exception of the neutrinos. The latter are excluded owing to the fact that the mass terms include both the left- and right-handed fermion fields. Given that the right-handed neutrino does not partake in the electroweak interaction, neutrinos do not receive a mass term and are therefore massless. The observation of neutrino oscillations [3] however, contradicts this theoretical prediction. The right-handed, or *sterile* neutrinos are now being considered as

candidate particles for dark matter.
The discovery and first measurement of the Higgs in 2012 yielded a mass $m_H \simeq 125\,\mathrm{GeV}$ [4]. Although its discovery is celebrated as one of the greatest advancements in particle physics to date, the measured value has puzzled scientists ever since. It is in stark contrast with a fundamental pretense of *naturalness*, i.e. an aesthetic property of a theory requiring the ratios of fundamental free parameters to be consistent with unity, which is at the core of most theories. In theoretical predictions, the Higgs mass is subject to correction terms from its interaction with virtual particles. The scale of the correction is determined by the energy available to these virtual particle pairs. In principle we would expect this energy to be of the Planck scale, being the limit at which the SM is assumed to break down. The mass available to the Higgs would then be of the order $m_{PL} = \sqrt{\hbar c/G} \sim 10^{18}\,\mathrm{GeV}$. To achieve a mass of $\mathcal{O}(10^2\,\mathrm{GeV})$ the individual corrections over all scales would need to cancel out very precisely merely by accident [5]. This riddle is equivalent to the question of why the electroweak force is so many orders of magnitude stronger than gravity and is commonly referred to as the *hierarchy problem*. It is a strong motivation for extensions to the SM, such as supersymmetric models, where each SM particle receives a supersymmetric partner, spartner for short, with the same set of quantum numbers except for differing spin. The virtual corrections are therefore identical in magnitude but with opposite sign, providing the cancellation required to observe the measured Higgs mass.

Cosmological Paradigm

The widely accepted standard model of cosmology relies on the hot Big Bang scenario, describing the universe as having evolved from a highly compressed state some 10^{10} years ago [2]. This picture is based on the discovery of the cosmological redshift, i.e. the observation that the vast majority of light reaching the earth from celestial bodies experiences a Doppler shift toward larger wavelengths, suggesting an expanding universe.
Einstein's field equations relate the universe's geometry to its matter and energy content. They can be solved by introducing the Riemann-Lemaître-Robertson-Walker (RLRW) metric. One of its components yields the Friedmann equation:

$$\left(\frac{\dot{a}}{a}\right)^2 + \frac{k}{a^2} = \frac{8\pi G_N}{3}\rho_{tot} \tag{2}$$

where G_N is Newton's gravitational constant, $a = a(t)$ is the so-called scale parameter, parametrizing the relative expansion of the universe, ρ_{tot} is the average energy density, and the constant k describes the universe's spatial curvature and can take the values $k = -1, 0, 1$. In the simplest case, i.e. $k = 0$, the universe is said to be *flat* and the spatial term of the RLTW metric assumes the ordinary Euclidean metric. This is the case if the total energy density equals the *critical density*

$$\rho_c = \frac{3H^2}{8\pi G_N} \simeq 1.88h^2 \times 10^{-29}\mathrm{g\,cm^{-3}} \tag{3}$$

where the Hubble constant is introduced as $H = \dot{a}/a$. Historically, its present-day value is defined as $H_0 = 100\,h\,\mathrm{km\,s^{-1}\,Mpc^{-1}}$ with the dimensionless *Hubble parameter* $h \leq 1$ [6]. The individual contributions to the energy density, such as the matter and radiation contents, are conventionally expressed in relative abundances $\Omega_i = \rho_i/\rho_c$ such that equation (2) now reads:

$$\Omega - 1 = \frac{k}{H^2 a^2} \tag{4}$$

where $\Omega = \sum_i \Omega_i$.
Furthermore, evidence from distant supernovae suggests that the universe expands at an accelerated rate [7]. This necessitates the inclusion of the cosmological constant Λ in the Einstein and

subsequently, the Friedmann equation, which acts as an addition to the overall energy budget in the form of dark energy. Its temporal independence suggests that it takes the form of a vacuum energy. Current models, however, fail to quantify it in a manner consistent with observation [6].
The last element mentioned in this work is the inclusion of *cold* dark matter as the main contribution to the relative abundance of matter in the universe. The designation 'cold' relates to the non-relativistic velocity distribution of this matter constituent in the early universe that would allow structure formation as is observed today.
The above broadly illustrated components are part of the contemporary concordance model of cosmology, dubbed ΛCDM, characterized by a flat ($k = 0$) universe with a cold dark matter dominated matter content and accelerated expansion.

2 The Case for Dark Matter

In his famous article from 1933, Fritz Zwicky made use of the then newly discovered method to determine the distances and relative velocities of galaxies via their apparent Redshift [8]. His observations of the Coma Cluster resulted in a vast velocity dispersion of at least $1500\,\mathrm{km\,s^{-1}}$ to $2000\,\mathrm{km\,s^{-1}}$ among the constituent galaxies, which Zwicky showed by applying the virial theorem to be exceeding the escape velocity of the system by an order of magnitude. He took this as an indication that the gravitational attraction experienced by the galaxies within the cluster cannot be solely due to their luminous mass and coined the term *"Dunkle Materie"*, referring to an additional massive but invisible component. About three decades later, further evidence started to accumulate, cementing Zwicky's conjecture into today's prevalent paradigm.

2.1 Galactic Rotation Curves

On a galactic scale astronomers Vera Rubin and William K. Ford observed a discrepancy with classical Newtonian dynamics in the velocity distributions of stars in NGC 224 [9], commonly known as the Andromeda galaxy. In the late 60s, Rubin and Wilson were able to determine the orbital velocity of its H II emission regions, from their Hα emission lines [1], and map them against the distance to the galactic center. Figure 2 shows a collection of rotation curves formed from their data. The striking feature of all these curves is the evident flattening at distances greater than 8 kpc. From Newtonian dynamics, we would expect the centripetal force of these objects to be equal to the gravitational force they experience due to the mass enclosed in their orbits. The resulting radial velocity reads

$$v = \sqrt{\frac{GM(R)}{R}} \tag{5}$$

where R denotes the distance to center and $M(R)$ refers to the enclosed mass at distance R. For large enough distances, where the predominant majority of the visible mass leis within the orbit, we expect the mass profile to flatten out, i.e. $M(R) \sim const.$, and therefore the radial velocity to drop asymptotically or $v \propto 1/\sqrt{R}$. What Rubin and Ford observed however are, as Zwicky decades before, velocities far exceeding the galaxy's escape velocity if one were to only consider Andromeda's luminous mass, i.e. the matter that interacts electromagnetically.
The mass profile inferred from the rotation curves, however, increases linearly with distance. This is understood in equation 5 when requiring that for $R > 8\,\mathrm{kpc}$ the radial velocity remains constant. For this to hold true the radial dependence of the mass profile must cancel with inverse dependence in v, such that $M(R) \propto R$. This is in stark contrast with the observed distribution of matter. The conclusion that has come to be largely accepted by the scientific community is that in addition to the matter we observe, there is another contribution from an as of yet unknown form of matter, that does not interact electromagnetically (or in any other way except through gravitational effects as far as we know) and is hence only tangible through its effects on *tracers*, meaning objects that are expected to behave in a comparable fashion, i.e. are collision-less and interact mainly through gravity. This role is usually played by stars, as is the case in this example. Galaxies however can also fulfill these requirements, as will be discussed in the following.

[1] The term H II denotes interstellar, luminous dust clouds made up of hydrogen (H), where star formation has recently started. The suffix II indicates that parts of the constituent hydrogen atoms of the cloud are singly ionized. The Hα emission line corresponds to the first spectral line in the Balmer series, describing hydrogen emissions in the visible spectrum.

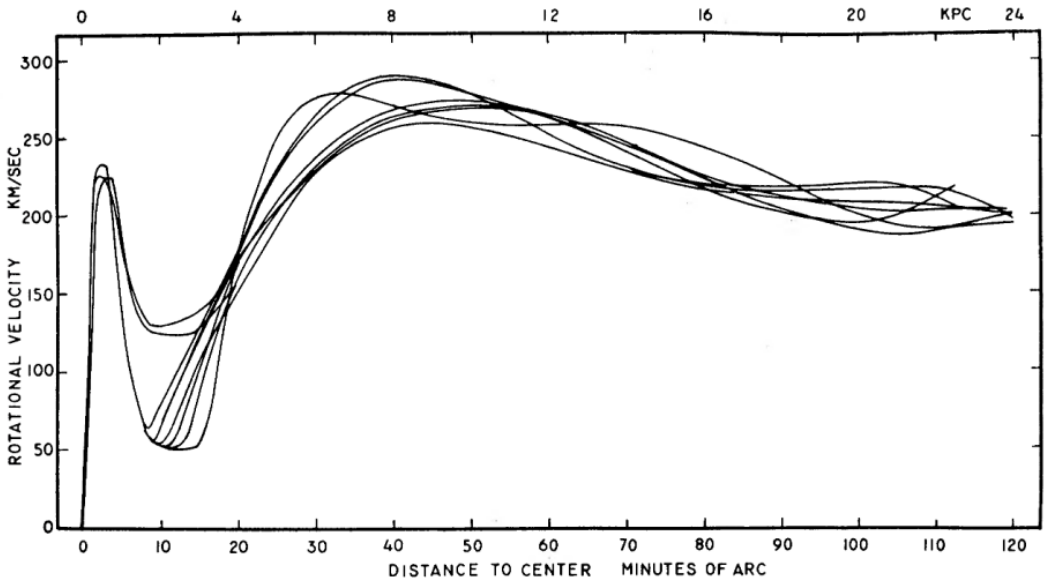

Figure 2: Rotation Curves of M31 illustrating the flattening of the rotational velocities for radii $\geq 8\,\mathrm{kpc}$. Figure from [9]

2.2 The Bullet Cluster

The strongest evidence for dark matter on extragalactic scales comes from the observation of galaxy cluster mergers [10, 11]. Both arguments presented so far hinge on some general assumptions of isotropy and thermal equilibrium. There are some alternatives in describing these phenomena. Most notable is the concept that the Newtonian laws of gravity need adapting at large distances. This concept is usually referred to as MOdified Newtonian Dynamics (or MOND), which manages to recreate the flattening of rotational curves, without the need for a hidden mass assumption [12]. While the general discussion hasn't yet met its conclusion, the following evidence tips the scale in favor of the dark matter hypothesis, because it does no longer rely on the above base assumptions [13].
The observations made on galaxy cluster 1E 0657-558, commonly referred to as the bullet cluster, are based on the concept of weak gravitational lensing. Although dark matter does not directly interact with light, it can affect its path via its gravitating mass. One consequence of Einstein's theory of general relativity is the warping of space-time in the presence of gravitational fields [14]. This warping results in a bent trajectory of light passing through strong gravitational fields, from the perspective of outside observers, as depicted in figure 3. Large enough masses can then act as a sort of lens, such that the image of distant celestial bodies appears magnified, diminished, or generally warped, depending on the lensing mass. Gravitational lensing, in this case, weak lensing specifically, allows astronomers to map the mass distribution of objects via the apparent refraction of luminous bodies in the background. The measurement of weak lensing effects is generally statistical in nature. Because, as the name suggests, its effects are more subtle than, i.e. the very identifiable Einstein Rings (see for example [15]), and any measurement relies on sufficient statistics. As an example consider the orientations of distant galaxies. It can be assumed that their major axes' orientations are randomly distributed. Any coherent alignment then indicates the presence of a lensing mass along the line of sight [16]. The alignment arises through optical distortion, or shear, of the background images. This shear can then be mapped over an object of interest, and can, in a next step, be directly related to the responsible gravitational potential. In Figure 4 a map is shown of the bullet cluster's shear-fields (green

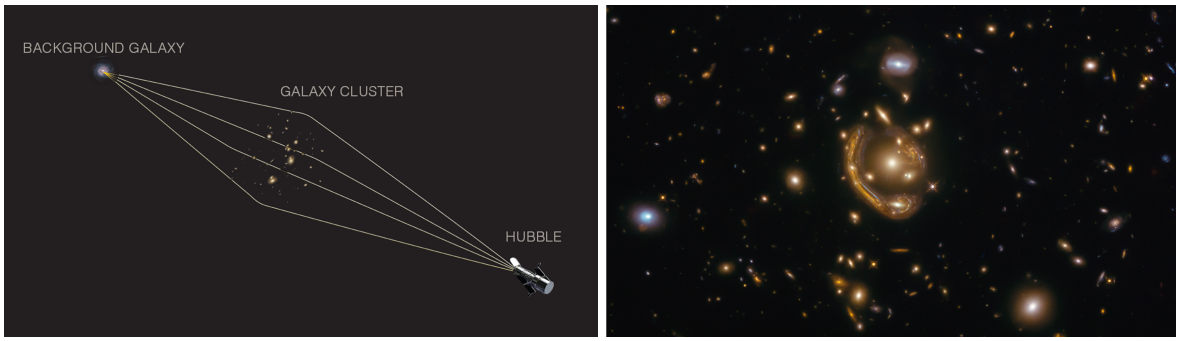

(a) (b)

Figure 3: Illustration of gravitational lensing. (a) The light from a background galaxy is deflected by a massive object creating either multiple images of the same object or warping the image around the foreground object. Image from [17] (b) A partial Einstein ring. Image from [18]

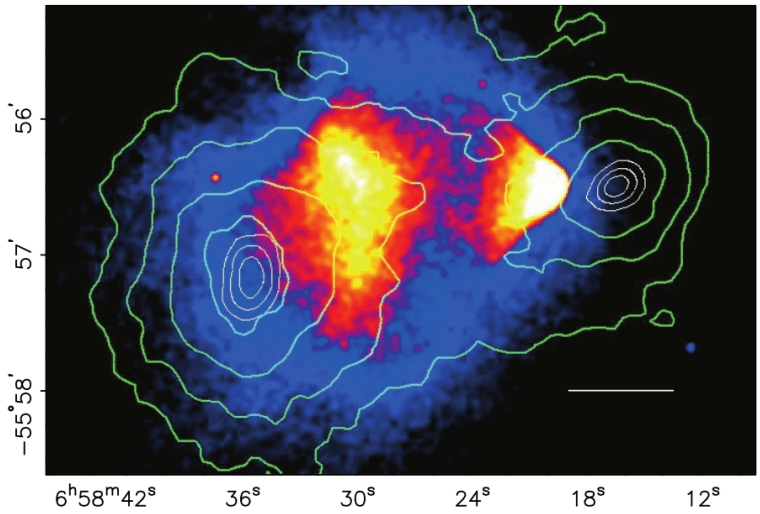

Figure 4: Overlay of the distribution of X-ray emitting gas in shades from blue to white, on the contours of the gravitational well in green of the bullet cluster. The map of the gravitational potential was constructed using weak gravitational lensing. Figure from [13]

contours) with its namesake X-ray emitting gas cloud in shades from blue to white.
The quality of this particular object lies firstly within the circumstance that the merger occurred in our celestial plane, i.e. both galaxy clusters are moving more or less perpendicular to our line of sight, and secondly, the very important fact that the galaxies themselves are collision-less before, during and after the merger, and are therefore suitable tracers for dark matter. The latter statement is not true for the ionized x-ray-emitting gas clouds the clusters carry along with them. During the process they experience ram pressure, giving the cloud on the center-right of the frame its recognizable form. This results in a spatial separation between the bulk of the baryonic mass, i.e. the X-ray gas, and the dark matter, that is expected to follow the path of the galaxies constituting the two clusters. Any model that only accounts for luminous mass, would expect the mass distribution to peak at the intensity maxima of the baryonic bulk. The presented map however clearly exhibits a strong displacement between the plasma and the gravitational potential, placing its peaks towards the centers of the galaxy clusters, where we would expect the dark matter to be [13].

2.3 The Cosmic Microwave Background

In 1965 one of the greatest advancements in cosmology was made purely by accident. Arno Penzias and Robert Wilson, two radio astronomers set out to map the Milky Way's galactic halo with the ground-based Bell's horn-reflector Antenna. In calibrating their instrument they found some noise that they seemingly couldn't get rid of [19]. After various attempts to reduce said noise, which included wiping off pigeon droppings from the inside of the antenna, it was pointed out by George Gamow and his student Ralph Alpher that the excess they had observed might not, in fact, be static noise, but the relic radiation of an early epoch in the universe. In their theory of of nucleus formation [20] there was an epoch in the early universe, of extreme temperature and density. During this stage, the baryonic matter and electromagnetic radiation held each other in thermal equilibrium via Thomson and Coulomb Scattering [21]. Every nucleus formed would immediately be broken apart through ionization. As the universe expanded, however, the temperature decreased. When it dropped to a temperature of the order of $10^4\,\mathrm{K}$ at redshift $z \simeq 1100$ [6], the scattering processes were no longer efficient in maintaining thermal equilibrium. The photons then effectively decoupled, as neutral nuclei were able to form, leaving the former to free-stream into space. This instance is referred to as *recombination*. What Penzias and Wilson then observed was a fragment of the *surface of last scattering*, more commonly known as the Cosmic Microwave Background (CMB), which appears as a close to ideal black body spectrum corresponding to a temperature of $(2.7255 \pm 0.0006)\,\mathrm{K}$ [22].

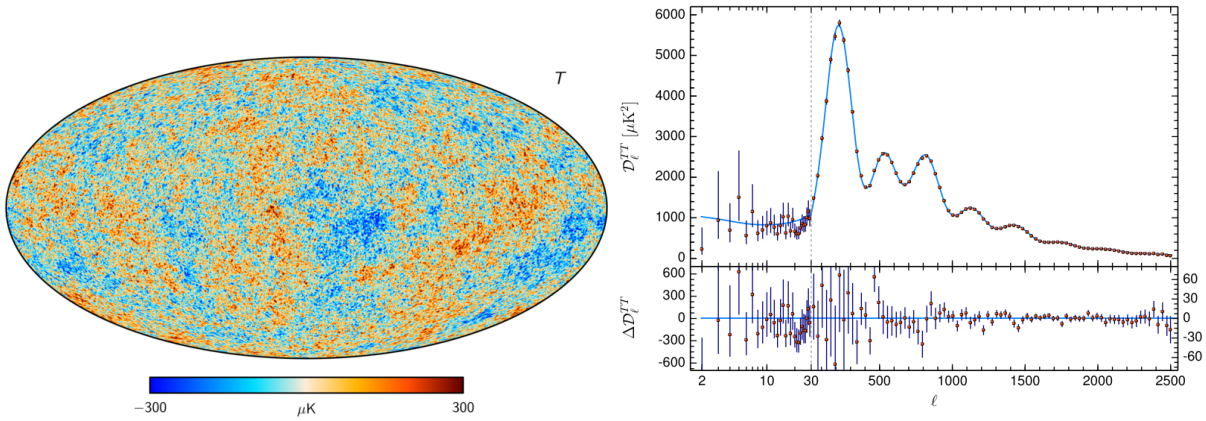

(a) (b)

Figure 5: (a) Full sky map of the cosmic microwave background. The color shading relates to the deviations from the mean black body temperature. Figure from [23] (b) Best fit to the angular scale dependent power spectrum of CMB anisotropies. Recorded by the PLANCK satellite. Figure from [24]

This relic radiation encapsulates information on the shape and dynamics of the photon-baryon fluid at the moment of recombination and is almost perfectly isotropic. The small fluctuations we do observe are of $\mathcal{O}(10^{-4}K)$ and a result of perturbations in the primordial fireball, referring to the hot and dense ion gas before recombination took place. They carry information on key parameters of our current cosmological paradigm. Figure 5a shows a full sky map of the CMB, where the color shades indicate deviations from the mean temperature. Figure 5b illustrates the best fit to the data of the angular scale-dependent power spectrum of temperature fluctuations as measured by the Planck space mission [24]. The individual peaks in the power spectrum carry information about the total energy content of the universe and with it its geometry, and other

key parameters of the ΛCDM model. Most notably for this work the fit yields the following matter contents [24]

$$\Omega_m = 0.321 \pm 0.013, \;\; \Omega_c h^2 = 0.1200 \pm 0.0012, \;\; \Omega_b h^2 = 0.02237 \pm 0.00015$$

where h denotes the dimensionless Hubble constant, as defined in Chapter 1, and the subscripts indicate total m, cold dark matter[2] c and baryonic matter b respectively. Combined with the result that the universe's energy content is roughly equal to the critical density, the above relative abundances indicate that, while matter makes up some 32% of the total energy budget, baryonic mass only accounts for less than $1/5$ of the total matter content. The predominant form of matter appears in the form of cold dark matter and accounts for roughly 85% percent of the universe's total matter content.

2.4 Dark Matter Candidates

Although little is known about the particle properties of dark matter, astrophysical observations, such as the ones mentioned above, allow us to infer some key features. For instance, since DM does not seem to interact with light, the charge of its constituent particles is conjectured to be close to neutral. The strongest constraint comes from the requirement that the DM be completely decoupled from the baryon-photon fluid at the time of recombination. It limits the charge to be no larger than of the order $\mathcal{O}(10^{-7}(m_{DM}/1GeV)^{0.58})\ e$ [25], where e is the charge of the electron. The possible mass range is extensive. It ranges from axion-like objects with masses of the order $\mathcal{O}(10^{-22})$ eV [26] to MAssive Compact Halo Objects (MACHOs) and Primordial Black Holes (PBH) maxing out at $\mathcal{O}(10)M_\odot$ [27, 28]. More details on these proposed DM candidates follow in section 2.4.3. This mass range is somewhat reduced in looking into specific candidates. The approaches in the detection of such candidate particles, outlined in section 2.5, also hinge on a set of core assumptions imposed on the distribution of DM in the universe and more importantly in the immediate vicinity of the earth. Again, the observations made, specifically on galactic scales, allow us to infer key properties of the DM distribution.

2.4.1 Dark Matter in the Milky Way

Considering the linear radial dependency of the mass $M(R) \propto R$ from section 2.1, we can immediately infer a first estimate of the DM density distribution:

$$\rho(r) \sim \frac{M(r)}{r^3} \propto \frac{1}{r^2} \tag{6}$$

Note that the factor $1/r^3$ comes from the assumption of isotropy. This assumption, although too simplistic, is a plausible one, since due to the inert nature of dark matter, it is believed that it has limited means of dissipating energy, unlike its baryonic counterpart, and thus cannot collapse into a disk and therefore forms spherical halos [29]. Applying the virial theorem

$$\langle v \rangle = \sqrt{\frac{2GM_{Halo}}{R_{Halo}}} \tag{7}$$

with estimates for the halo size R_{Halo} and halo mass M_{Halo} consistently yields a mean velocity $\langle v \rangle << c$. If we were to take estimates of the Milky Way's mass $M_{Halo} \sim 10^{12} M_\odot$ and halo size $R_{Halo} \sim 100$ kpc [30] an estimate of the mean velocity of the DM particles according to equation (7) is $\langle v \rangle \sim 200\,\mathrm{km\,s^{-1}}$, motivating the assumption that the bulk of dark matter in

[2] The denomination *cold* stems from the mean of the DM velocity distribution at freeze-out being non-relativistic, cf. section 2.4.2

the universe is non-relativistic. The Standard Halo Model (SHM), which is usually consulted in calculating DM cross sections, assumes a truncated Maxwell distribution in the galactic frame, with an imposed cut-off at the galactic escape velocity [31]:

$$f(v_{gal}) \propto \frac{\rho_\chi}{m_\chi} exp\left(-\frac{|\vec{v}_{gal}|^2}{2\sigma_0^2}\right)\theta(v_{esc} - |\vec{v}_{gal}|) \tag{8}$$

The local density and mass of the DM particles are denoted ρ_χ and m_χ respectively, with standard values of $\rho_\chi = 0.3\,\mathrm{GeV\,cm^{-3}}$ [32] and $v_{esc} = 544\,\mathrm{km\,s^{-1}}$ [33]. This picture, however, ignores effects from departures of the steady-state system, caused for example by galactic mergers, that skew the mean velocity toward larger values. Ongoing merging events, such as the case of the Sagittarius dwarf galaxy being absorbed by the Milky Way [34], affect the DM phase-space distribution. But more sophisticated approaches determining the DM velocity distribution via numerical simulation arrive at comparable conclusions regarding the most probable DM particle velocity [35].

2.4.2 WIMPs

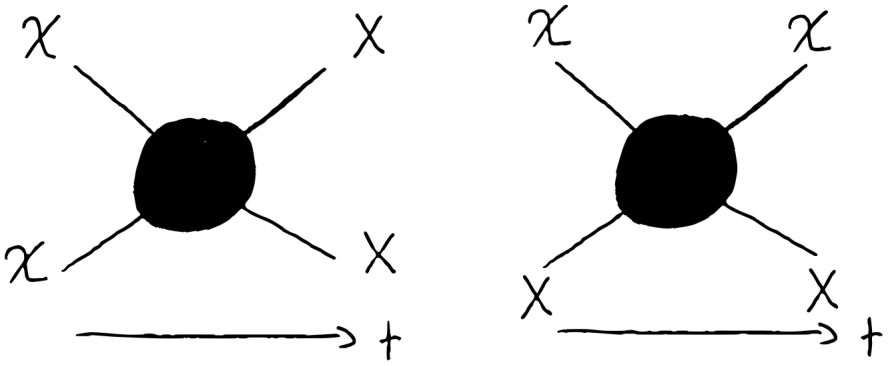

Figure 6: (left) Inelastic scattering process of a dark matter particle pair $\chi\chi$ to SM particles XX. Note that the process also occurs in the inverse direction in t. (right) Elastic scattering of a dark matter particle χ with a SM particle X. The blob in the middle tries to hide the fact that we don't understand the underlying process yet.

In a fashion reminiscent of the decoupling of photons from the photon-baryon fluid, it is conjectured, that DM as well was once in thermal equilibrium with the primordial photon-bath via inelastic scattering of the form presented in figure 6. As long as the rate $\Gamma_{\chi\chi\leftrightarrow XX}$ is greater than the Hubble rate H, thermal equilibrium can be maintained. When $\Gamma << H$ however, the expansion drives the DM particles apart faster than they can annihilate and the process effectively stops. From this point on the relic DM abundance is *frozen*. This proposed course of decoupling is referred to as *freeze-out* in most relevant literature.
An estimate of the relic abundance can be obtained by applying Boltzmann statistics to calculate the freeze-out temperature, i.e. $H(T_f) \sim \Gamma(T_f)$, and equating the comoving number density at freeze-out and today [37]. The abundance Ω_χ obtained for *cold* relics, meaning particles for which the freeze-out temperature is much smaller than the particle mass, results to be a function of the velocity averaged cross section $< \sigma v >$, as indicated by the dashed curves in figure 7. Which in turn is proportional to the ratio of the particle mass and interaction strength squared:

$$\Omega_\chi h^2 \propto < \sigma v > \propto \frac{m_\chi^2}{\alpha^2} \tag{9}$$

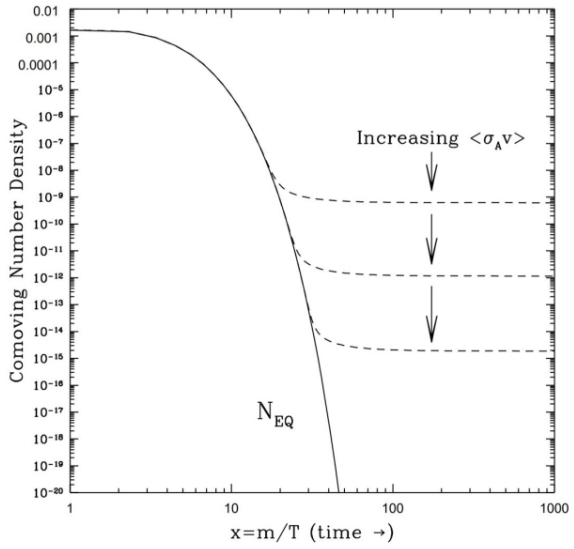

Figure 7: Evolution of the comoving DM number density over time. In an early epoch of the universe, production and annihilation of DM was kept in equilibrium, indicated by the solid line. As the temperature dropped, production became increasingly rare, leading to the exponential drop-off of the equilibrium curve. The expansion, driving DM particles further apart, resulted in a cease of DM annihilation, fixing the abundance to a value depending on the velocity averaged cross section, indicated by the dashed lines. Figure from [36]

The striking thing about this relation is that a particle interacting at the weak-scale with $\alpha \sim 10^{-2}$ and a mass of ∼100 GeV results in a velocity averaged cross section that naturally arrives at roughly the DM abundance observed today by Planck [24]. A particle of this type is referred to as a Weakly Interacting Massive Particle (WIMP). This a priori coincidental relation between weak-scale interactions and cosmological closure, i.e. $k = 0$ in equation (2), suggests that any stable, weak-scale Beyond the Standard Model (BSM) particle can immediately be related to DM [38]. The WIMP miracle, as it is often referred to, has kicked off extensive experimental efforts with promising theoretical groundwork providing a plethora of candidates by various extensions to the SM, such as supersymmetry. It is worth mentioning that these candidates arose independently from the aforementioned quest of a more natural description of particle physics and were not proposed explicitly as possible DM particles. In this sense, supersymmetry was introduced as a solution to the hierarchy problem, but its lightest stable beyond SM particle is considered to be a splendid DM candidate.

2.4.3 Further Candidates

Although the existence of WIMPs is very well motivated and they have been the focus of many research endeavors, no conclusive evidence could be presented so far that proves their existence. It is therefore important to also consider alternatives to the WIMP paradigm.
Many proposed candidates could be excluded with some confidence. MACHOs, such as brown dwarfs and neutron stars, could not be observed in large enough quantities to constitute the required amount of DM in galaxies [39]. Also, they consist of baryons and are to some extent already accounted for in the energy budget as constrained by measurements of the CMB power spectrum. Another popular former candidate came with the discovery of neutrino masses. Neutrinos came to be considered as viable candidates until upper limits on their masses were established since they imply an upper bound on neutrino relic density of $\Omega_\nu h^2 \lesssim 0.07$ [2].

The V-A-structure of the SM weak-interaction leads to a vanishing weak-current contribution of any term in the Lagrangian containing right-handed spinors. This leads to a complete decoupling of right-handed fermions from weak interactions. Since the neutrino can only interact via the exchange of one of the weak $W^{\pm}$ or Z^0 gauge bosons, its right-handed counterpart is virtually non-existent in the SM. These *sterile* neutrinos, being massive, albeit rather light, would only interact gravitationally and through mixing. They constitute promising DM candidates and could also provide insight into the nature of neutrino flavour oscillations and the matter-antimatter asymmetry of the universe [40].
Lastly one of the more popular alternatives to the WIMP paradigm is the ultra-light *axion*, arising from the Peccei and Quinn symmetry that was proposed to solve the strong CP problem[3], and more generally axion-like particles. They are thought to be produced non-thermally, bosonic in nature, and inert enough to constitute suitable DM candidates [41].

2.5 Dark Matter Detection

Figure 8 illustrates the three conceptual DM detection channels that are currently explored in experiments. The blob in the center expresses our ignorance of the exact nature of these processes. The arrows indicate the direction of time.

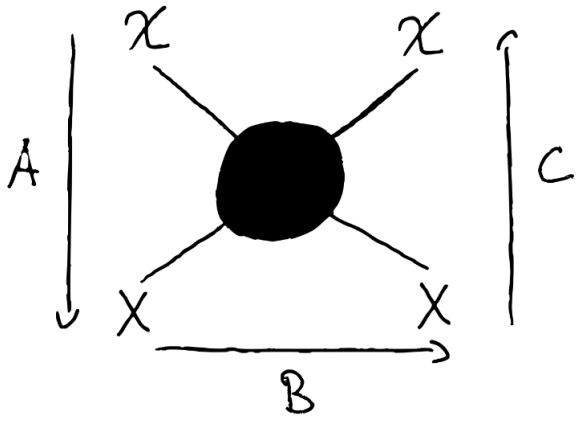

Figure 8: The three DM detection channels of a DM particle χ interacting with SM particles X. The arrows indicate the direction of time. A) Indirect detection through observation of DM decay products. B) Direct detection through observation of deposited energy in elastic scattering processes. C) Production in e.g. collider experiments. The signature would appear as missing energy.

Production in Particle Colliders

Reading the schematic with respect to the direction labeled C, the process shown corresponds to the annihilation of a SM particle pair into DM particles. Collider experiments carry a great premise to be the first to announce a discovery of BSM particles. They provide controlled environments to study the properties of known particles and probe the limits of the SM. Proposed WIMP candidates, cf. section 2.4.2, in most cases arise from extension to the SM, supersymmetric extensions, whose parameter spaces are being probed at the accessible level in terms of center of mass energy. Future accelerators will achieve a larger center of mass energies [42]

[3]The strong interaction, even though its Lagrangian incorporates a CP-violating term, is observed to conserve CP symmetry.

and open up the possibility to probe even deeper into the parameter spaces of these proposed particles. This approach is currently under investigation by various BSM searches at the Large Hadron Collider (LHC) [43]. Due to its weak interaction strength, DM is expected to not interact with any of the detector materials. Candidate events are therefore generally inferred by missing transverse momentum. In addition, the unknown nature of the interaction introduces many free parameters and renders most analyses strongly dependent on the underlying model. A comparison of the constraints obtained from DC production with the other detection channels is shown in figure 11a.

Indirect Detection

Following the direction labeled A, the diagram corresponds to the annihilation of a DM particle pair into SM particles. The idea of indirect DM searches consists of the assumption that DM annihilation can occur in over-dense regions in space, where DM is believed to accumulate. The decay into SM particles would then result in an anomalous flux of particles. Typical candidate sources are the Galactic center, the sun's core, or even the Earth. The instruments employed for this purpose are Cherenkov telescopes, neutrino detectors, or space-based particle detectors. The large variety comes from the fact that different signatures require different instrumentation. The cleanest detection channels contain neutrinos in the final state. In contrast to photons or other SM particles that interact electromagnetically, neutrinos generally point back straight to the source, and DM annihilation is expected to occur close to the core of the source under study. The sun provides an excellent probe for DM annihilation since only neutrinos are able to escape its dense ionized interior. The expected background is also comparatively small, considering that the solar neutrino flux is well understood and populating a significantly smaller energy scale than the neutrinos emanating from DM decays ($>$ 1 GeV) [44]. Figure 11b shows a comparison of the constraints computed from indirect detection experiments with the other DM detection channels.

Direct Detection Principles

Direct detection experiments search for signs of DM scattering interactions with target atoms, as depicted by label B, becoming noticeable through energy deposited to the latter. Due to their large mass, WIMPs are expected to interact coherently with a target nucleus. This means that at low enough momentum transfer, the WIMP interacts with the nucleus as a whole and causes it to recoil. The expected interaction rate is given by [29]

$$\frac{dR}{dE}(E,t) = \frac{\rho_0}{m_\chi m_A} \int v \cdot f(v) \frac{d\sigma}{dE}(E,v) d^3v \tag{10}$$

where ρ_0 is the local DM density, $f(v)$ its velocity distribution, σ the corresponding cross section and m_χ, m_A are the DM and nucleus masses respectively. Since the only tangible quantity of equation (10) is the nucleus mass, all other quantities rely on specific models of, for instance, the local DM density or velocity distribution, provided in section 2.4.1. The cross section is usually computed under the assumption of Dirac-like DM, i.e. a spin-$1/2$ particle with a scalar, vector, or axial-vector coupling, resulting in a spin-independent (SI) term (for the scalar and vector couplings) and a spin-dependent (SD) term (related to the axial-vector coupling) [45].

$$\frac{d\sigma}{dE}(E,v) = \frac{m_A}{2\mu^2 v^2} \Big(\sigma_0^{SI} F_{SI}^2(E) + \sigma_0^{SD} F_{SD}^2(E) \Big) \tag{11}$$

with the reduced mass of the WIMP-nucleus system μ and form factors F_{SI} and F_{SD} of the SI and SD processes respectively. The latter are included to account for the loss of coherence

at larger momentum transfer or for heavy target nuclei such as xenon, where in both cases the target atom does not participate in the interaction as a point-like particle anymore and its constituent nucleons have to be included. To facilitate comparison between different target nuclei employed by different experiments, the WIMP-nucleus cross section is usually given in terms of the WIMP-nucleon cross section σ_n. The SI cross section is then given by

$$\sigma_{SI} = \sigma_n \frac{\mu^2}{\mu_n^2} \left(\frac{f_p Z + (A - Z)}{f_n} \right)^2 = \sigma_n \frac{\mu^2}{\mu_n^2} A^2 \tag{12}$$

with the reduced mass of the WIMP-nucleon system μ_n and the WIMP couplings to the proton f_p and neutron f_n. The right-hand side of equation (12) assumes $f_p = f_n$. The SI process is then contingent on the target mass via $\sigma_{SI} \propto A^2$. The cross section scales with the mass number A squared, increasing the expected event rate of heavier target materials, but at the cost of lower expected recoil energy. The spin-dependent counterpart is insensitive to the target's mass. The relevant nucleus feature, in this case, is its spin structure and the SD cross section scales as $\sigma_{SD} \propto {}^{(J+1)}/_{J}$, with the total spin of the nucleus J. In this sense, target nuclei with total spin 0 do not participate in this kind of interaction.

2.6 Direct Detection Applications

In general, the energy deposited by WIMPs in the target material of a detector is described by

$$\left(\frac{dE}{dx} \right)_{tot} = \left(\frac{dE}{dx} \right)_{e} + \left(\frac{dE}{dx} \right)_{nr} \tag{13}$$

where the majority of the nuclear recoil (NR) energy transferred in the WIMP-nucleus interaction is typically lost to heat, i.e. to an increase of atomic motion in the target, denoted by the index nr, and a smaller amount to excitation or ionization via interactions with electrons of the atomic shell [45], denoted by the index e. Purely electronic recoils are a source of background events in WIMP searches, arising mostly from interactions with γ-radiation. The NR process can in principle generate three types of signatures, depicted in figure 9: the deposited energy is either absorbed as heat, or, in the case of scintillating materials, such as some liquid noble elements, light is produced. The atoms can also become excited or ionized, producing again scintillation light or free charges. The available detection channels are thus heat, in the form of phonons, light, and charge. Most experiments employ detectors able to read-out multiple channels at the same time since nuclear and electronic recoils populate the different signatures with differing proportions. The multi-channel read-out can then be exploited to provide efficient signal/background discrimination. Due to the wide range of possible DM masses, a multitude of experimental techniques are applied in direct detection DM searches.

Cryogenic detectors exploit the low heat capacity of some crystalline structures at temperatures of a few mK to measure energy depositions in the order of 1 keV. Typical target materials are high-purity germanium or silicone crystals. By additionally placing a voltage across the crystal, the free electrons produced through ionization can be extracted. This method is employed by e.g. the EDELWEISS [46] and SuperCDMS [47] experiments and is most sensitive towards WIMP masses $< 10\,\text{GeV}$. Instead of extracting charges, there are a number of experiments employing cryogenic detectors that have a parallel read-out of phonons and scintillation light. The CRESST-III experiment [48] employs a small-scale detector operating $CaWO^4$ scintillating crystals. While cryogenic detectors generally have outstanding energy resolution, one main drawback is that scaling up in terms of target mass is challenging. Given that the crystal's heat capacity is directly proportional to its mass, the size of the detector is confined to the

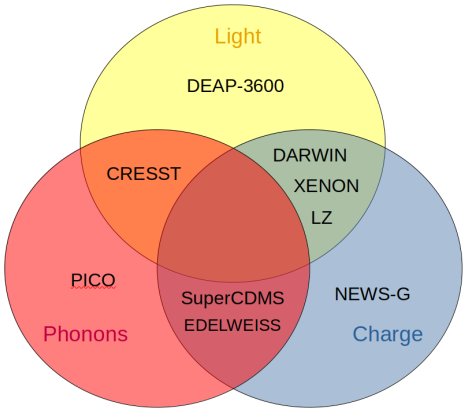

Figure 9: Schematic of the three possible signatures from $\chi X \to \chi X$ interactions. The overlapping regions indicate potential multi-channel detection methods. A selection of current, past, and future experiments and the channels they exploit is presented.

kg-scale [45]. A popular workaround is employing crystal arrays, but refrigeration to mK-temperatures is expensive and non-trivial.
Noble Liquid Detectors exploit the scintillating properties of noble gases. Some materials respond to incident radiation by emitting light of a characteristic spectrum. Light produced in this fashion is generally referred to as scintillation light. Some liquid noble gases, namely argon, and xenon, have the additional benefit of simultaneously producing free electrons via ionization as part of the underlying mechanism, which is understood as follows and depicted in figure 10: An incident particle deposits some of its energy in the medium producing heat, as well as excited X^* and ionized atoms X^+, where $X = Xe, Ar$. The excited atom also referred to as an exciton, can combine with a neighbouring neutral atom to form an excited dimer, or excimer, X_2^*. The excimer then decays under the emission of a photon.

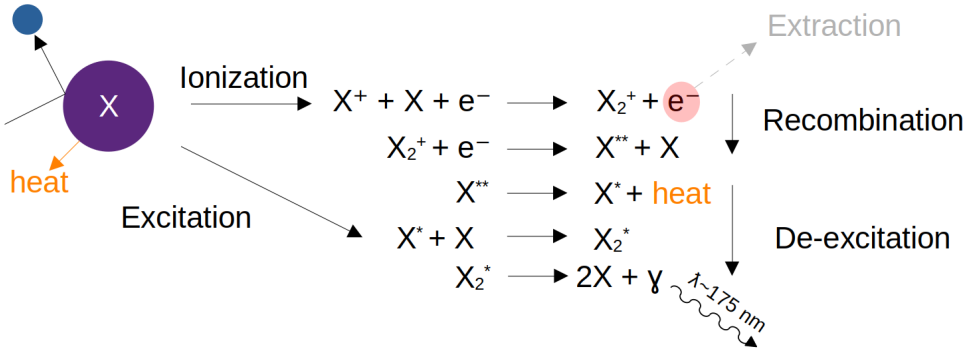

Figure 10: Schematic overview of the scintillation light production mechanism in liquid noble gases following a scattering event.

Note that there is an intermediate stage before de-excitation, effectively rendering the material transparent to its own scintillation light. If left to recombine, the ions are excited and will subsequently decay under the emission of scintillation photons. If instead the ionization electrons are extracted by an applied electric field, charge and light can be read out separately. The process labeled 'Ionization' in figure 10 is suppressed and an anti-correlation between light and charge yield emerges, depending on the strength of the drift field. The scintillating properties of liquid noble gases are exploited in two distinct ways. *Single-phase* detectors, as employed by

the DEAP-3600 collaboration [49], only measure scintillation light and generally have spherical geometry and photosensors all around in a 4π configuration. However, they rely on pulse shape discrimination (PSD) for electronic recoil background rejection. PSD exploits the fact that the excimers X_2^* and X^* in both processes are produced in different spin states, namely in a spin-singlet or -triplet state. Their decays are governed by different decay constants or half-lives. Since the difference in the decay constants of the individual spin-states of xenon excimers is comparatively small, PSD is rendered largely inefficient. The material of choice here is argon, where the half-lives differ by multiple orders of magnitude [45].
The most competitive constraints on the SI WIMP-nucleon cross section for WIMP-masses in the range $m_\chi \sim 1\,\text{GeV}$ to $10^3\,\text{GeV}$ currently stem from liquid xenon based experiments, cf. figures 11 and 12, employing *two-phase time projection chambers* (TPC). An in-depth discussion of TPCs follows in Chapter 3. They have been succesfully operated by the XENONnT [50] and LUX-Zeplin [51] collaborations, with target masses of 5.9 t and 7 t of xenon, respectively. The world leading constraints on the SI WIMP-nucleon cross section with a minimum upper limit of $9.2 \times 10^{-47}\,\text{cm}^2$ for a WIMP mass of 32 GeV [52] at 90% confidence level is currently reported by the LZ collaboration, cf. figure 12.

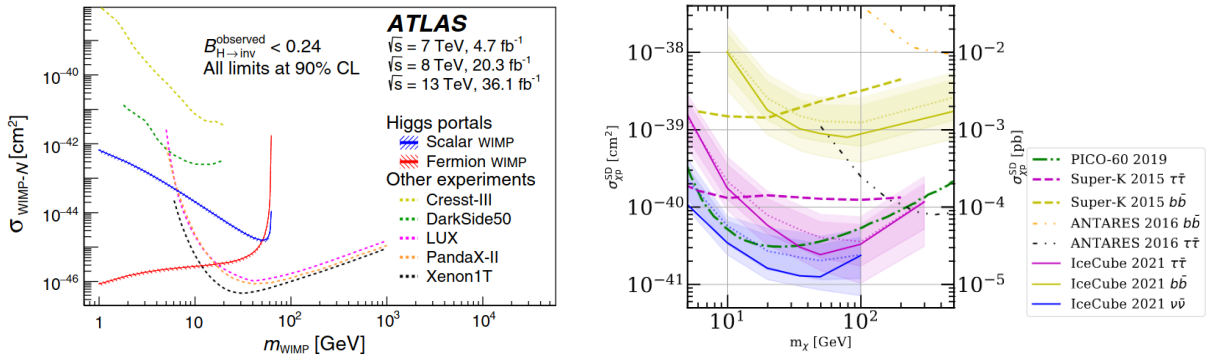

(a) (b)

Figure 11: a) Comparison of upper limits at 90% C.L. on the spin-independent WIMP-Nucleus interaction cross section, compared with direct detection results, assuming Higgs-portal scenarios where a Higgs boson decays to an invisible DM pair. Figure from [43]. b) Comparison of the lower limits on the SD WIMP-proton cross section as computed from neutrino telescopes (IceCube, Antares, Super-K) and the PICO-60 bubble chamber. Figure from [53].

Apart from the single-phase argon detectors, there are a number of experiments also employing technologies, where only a single channel is exploited. The NEWS-G [54] and PICO [55] collaborations employ a *proportional gas counter* and a *bubble chamber*, respectively. NEWS-G's proportional gas counter consists of a spherical detector filled with a neon-methane gas mixture. An applied bias voltage drifts the ionization electrons produced in scattering events toward the center of the sphere, where the charge is read out. The detection threshold reported is $\mathcal{O}(10)$keV. The low threshold and light target material neon make it especially sensitive to sub-GeV WIMPS. The PICO-60 bubble chamber holds 52 kg of C_3F_8 in a superheated state. Fluorine F, with a total spin of $J = 1/2$, provides maximum sensitivity to the SD interaction. The liquid is kept at a temperature close to the boiling point and pressures slightly below the vapor pressure, such that energy depositions lead to a localized phase transition. These become noticeable through the formation of bubbles, which are then captured by a set of cameras. The advantage of this approach lies in an excellent rejection of the electronic recoil background. The

system can be tuned in such a way that interactions of charged particles with the target do not impart enough energy to initiate nucleation without significant loss of sensitivity to nuclear recoils [56]. The current state of direct detection experiments is summarized in figure 12. A detailed description of LXe-based two-phase TPCs and the DARWIN experiment is presented in the following Chapter.

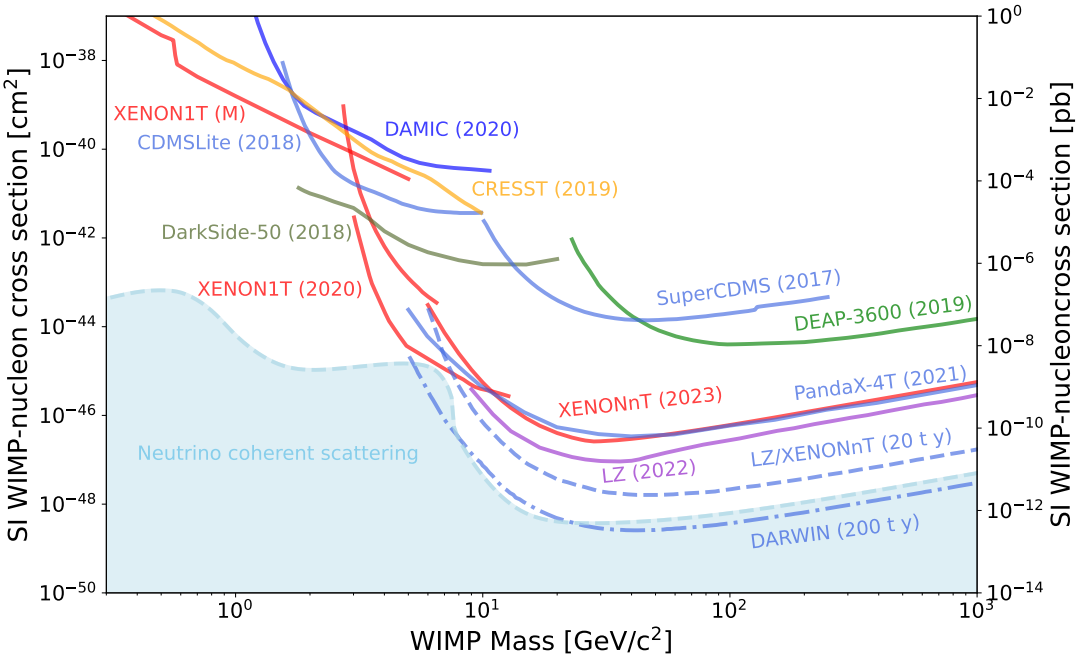

Figure 12: Upper limits of direct detection experiments on the SI WIMP-nucleon cross section. Indicated by the dotted-dashed blue lines are the projected limits of both LZ and XENONnT and DARWIN at an exposure of 20 t y and 200 t y respectively. Image credit: Laura Baudis

3 The DARWIN Observatory

3.1 Xenon as a Detector Medium

The scintillation wavelength of xenon is 175 nm [57], which is well within the sensitive range of most vacuum-ultraviolet (VUV) sensitive photosensors. The main reason for the prevalent use of xenon in direct detection experiments lies in its high mass (Z = 54) and superb radio purity. At cryogenic temperatures (T = 178.0 K, p = 2.0 bar) its density in the liquid phase is ρ =2853.9 kg m^{-3} [58]. This makes it an ideal target material, since its high mass number boosts the spin-independent cross section, cf. section 2.5, and its high density effectively stops penetrating radiation. This self-shielding capability can be exploited to design more compact detectors because the large stopping power of xenon creates a mostly background-free region in the inner part of the active detector volume. By requiring candidate events to coincide with this inner volume, the background rate can be reduced drastically. This procedure is usually referred to as fiducialization.
Of course, fiducialization can only work if the material itself is not a main source of background radiation. Xenon has nine naturally occurring isotopes. Six of which are stable, with the remaining three, ^{124}Xe, ^{134}Xe and ^{136}Xe having halve-lives of the order of 10^{21} y or greater. Furthermore two isotopes, ^{129}Xe and ^{131}Xe, with total spins 1/2 and 3/2, occur with large natural abundances of 26.4% and 21.2%, respectively, providing sensitivity to the spin-dependent term in equation (11) [59]. Combined with the relatively high boiling temperature of T $\simeq$ 178 K at p = 2 bar, xenon proves to be a highly sensitive, manageable, and scalable medium for direct detection purposes.

3.2 Two-Phase Time Projection Chambers

A *Two-phase time projection chamber* (TPC) measures both scintillation and charge. The target material usually consists of liquefied xenon (LXe), monitored by two arrays of photosensors, one placed at the bottom and the other at the top of the setup. While the bottom array is submerged in the liquid, the top array is immersed in gaseous xenon (GXe), placed a short distance above the LXe/GXe interface. A schematic overview is presented in figure 13. An electric field is maintained by a cathode operating on negative potential, placed above the bottom array, and a grounded gate located below the interface. A stronger extraction field is placed between the anode, which is kept at positive voltage, above the liquid phase and the gate. Field uniformity inside the detector volume is improved by a set of field-shaping copper rings, adequately biased, enveloping the active target.
A particle interacting with the target produces a prompt flash of scintillation light, as well as ionizing a portion of the atoms. The freed electrons are drifted towards the gate by the applied drift field E_{drift}, where they are extracted from the liquid phase by the extraction field $E_{extraction}$ between the gate and anode. In the gas phase, the accelerated electrons are energetic enough to produce light via proportional scintillation. The corresponding signals, as measured by the photosensors, are referred to as S1 (prompt scintillation) and S2 (proportional scintillation). The coordinates of the interaction site can be reconstructed via the specific signature, often referred to as the hit pattern, created by an event in the top array, giving the position in the x-y-plane, and the time difference between the S1 and S2 signals, providing the vertical position based on the proportionality between the electron drift time and the depth of the interaction.
The energy transferred in a scattering event is a function of the amount of quanta, i.e. photons and electrons, produced in the interactions, and is therefore directly related to the S1 and S2 signals. However, losses affect both the prompt and proportional scintillation in distinct ways.

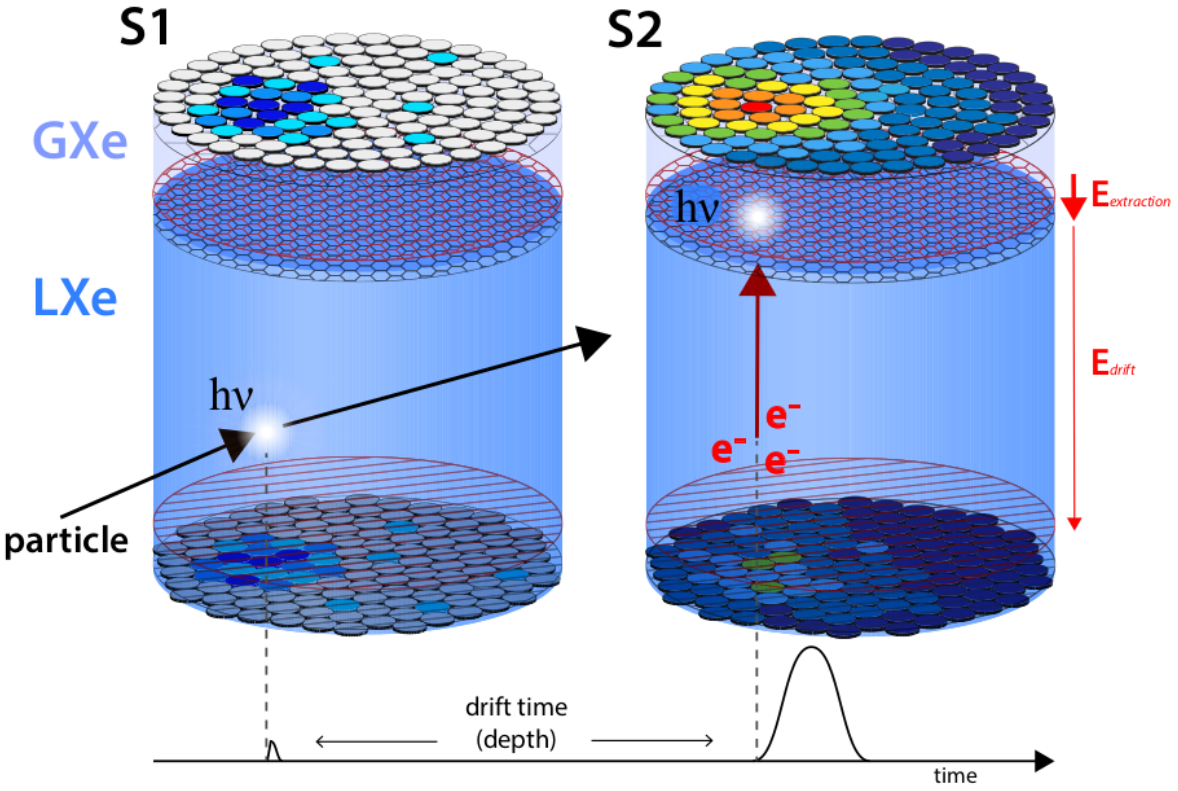

Figure 13: Schematic illustrating the basic working principle of a two-phase TPC. A particle colliding with the detection material imparts some of its energy leading to a prompt scintillation response. Free charges produced in the interaction are drifted upwards by an applied drift field between the cathode (at the bottom of the setup) and the gate (slightly below the LXe/GXe interface. An extraction field between the gate and the anode (at the top of the setup) extracts the charges from the liquid phase to the gas phase, where a second burst of scintillation light is produced via electroluminescence. The light is registered by two arrays at the top and the bottom of the setup. Figure from [59].

S1s suffer deterioration from position-dependent effects, such as internal reflection at the liquid-gas interface for events occurring close to the surface. The ratio of the quanta that are registered versus the total number of quanta produced is called the light collection efficiency (LCE). The S2 experiences defects from losses of charge during the electron drift from the interaction site to the LXe/GXe interface. The free charges can attach to impurities remaining in the LXe. The probability of an electron reaching the gas phase is characterized by the mean time before the charge recombines, referred to as the *electron lifetime* τ_e, and the depth-dependent drift time $t_{drift}(z)$. The LCE of the S2 signal is also contingent on any inhomogeneities, such as warping or sagging, of the electrode, which is corrected by the inclusion of the $\mathrm{LCE}_{S2}(x,y)$ term. The corrected signal yields are thus given by:

$$cS1 = \frac{S1}{\mathrm{LCE}(x,y,z)} \qquad cS2 = \frac{S2 \cdot \mathrm{LCE}_{S2}(x,y)}{exp(-t_{drift}(z)/\tau_e)} \tag{14}$$

The number of signal photons n_γ and electrons n_e can be extracted by incorporating the primary and secondary scintillation gains $g1 = {}^{cS1}/_{n_\gamma}$ and $g2 = {}^{cS2}/_{n_e}$. From the S1 and S2 signals the

energy is then reconstructed as:

$$E = \left(\frac{cS1}{g1} + \frac{cS2}{g2} \right) \cdot W \tag{15}$$

Where the mean excitation energy $W = (13.7 \pm 0.2)\,\mathrm{eV}$ [60] corresponds to the average energy needed to produce either an electron or a photon in liquid xenon [59]. A competing value of $W \simeq 11.5\,\mathrm{eV}$ [61], measured in $\mathcal{O}$(1-10keV) electronic recoils, was recently reported. Further independent measurements are required to settle this tension.
The anti-correlation between the scintillation (S1) and charge (S2) yield is exploited to reject the background emerging from electronic recoil. While nuclear recoils have a high recombination fraction, meaning a strong S1, the fraction of charges that are extracted to the gaseous phase is greater in electronic recoils, resulting in a prominent S2 signal. The ratio $^{S2}/_{S1}$ is thus smaller for nuclear, as compared to electronic recoils. This allows for efficient discrimination between the two [59], such that all advantageous properties listed in the previous section (3.1) can be fully exploited without loss of sensitivity.
Though fiducialization, cf. section 3.1, allows for effective rejection of events originating from ambient radiation, additional care is required to mitigate cosmogenic backgrounds. The vast majority of direct detection experiments are therefore located deep underground to use the rock overburden as passive shielding against cosmogenic radiation. Examples include XENONnT at the Laboratori Nazionali del Gran Sasso (LNGS), located in a highway tunnel beneath the Gran Sasso mountain with a rock overburden of 1400 m (3600 m water equivalent (w.e.)) and LZ at the Sanford Underground Research Facility (SURF) [62], located 1500 m (4300 m w.e.) underground.

3.3 A Next Generation Dark Matter Observatory

The available technologies dedicated to the detection of DM are constantly being pushed to reach ever-higher sensitivities. One popular avenue is to enhance exposure, i.e. mass×time, by scaling up the active target. The DARk matter WIMP Search with Liquid XenoN (DARWIN) project is a proposed experiment that will host a two-phase TPC at its core. The baseline design will entail a target mass of up to 50 t of xenon, 40 t of which will be actively instrumented, in a cylindrical TPC 2.6 m in diameter and height. The resulting projected exposure of $200\,\mathrm{t} \times \mathrm{y}$ will be able to probe SI WIMP-nucleon cross sections down to a few $10^{-49}\,\mathrm{cm}^2$ for WIMP masses of ∼50 GeV [63], as depicted in figure 12, and reach the *neutrino fog*, indicated by the light blue shaded region. Below this threshold, direct detection experiments become sensitive to elastic scattering processes of neutrinos with the target material, referred to as *coherent elastic neutrino-nucleus scattering* (CEνNS), which will constitute an irreducible background to DM searches. The DARWIN collaboration aims to exploit this surge in sensitivity to enhance our understanding of the energy production mechanism of the sun, by a precise measurement of the solar neutrino flux in the electronic recoil $\nu + e^- \rightarrow \nu + e^-$ channel. The precision after five years of data taking is projected to be below 1% [63].
The electric field for electron drifting and extraction will be provided by a set of three circular dynodes, 2.6 m in diameter each. The field strength required to efficiently drift ionization electrons towards the LXe/GXe interface is of $\mathcal{O}(0.5)\mathrm{kV\,cm}^{-1}$. The necessary bias voltage applied to the cathode will thus be around −100 kV. The active volume at the core of the TPC will be enveloped by, firstly, a lining of polytetrafluoroethylene (PTFE) to act as a reflector for the xenon scintillation light, and secondly, a set of roughly 100 oxygen-free high-conductivity copper field shaping rings to ensure drift field homogeneity. The former is additionally suited as an insulator to protect sensitive components from the high voltage ubiquitous inside the detector.

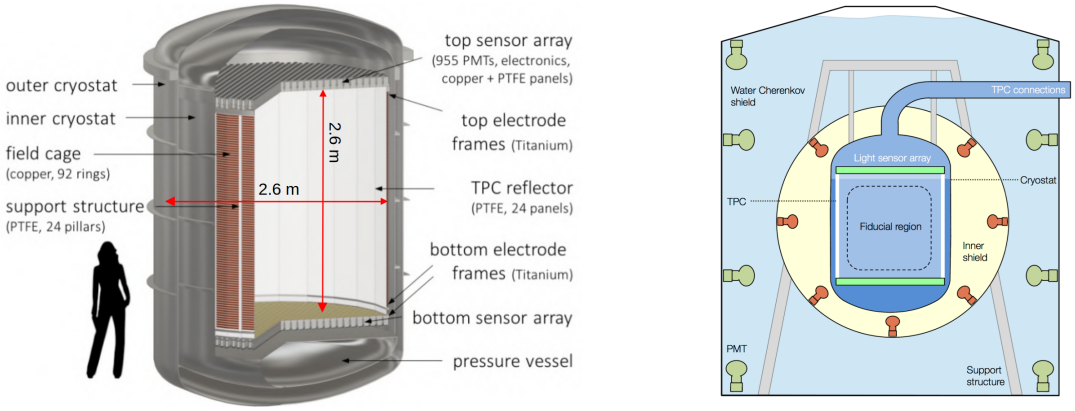

(a) (b)

Figure 14: a) Schematic of the baseline design of the DARWIN two-phase TPC and cryostat. b) Schematic of the active shielding in the DARWIN baseline design. The first stage consists of a water Cherenkov muon veto. The inner shield will contain a liquid scintillator to preemptively identify neutrons entering the detector. Figures from [63].

The materials used in manufacturing all components of the TPC are held to the highest standard of radio-purity, in order to minimize the amount of radiogenic background introduced to the system. This also includes the double-walled cryostat designed to hold the TPC and maintain the target at stable temperature and pressure. The cryostat will be suspended from a support frame, designed to allow for precise leveling of the TPC up to 0.1 mm precision.
The main background in WIMP searches is attributed to neutron-induced nuclear recoils. Apart from ambient radiation, a significant source of neutrons arises from cosmic muons producing secondary neutrons in hadronic or electromagnetic showers. To mitigate their effect DARWIN will be located at an underground facility with the primary option being LNGS. However, high-energy muons are still able to penetrate the 1.4 km rock overburden. A two-layer active shield has been proposed to further reduce this cosmogenic background, depicted in figure 14b. They consist of an outer shield in the form of a water Cherenkov muon veto and an inner liquid scintillator neutron veto. The former exploits the phenomenon of Cherenkov radiation, where charged particles traversing a medium with a velocity greater than the speed of light in said medium emit electromagnetic radiation. A water tank surrounding the detector is monitored by PMTs for the Cherenkov light, to check for coincidences between the water tank and the active LXe target.
A TPC of this size comes with a host of new challenges that are currently being addressed by extensive R&D campaigns. This extends to the question of which type of photosensor is to be employed. Key requirements are low intrinsic radioactivity and high sensitivity towards xenon scintillation light. The chosen photosensor should also be able to operate in the presence of strong electric fields. The baseline design would require ∼1800 units of R11410 3” photomultiplier tubes (PMTs), employed in XENONnT and LZ, to cover the active target. The main advantages of PMTs include low radioactivity, high sensitivity to the wavelength of xenon scintillation light, and very low dark count rate, cf. section 4.2. The main drawbacks are that compared to technologies like silicon photomultipliers (SiPMs), PMTs are generally more bulky and require a more sturdy support structure to keep them affixed. Especially in the high-pressure region at the bottom of the setup, where effects from buoyancy become increasingly noticeable. A compact form factor is therefore favourable, since it allows to decrease the amount of material in the support structure and with it the radioactivity introduced to the system.
Position reconstruction also benefits from more compact sensors, provided the sensitive area

coverage in an array remains the same. Adding more read-out channels to the same covered area increases the granularity and with it the precision of event localization in the x-y-plane. One PMT considered for the next generation direct detection experiment is the Hamamatsu R12699-406-M4 square-shaped 2" PMT, which provides the two aforementioned advantages. In its baseline design, the DARWIN TPC would require approximately 3000 units. A first step in evaluating its suitability for application in LXe TPCs is presented in this work. An in-depth discussion of the working principle, the quantities of interest of PMTs, and the 2" PMT follows in section 4.1.

4 Photomultiplier Tubes and Their Performance

4.1 Working Principle of Photomultiplier Tubes

A photomultiplier tube is a type of photosensor that is able to measure single photon incidences. The mechanism of detection is based on the photoelectric effect and involves three main mechanical components as shown in figure 15. Firstly, the incident light imparts some of its momentum to an electron bound to the photocathode. If the energy transfer is larger than the work function of the material, a so-called photoelectron is dislodged from the cathode and drifted towards a set of dynodes, referred to as the multiplication stage, by an applied bias voltage. Secondly, upon contact with the dynodes, it displaces a number of secondary electrons, each of which repeats this process further down the multiplication chain. The potential differences between individual dynodes are provided by a voltage divider chain that distributes the bias voltage over the entirety of the multiplication chain. This results in an exponential increase of the initial photoelectron until finally, $\mathcal{O}(10^6 - 10^7)$ electrons (depending on the bias voltage, number of dynode stages, and PMT type) arrive at the anode, where a measurable current is registered. While the majority of PMTs, including the R11410 3"-PMT employed in XENONnT and LZ, have a single anode and dynode per stage, position-sensitive PMTs have a different dynode structure. Some models, such as the one under study in this work, employ metal channel dynodes, and multiple anodes that can be read out separately. This provides additional information on which part of the photocathode was activated.

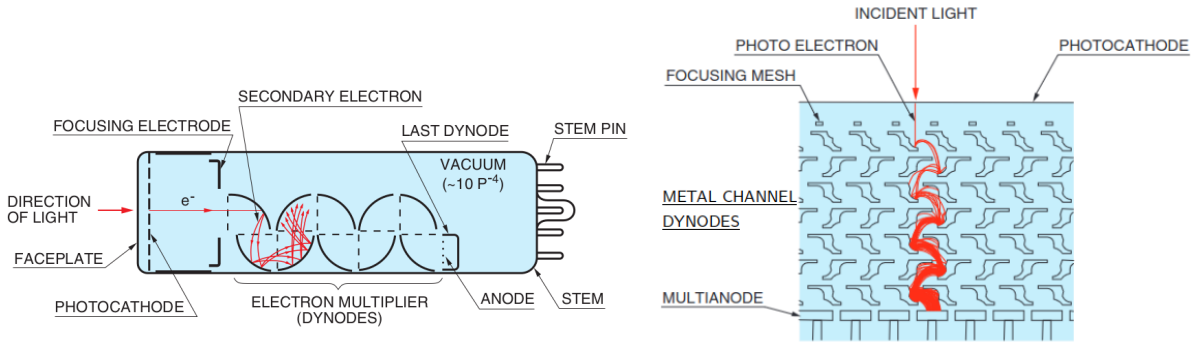

(a) (b)

Figure 15: (a) Schematic of the working principle in a common linear-focused PMT. Incident light ejects a photoelectron from the photocathode. The photoelectron is accelerated towards the first dynode where it is multiplied through secondary electron emission, which is repeated at each dynode. A measurable current arrives at the anode, where it can be read out. (b) Schematic of a multianode PMT with a metal channel dynode structure. The underlying principle remains the same, but the additional anodes provide information about which part of the photocathode was struck. This increases position sensitivity. Figures from [64].

4.2 Photomultiplier Tube Properties

The charge arriving at the anode is recorded as a dip in voltage. Figure 16 shows a typical PMT signal, usually referred to as a waveform, as recorded by the data acquisition (DAQ) chain or an oscilloscope. The baseline reflects the applied bias voltage. It has to be calculated for each

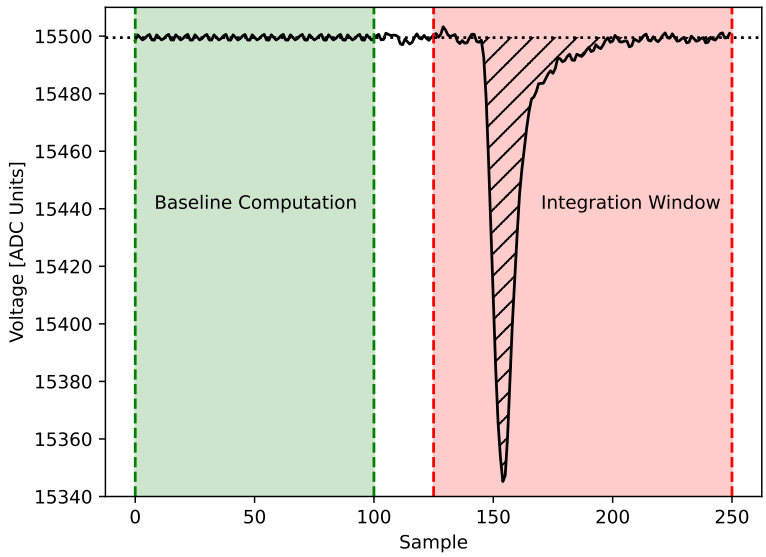

Figure 16: Example waveform with shaded areas indicating the computations performed over them. The green shaded area is used for baseline computation. The baseline corresponds to the median value assumed within the boundaries. The red-shaded area is where the triggered signal is expected to take place. The relevant quantity is the shaded area used for charge computation.

event individually since it is subject to random fluctuations due to noise arising from electronics in the read-out chain and the PMT itself. In general, the quantity of interest is the amount of charge arriving at the anode. It is proportional to the area A, indicated by the hatched region in figure 16, via Ohm's law. The area is determined by summing the entries inside the integration window and subtracting the baseline, which is the median value inside the baseline computation window. Accounting for the Analogue-to-Digital Converter (ADC) unit specif properties, the number of charge carriers is computed as

$$N_e = A \cdot \frac{r}{eaFZ} \tag{16}$$

where a simple conversion factor containing the ADC unit's resolution[4] r, its sampling frequency F, the output impedance Z, the electron charge e, and the amplification applied to the signal a, is factored to the calculated area. The values specific to the ADC unit used during data acquisition are $r = {}^{2.0}/_{2^{14}}\,\mathrm{V\,bit^{-1}}$ and $F = 500\,\mathrm{MHz}$, corresponding to a sample taken each 2 ns. The output impedance amounts to $Z = 50\,\Omega$ and a tenfold signal amplification, $a = 10$, is applied. The resulting number of charge carriers can vary from -100 to 10^7, where negative values extracted generally stem from *empty* waveforms, i.e. waveforms where no light was registered. The recorded areas are then determined by the baseline fluctuation, which can assume negative values.

The PMT response is best summarized by its charge spectrum, i.e. the histogram of the number of charge carriers extracted over a fixed period of time. An example of a charge spectrum compiled in a calibration measurement is shown in figure 17. The first peak centered close to 0 is due to waveforms that do not contain a photon response. Its width gives insight into the extent of the baseline fluctuations. The second peak centered at μ corresponds to the average amount of charge produced by a single initial photoelectron. The individual multiplication

[4] computed as the unit's dynamic range in volts divided by the number of ADC channels.

processes at each dynode are discrete in nature and well described by a Poissonian distribution. However, because this process is repeated at n individual multiplication steps, n being the number of dynode-stages, for sufficiently large n, the central limit theorem states that the overall distribution is Gaussian in good approximation. The charge distribution related to a single photoelectron is referred to as the single photoelectron (SPE) distribution. Its mean gives the average number of charge carriers produced per photoelectron (in a certain regime) and is commonly called *gain* in literature. Accordingly, the ratio of the width and the mean σ/μ is a measure of the PMT's ability to resolve the SPE response, which is usually referred to as the *SPE resolution*.
The underlying concept of energy reconstruction in any TPC is that the light yield is proportional to the deposited energy. In order to reconstruct the energy, the yield has to be extrapolated from the amount of charge produced in the PMTs. The assumption that directly relates the extracted charge to the number of incident photons, is the one of *gain-linearity*. It states that, in a given illumination regime, i.e. not exceeding a number of incident photons, the mean response of PMTs in terms of charge is linearly proportional to the number of initial photoelectrons. This is reflected in the charge spectrum in figure 17 by its equidistant peaks. In other words, given an event that produces k photoelectrons, the expected charge is k-times the gain. The entire charge spectrum is thus characterized by the first two moments of the SPE distribution.
A good description of the charge spectrum, however, also presupposes a thorough understanding of the backgrounds inherent to the PMT. Apart from static noise, inducing the baseline fluctuations, the dark current is the main driver of uncertainty on the SPE distribution. Its telling name comes from the fact that it refers to charges that are not directly produced by incident photons. This has two main causes [64]:

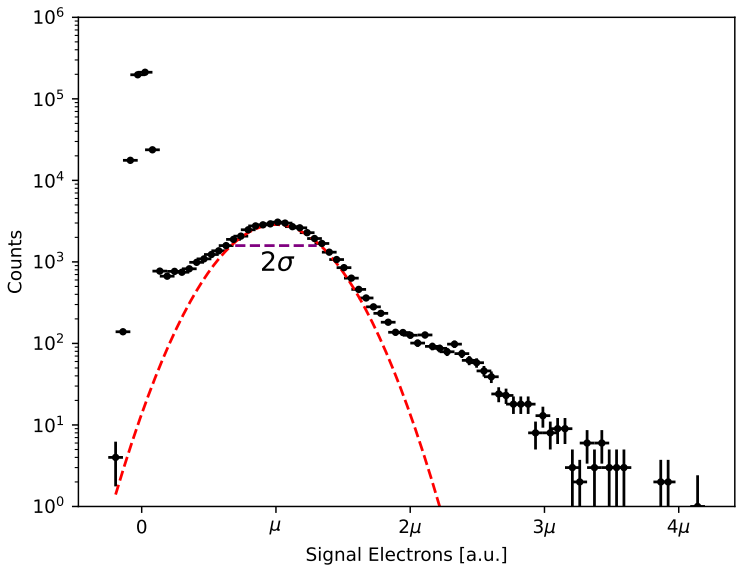

Figure 17: Exemplary charge spectrum of a 2" PMT with the Gaussian SPE distribution illustrated by the red dashed line. The width of the distribution is indicated by the purple dashed line. The means of the 2-, 3- and 4-PE are given by the ticks on the x-axis, marking the linear nature of the PMT gain.

i) **Thermionic emission**: To ensure high sensitivity, the photocathode and dynodes are usually composed of materials with low work function. The disadvantage is that they can

emit electrons spontaneously just due to their thermal energy. These thermally induced electrons cause signatures in the PMT that are indistinguishable from photonic events.

ii) **Afterpulsing**: The interior of PMTs is kept at vacuums as high as 10^{-6} MPa. However, the few residual gases can still affect measurement. An electron striking a molecule can easily ionize it. The positive ion is then accelerated towards a dynode or the photocathode, where it will dislodge a number of electrons, starting an avalanche of secondary charge carriers that results in a subsequent peak in a single waveform, referred to as an afterpulse (AP). A much faster afterpulse arises from electrons scattering elastically from the first dynode. In general, they are not separable from the main pulse, because they occur at orders of magnitudes faster than the signal processing can resolve.

Other contributions arise from ambient radiation or cosmic rays producing scintillation light in the PMT window. These two, however, can be controlled by adjusting the experimental conditions, such as placing the PMTs deep underground with additional active shielding, or by the choice of radio-pure materials within the vicinity of the experiment. The last contribution stems from radioactive isotopes contained in the PMT structure. This can only be mitigated by careful selection of materials.

4.3 The Multianode R12699-406-M4 Photomultiplier Tube

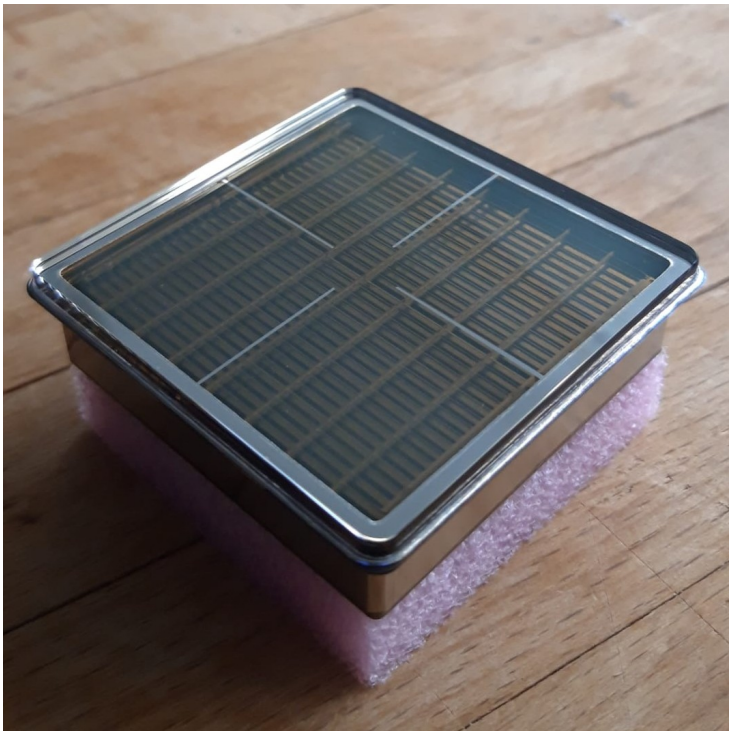

Figure 18: Photograph of the R12699-406-M4 2” PMT

The R12699-406-M4 [65] flat panel type multianode photomultiplier tube is a square-shaped photosensor produced by Hamamatsu Photonics K. K. with a side length of 56 mm and a height of 14.6 mm, without pins. It is designed for operation in cryogenic conditions at temperatures down to −110 °C. The bialkali photocathode has a quantum efficiency (QE), which is a measure of the probability of a photon of a given wavelength to induce a photoelectron, of 33% at a wavelength of 175 nm, with an effective area of $(48.5 \times 48.5)\,\mathrm{mm}^2$. The resulting packing

fraction A_{eff}/A_{tot} is 75%. This value roughly translates to the ratio of active versus dead sensor area in an array at the densest packing, due to the square shape of the instrument. The electron multiplier consists of metal channel dynodes with ten stages and four separate anodes. This divides the photocathode into four individual pixels that can be read out separately for finer granularity in position reconstruction. The typical gain reported by Hamamatsu is 1.5×10^6 with a typical time response of 1.2 ns rise-time[5] and 5.9 ns transit time[6] with a spread (FWHM) of 0.41 ns [65].
The most promising aspect of this particular photosensor is its compact form factor, c.f. section 3.3, and the low intrinsic radioactivity advertised by the manufacturer. The latter was verified by material screenings during different development stages of the sensors, performed with the low-background germanium counting facility Gator [66] at LNGS. The main objective of this work is to evaluate the feasibility of this instrument in direct detection applications. To this end, the PMT performance needs to be assessed in conditions as close to the real experimental environment as possible. This includes the cryogenic temperatures of around 178 K and to an extent the pressure close to 2 bar [7] all while being submerged in the detector medium.

[5]The average time for the anode output current to rise from 10% to 90% of its amplitude.

[6]The average time from the photon incident at the photocathode and the instant when the anode output current reaches its maximum value.

[7]Tests at higher pressures, which are expected to occur at the bottom of the DARWIN baseline design are pending

5 The MarmotX Facility

MarmotX is a test facility at the University of Zurich, with the specific purpose of testing photosensors in cryogenic xenon. An overview of its subsystems is given in figure 19. Its main component is a double-walled cryostat with an adjacent gas system, described in sections 5.1 and 5.2, for xenon filling and recirculation. A VME and NIM crate handle the power supply and signal readout, presented in section 5.3, of the instruments. The current configuration of the setup, as described in section 5.4, is designed to host up to four of the Hamamatsu R12699-406-M4 photomultiplier tubes, referred to as 2" PMTs from here on after. In the past, the facility hosted as many as ten R1140-21 3" PMTs [67]. The characterization of the eight units described in this work occurred in three independent data acquisition campaigns, described in chapter 6 and referred to as Run 0, Run 1, and Run 2.

5.1 The Cryostat

The MarmotX cryostat is a vacuum-insulated double-walled cryostat specifically designed for holding liquid xenon. Cooling is provided by a pulse tube refrigerator (PTR), powered by a helium compressor, with an additional liquid nitrogen-based emergency cooling system . The inner vessel can hold a volume of roughly 19 L of xenon. A single vacuum pump is used to either evacuate the inner or the outer vessel. After reaching a satisfactory vacuum in the inner vessel ($\mathcal{O}(10^{-5}\,\text{mbar})$), the chamber is sealed and the outer vessel can be mounted. The insulation vacuum is then maintained by continuous pumping of the outer vessel. The inner vessel is sealed by a CF flange (ISO 3669), whereas for the outer vessel KF flanges (ISO 2861) are in use. Further insulation from radiative heat transfer is provided by a multi-layer insulation sleeve, fitted around the entire surface of the inner vessel. Once the pressure in the outer vessel drops bellow $\mathcal{O}(10^{-4}\,\text{bar})$ filling can commence.
Once the xenon is filled, the cold-head continuously provides cooling power. A Cryocon 32b cryogenic temperature controller powers a heater, placed closely above the cold-head, to offset the constant influx of cooling-power and maintain the system stable and avoid freezing of the xenon to the cold-head. Frozen xenon enveloping the cold-head would act as an insulator, effectively reducing the cooling power and putting the system at risk of over-pressurization.
The target temperature in most TPCs is 178 K corresponding to a vapor pressure of about 2 bar. In practice however, the temperature and pressure were kept at 174 K and 1.8 bar, in order to have some leeway for unexpected fluctuations. In the current setup the Cryocon module can be regulated by two PT-100s thermistors, cf. section 5.3 and figure **??**, located next to the cold-head and mounted to the PMT support structures, cf. section 5.4, referred to as the bulk. The Cryocon was set to control the bulk temperature, in order to avoid it from overcompensating, given that the response to any change in the temperature of the gas phase arrives at large latency to the LXe. The presence of a temperature gradient between the gas and liquid phase further complicates achieving the target temperature, when controlling over the cold-head temperature. To avoid over-pressurizing the vessel, the system parameters are permanently monitored, see section 5.3, and the emergency cooling is configured to initiate via an automated valve if the pressure exceeds 2.3 bar. The automated valve connects a liquid nitrogen dewar to a small chamber located above the inner vessel. In case of above-threshold pressures, the chamber is flushed with liquid nitrogen, to quickly cool down the system. As an added redundancy, an emergency release valve is attached to the inner vessel to vent the xenon charge to air in case of pressures beyond 3 bar. Both systems have never needed to take action, owing to the fact that during normal operation the system demonstrated superb stability (temperature and pressure fluctuations were of the order of mK and mbar respectively) and system failures were always

detected in due time.

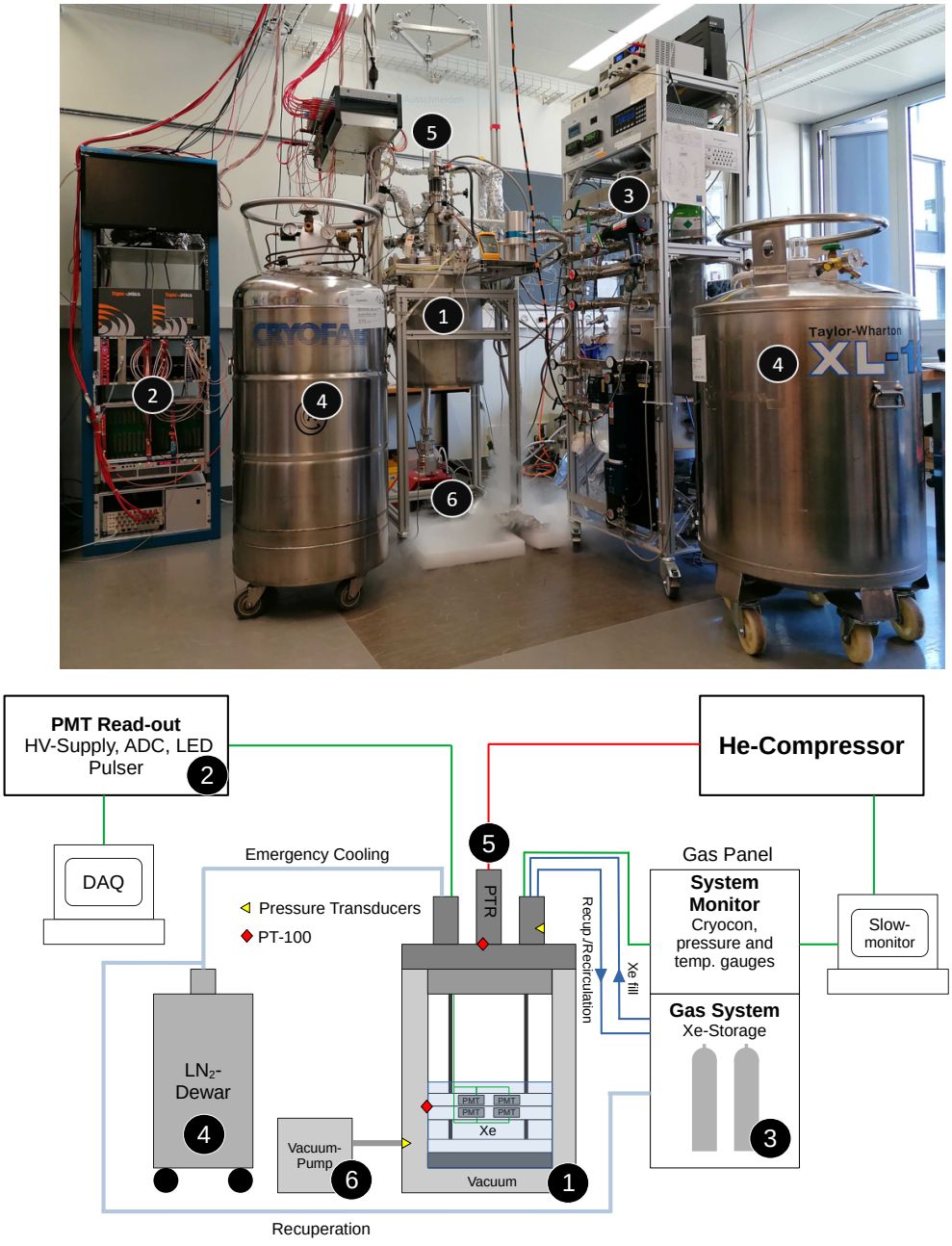

Figure 19: Overview of the MarmotX setup during the filling procedure. (1) Double-walled cryostat containing the instruments. (2) Rack holding the VME and NIM crates, housing the read-out chain and power supply. (3) Gas system and system instrumentation panel. (4) Liquid nitrogen dewars for emergency cooling and recuperation. (5) Pulse tube refrigerator providing the necessary cooling power to liquefy xenon. (6) Vacuum pump for evacuating the inner vessel and maintaining the insulation vacuum. Top image provided by Alexander Bismark.

5.2 The Gas System

Outside of operation, the 14.8 kg of xenon are kept in two separate storage cylinders for filling and recuperation, mounted to a Bosch profile containing all system parameter instrumentation and the gas system. Figure 20 shows a schematic of the MarmotX gas system. In an exemplary fill, where the bulk of the xenon is stored in cylinder 1, the flow is directed along the path indicated in red. During this procedure, cylinder two is constantly refrigerated using the liquid nitrogen dewar on the right-hand side of figure 19 as a safeguard. If the need arises to recuperate, keeping cylinder 2 at cryogenic temperature allows for quick recovery of the xenon via cryopumping[8]. The flow is controlled by a regulator. After filling is complete and valve 21 is closed, the xenon remaining in the line is evacuated by opening a path to the refrigerated cylinder 2. Although it was not employed during any of the three campaigns described in this work, the system is setup to allow for recirculation and purification of xenon by directing the path though the recirculation pump and the getter, both of which were bypassed during Run 0 through Run 2.
For evacuation of the inner chamber, cylinder two is again cooled with liquid nitrogen, and the path marked in green is opened. To increase the speed at which the xenon is extracted, a second line via valves 21, 19 and 8 were opened at times. This however leads to a steeper drop in pressure and in turn temperature and an additional heat input is needed to avoid damaging the PMTs. For Run 1 and Run 2, this was accomplished by breaking the insulation vacuum and heating the chamber wall with a heat-gun.

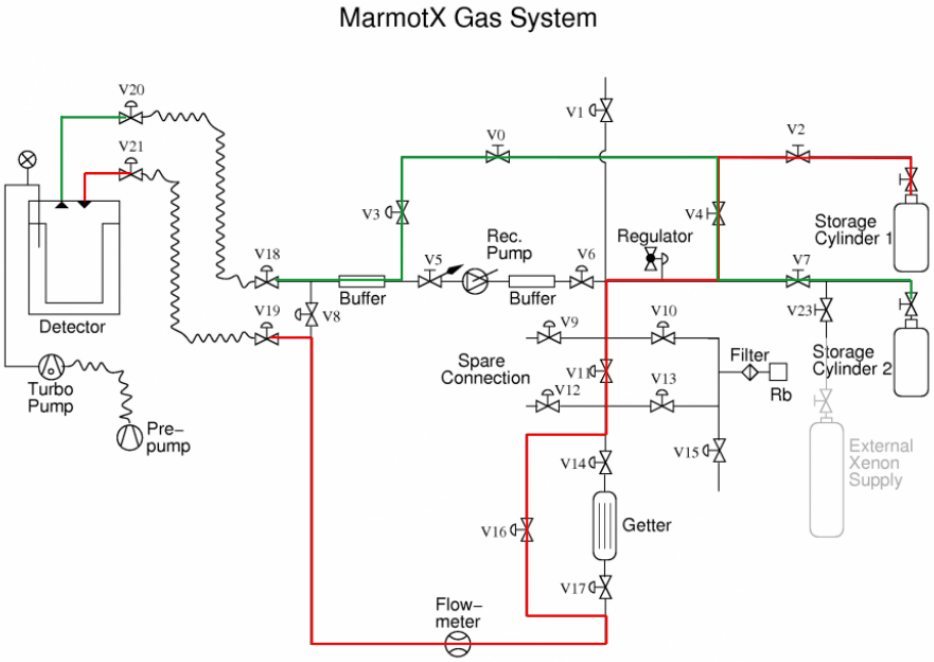

Figure 20: Schematic of the gas system. The red path follows the filling line. Green indicates the path for recuperation. Image credit: Andreas James.

[8] A technique where the content of the storage cylinder is kept at very low temperature, resulting in a negative pressure differential with respect to the rest of the gas system.

5.3 Slowmonitoring and Data Acquisition

5.3.1 Slowmonitoring

The system parameters are monitored constantly by a set of sensors inside the cryostat. Three separate pressure gauges monitor the insulation vacuum and inner vessel pressure. Two of the sensors are placed in the inner chamber to control conditions in vastly differing pressure ranges. An Edwards wide range gauge (10^{-9} bar to atmosphere) is installed in order to determine if the vacuum is sufficient to not contaminate the xenon supply prior to filling. Once the xenon charge is introduced to the system, it is maintained at pressures of up to 2 bar. This is then monitored by an Omega PX302-100AV pressure transducer with an operational range of 10^{-2} bar to 6.9 bar. The insulation vacuum is instrumented by a Pfeiffer TPR 280 gauge sensitive to pressures from atmosphere down to 5×10^{-7} bar. A series of PT-100 thermistors is placed in the inner vessel to monitor the temperature. As mentioned in section 5.1, the Cryocon regulates the system based on the temperature recorded at the bulk. It regulates the heat output based on three parameters: proportional to the difference of the actual temperature to the target (P), from the integrated evolution of the temperature (I) and the current rate of change, or differential (D), of the temperature. The so called PID values were determined by the autotune function integrated in the controller. The target temperature was set to 181 K, as depicted in figure 21. In the following description, the temperature in xenon is reported as 174 K. The discrepancy arises from a cross check performed in preparation of Run 1. In submerging the PT-100 in liquid nitrogen, an offset of around 7 K to 8 K between the boiling temperature of nitrogen and the reported value was observed. The temperature reported in the following is therefore the isochoric LXe temperature at a pressure of 1.8 bar. Finally, the gas flow from the storage cylinder into the cryostat chamber, or from recirculation is monitored by a Teledyne HFM-D-300 flow controller.

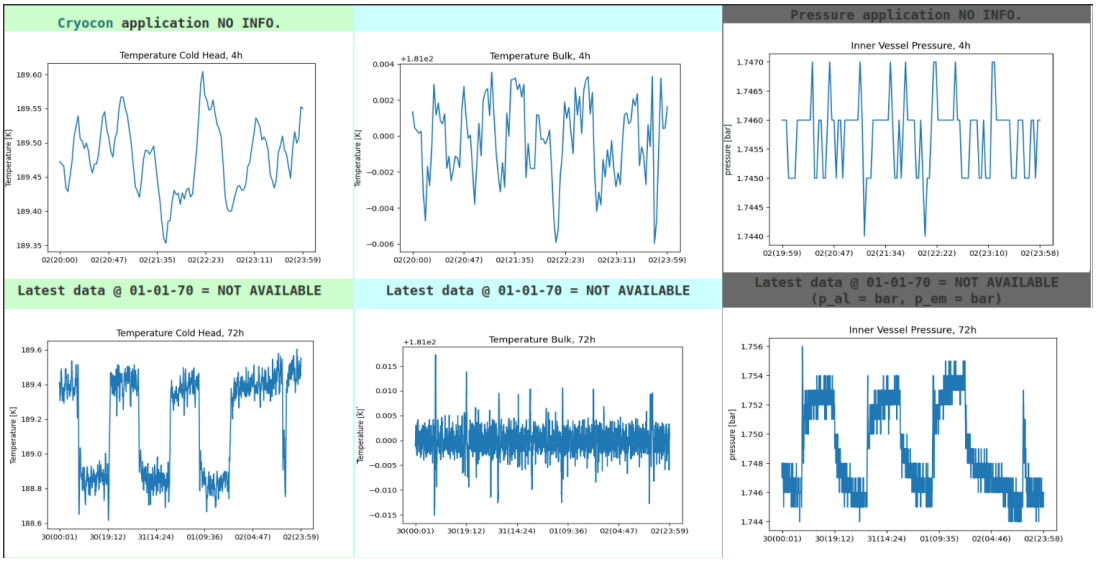

Figure 21: Screen-capture of the MarmotX slowmonitoring web page during stable operation in LXe. From left to right the following system parameters are displayed: Temperature at the cold head, temperature in the bulk and pressure in the inner vessel.

All of the instruments mentioned above, except the wide range gauge, which is decoupled from the system once the outer vessel is mounted, are connected to a slowmonitoring computer via RS232 serial connections. The slowmonitoring consists of a series of C-applications that indi-

vidually store data from the five gauges and display it on a web page for remote access. It has an integrated alarming system, sending out alerts via SMS, if any of the parameters should rise above or fall below a set of predefined thresholds, or if no data is transmitted over a given period of time.

5.3.2 Read-Out Chain

A separate machine handles the data acquisition (DAQ). The Computer is connected to the VME PCI bridge (Caen V2718) over an optical fiber. Figure 22 illustrates the DAQ chain. In a first step, the raw PMT signal is amplified by a factor of ten with a custom-built 16 channel dual-gain amplifier. The amplified signal is then passed to a quad linear Fan in-Fan out module (Caen N625) and relayed to a 16 channel low threshold discriminator (Caen N845) and an eight channel analog to digital converter (ADC) unit (Caen V1730D). The discriminator signal is then used as a trigger to either thee ADC, recording the waveforms, or a 16 channel Scalar module (Caen V260) only registering individual counts. The high voltage (HV) required for operation of the PMTs is supplied by a four channel programmable power supply (Caen V1470). For calibration purposes, two LEDs are placed within close proximity to the photosensors. They are flashed using an Aim-TTi TG5012 pulse generator that also supplies a TTL trigger signal to the ADC.

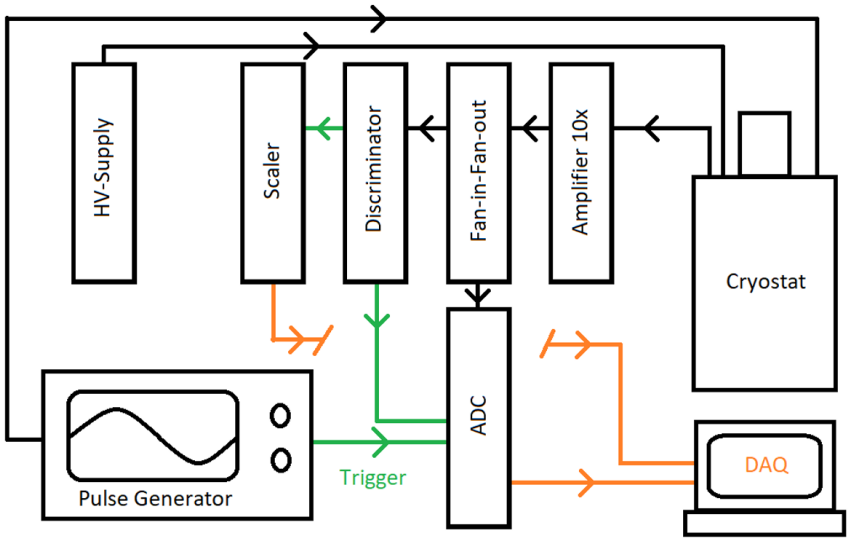

Figure 22: Schematic of the PMT signal read-out. Green arrows indicate signal triggers to the acquisition modules. Orange arrows indicate acquired signal transfer to the DAQ machine.

The V1730D ADC module by Caen has a time resolution of 2 ns and a dynamic range of 2 V. The waveforms recorded were set to consist of 250 for calibration and 1000 individual samples for DC and AP rate determination, the first 100 (500, and 200 for DC, and AP, respectively) of which preceding the trigger for baseline estimation. The total time span of a single event acquisition does therefore not exceed 0.5 µs. The very fine temporal resolution is necessary to accommodate the quick time response of the 2" PMTs.
Most of the acquisitions needed for characterization, save for measurements that require variation in the PMTs' bias voltage, have been automated by a series of bash scripts running periodically by means of a CronJob [9]. Specifically, the ability to remote-control the pulse generator has

[9]The Cron-Daemon facilitates the scheduling of repeated tasks in unix-based systems.

proven to vastly simplify data acquisition and minimize the need for in-person attendance in the laboratory. This was achieved with a USB connection to the DAQ-machine. All tasks regarding gain calibration could be automated in this fashion if a corresponding approach were implemented regarding the Caen V1470 power supply. The only human intervention required is then the switching of the trigger signals from the discriminator and pulse generator to the ADC.

5.3.3 Voltage Divider Circuit

The HV from the power supply is distributed over the individual electrodes of the PMT by means of the voltage divider circuit. To this end, a printed circuit board (PCB), containing the appropriate resistances, usually referred to as the PMT base, is attached to the pins of each PMT. In normal operation, the cathode is biased to the nominal $-1000\,\mathrm{V}$. The total resistance of the resistor chain was set to $125\,\mathrm{M\Omega}$, following the distribution ratio recommended by the manufacturer and resulting in a current of $8\,\mu\mathrm{A}$. Table 1 illustrates the distribution ratio and the resulting voltages on the individual electrodes, with the cathode K, the dynodes D1 to D10, the guard ring GR, and the anodes P.

Electrode	K	D1	D2	...	D10	GR	P
Distribution Ratio	2	1	...	...	1	0.5	
Voltage [V]	-1000	-840	-760	...	-120	-40	0

Table 1: Distribution ratio and electrode voltages of the R12699-406-M4 PMT voltage divider circuit at nominal operation. The potential difference between the dynodes D1 to D10 is of a constant $\Delta\mathrm{V} = 80\mathrm{V}$.

During the characterization presented in this work, the signals arriving at the individual anodes P1 to P4 were summed up to a single signal in P. A detailed schematic of the voltage divider circuit is presented in appendix C. The electronic components, e.g. the resistors and capacitors, were mounted to the PCB via through-hole technology (THT). The leads of the components are passed through holes drilled into the PCB and soldered on the opposite sites. Future variations of the base will feature surface-mounted devices (SMD), where the components are soldered directly to the surface of the PCB.

5.4 The Test-Setup

A support structure, mounted to the cryostat by five threaded rods, serves as the PMT holder. Figure 23a shows a CAD drawing of the setup. Its main components are an aluminium (Al) filler plate with two cavities to fit the photosensors, a polytetrafluoroethylen (PTFE) reflector plate, providing a gap between the PMT windows and finally an Al holder crown that fixes the top two PMTs in place. Because the bodies of the PMTs are at the same potential as their cathodes, i.e. $-1000\,\mathrm{V}$, contact with the metal support structure is to be avoided. To this end, the sensors are placed in PTFE shells providing sufficient insulation to inhibit sparking from the PMT casing to the support structure, which is at ground potential. At a distance of about $25\,\mathrm{mm}$ an additional PTFE and Al plate are attached to the structure. The first is to provide proper spacing and support for the high voltage and signal cabling of the instruments placed in the Al-filler. The latter was designed, produced, and installed in preparation for Run 1. The idea was to exploit the low heat capacity of the material (Al is more cost-efficient than copper) to act as a thermal buffer and minimize temperature fluctuations in the bulk and thus increase system stability.
The placement of the PMTs with their windows facing each other pairwise at a distance of $3\,\mathrm{mm}$,

allows for probing possible light emission under high voltage operation. This would manifest as a change in the dark count rate of a given PMT as a function of time or the bias voltage of the opposing one. Figure 23a indicates the placement of the two LEDs used to calibrate the instruments. In figure 23b their cables are visible passing through the center of the Al holding crown.

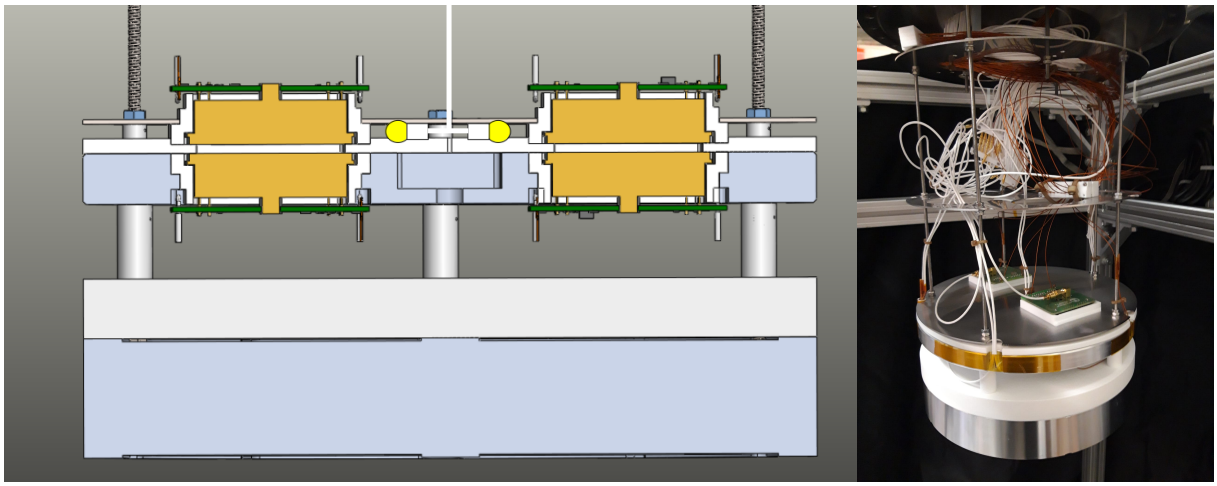

(a) (b)

Figure 23: a) Cross section of the PMT support structure mounted inside the inner cryostat chamber. It supports up to four Hamamatsu R12699 2" PMTs. b) Side view of the assembled PMT test setup.

6 Analysis Methods & Results

Three independent data acquisition campaigns were performed with the goal of characterizing eight units of the 2"-PMTs, labelled by their manufacturer IDs: MA0055, MA0058, MB0072, MB0080, MB0015, MB0090, MB0112 and MB0113. During the stages of data acquisition reported in this work, the read-out of the four individual anodes of the 2" PMT were summed up, resulting in a single read-out per PMT.
The characterization steps consist of testing of three main properties:

i) **Gain Calibration**: Estimate the gain and its dependence on the bias voltage and long-term stability in cryogenic conditions.

ii) **Dark Count Rate**: Estimate the dark count (DC) rate and probe for light emission of the PMTs.

iii) **Afterpulse Rate**: Estimate the afterpulse (AP) rate and its long-term behaviour, when submerged in liquid xenon.

The above steps were repeated in three different experimental conditions with a nominal negative bias voltage of 1000 V. First in vacuum as high as $\mathcal{O}(10^{-7}\,\text{bar})$ and at room temperature, to ensure proper functionality of all PMTs involved, and to have a baseline for comparison with later measurements. A second characterization is performed in xenon gas at a temperature of $\sim$ 174 K with an emphasis on DC rate determination. The scintillating properties of liquid xenon were observed to introduce a substantial amount of additional events, such that the DC rate is systematically estimated too high when probed in the liquid phase. In a last step the PMT properties are determined in liquid xenon with a focus on long-term gain and afterpulse rate stability.

	RT ($p \sim 10^{-5}$ mbar)		GXe ($m_{Xe} \sim 2$ kg)		LXe ($m_{Xe} \sim$ 7-8kg)		Duration [days]
Run 0	55 58				55 58		71
Run 1	55 58	72 80	55 58	72 ~~80~~	55 58	72 ~~80~~	89
Run 2	90 15	~~113~~ 112	90 15	~~113~~ ~~112~~	90 15	~~113~~ ~~112~~	100

Table 2: Overview of the three separate DAQ campaigns. The PMTs are identified by the last two to three digits in their manufacturer IDs. The placements relate to their location relative to each other in the setup. PMTs in a given column are positioned in such a way that their windows face each other. Crossed out names indicate PMTs excluded from analysis but present in the setup. Room temperature measurements were performed in vacuum. The conditions in GXe and LXe are characterized by T=174 K and p=1.8 bar.

This proceeding has been established through iteration. In the first campaign, dubbed Run 0 and undertaken over a period of 71 days, 14 of which in LXe, only two units, MA0055 and MA0058, were available and the separate cold xenon gas filling was omitted. In analysing the data, it became clear that an additional step is necessary to properly identify DCs. It is further motivated by the fact that in the baseline design of the DARWIN observatory, the top array will reside in precisely these conditions.
Run 1 was successfully operated over a period of 89 days (9 and 13 of which in GXe and LXe, respectively) according to the procedure outlined above, collecting data for PMTs MA0055,

MA0058, MB0072, MB0080. The long-term stability campaign however was interrupted by a pipe burst in the faculty building, cutting both the regular electricity and uninterruptible power supply to the cryostat, causing a complete loss of cooling power and forcing emergency recuperation of the valuable xenon. Furthermore, PMT MB0080 exhibited anomalous behaviour and has therefore been excluded from analysis. The observed waveforms appeared to broaden over time, indicating an increase in the read-out's time constant [10]. Indeed, after recuperation the output impedance of the base has increased by several orders of magnitude. The origin of which is currently under investigation.
During Run 2 (spanning 100 days, 7 and 41 of which in GXe and LXe respectively) a fresh batch of 2" PMTs was installed (MB0015, MB0090, MB0112, MB0113). During the room temperature calibration, MB0113 demonstrated the same behaviour as MB0080 in the previous run. The damaged resistor was replaced and MB0113 reinstalled in the setup. After closing and pumping the outer vessel of the cryostat, the resistor suffered damage again and the offending PMT was excluded from the analysis. Additionally, most likely due to thermal contraction of the support structure after introducing the xenon charge, the high voltage (HV) connection to MB0112 failed, causing it to be excluded as well. The campaign was continued with two remaining PMTs, but the long-term stability run was cut short again, this time by a failure of the vacuum pump. The moisture introduced to the insulation vacuum as a result of the pump failure, proved to hinder the re-establishment of the vacuum in a timely fashion, such that the xenon was recuperated again.

6.1 The Single Photoelectron Response

The SPE response is gauged by means of repeated calibration using the pulse generator and LEDs as source and trigger. The gain and SPE resolution are extracted in two distinct methods outlined in sections 6.1.1 and 6.1.2, each performing best at different PMT illumination regimes. That is with different voltages applied to the LED, resulting in varying light intensity. The redundancy is introduced to serve as a cross-check. Given that the two approaches are independent from each other, they rely on different systematics and consistency between the two increases confidence in the results.
The parameters of the calibration signal, i.e. the pulse shape of the LED light, was chosen as a square pulse of 30 ns to 50 ns width with rise and fall time of 5 ns and a permanent offset to the LED voltage of 500 mVpp. The LEDs are flashed at a frequency of 700 Hz. The rather large range in pulse width had to be introduced, because after cooling down the setup thermal contraction presumably shifted the LEDs, or otherwise obstructed the light in such a way that no signals were registered by the PMTs at LED amplitudes below 2 Vpp. Above that threshold, a considerable amount of switching noise is visible in the recorded waveforms, introducing a bias to the gain estimate. Increasing the pulse width boosted the amount of observed light at lower LED voltages without introducing excessive noise to the read-out.
PMT illumination is usually characterized by the *occupancy*, or the average number of photoelectrons produced per trigger. For the two methods outlined in the following, the occupancies were chosen, such that it is close to 2, for the *model independent* estimation, and below 0.1, when *fitting* the charge spectrum. To gauge the occupancy, the PMT signals are connected to an oscilloscope and the LED voltage is increased until signals correlated to the trigger appear. A first series of measurements is then performed, with further incremental increase of the applied voltage to the LEDs. Figure 24a shows an exemplary light level estimation, i.e. the LED voltage dependence of the occupancy, recorded during Run 1 at room temperature. The dependence is interpolated by a polynomial in order to get a rough estimate for the voltage at which the

[10] See appendix B.2

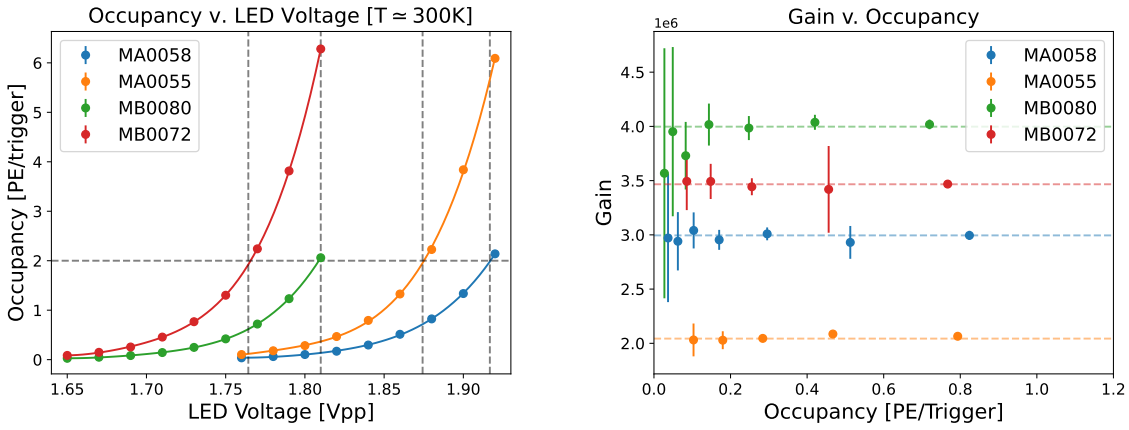

(a) (b)

Figure 24: Light level estimation performed during the initial stages of Run 1 with PMTs MA0058, MA0055, MB0080, and MB0072. (a) Occupancy of each sensor, as a function of the applied LED voltage. The vertical dashed lines indicate the voltage, at which the photosensor on average produces two photoelectrons per trigger. The PMTs sharing the same voltages are facing each other in the test configuration. The discrepancy in occupancy between each pair is a result of the specific placement in the array. The sensors receiving more light are placed on the top of the array, c.f. section 5.4. (b) Individual gains as a function of occupancy. This was performed as a sanity check, since the gain is expected to be independent of the intensity of light in the gain-linear regime. Only values with occupancy < 1.2 are shown to illustrate the large uncertainties in the limit of low illumination.

occupancy assumes the value 2, indicated by the intersection of the horizontal and the vertical dashed lines. In figure 24b, the estimated gains, calculated using the model independent approach, are mapped versus the occupancy as a sanity check of the applied method.

6.1.1 Modelling the SPE Response

The framework described in the following and used for modelling the charge spectra, recorded with low-intensity illumination, has been established in [68]. It hinges on the core assumption of gain linearity, as laid out in section 4.1. The total number of charge carriers produced is a random number $Y = Z + B$, where Z is the amount of charges produced as a direct result of incident photons, and B is the total number of charges due to background processes in the PMT itself and the read-out chain.

Background Charge

The model considers two main sources of background charges $B = Q + D$. Q accounts for random noise arising from each part of the read-out chain, that become noticeable as a fluctuating baseline. The term D encapsulates all other forms of dark current, that closely resemble signal signatures, emanating from PMT internal mechanisms. Included are, for example, thermionic emissions coinciding with the trigger window. The contribution Q from the fluctuating baseline is described by a normal distribution, centered at a mean q_0 with standard deviation σ_0. The component corresponding to instances of the dark current is described by an exponential probability density function (PDF) with rate parameter c_0. The corresponding PDFs then take the form

$$P_Q(x) = \frac{1}{\sqrt{2\pi\sigma_0^2}} exp\left[\frac{-(x-q_0)^2}{2\sigma_0^2}\right]$$
$$P_D(x) = (1-w)\delta(x) + w\theta(x)c_0 \cdot exp(-c_0 x) \tag{17}$$

with the dark count probability w. The PDF of the total background is then computed as the convolution of the two, resulting in the exponentially modified Gaussian (EMG):

$$P_{EMG}(x) = \frac{c_0}{2} \exp\left(\frac{c_0^2\sigma_0^2}{2}\right) exp\left[-c_0(x-q_0)\right] \times erfc\left[\frac{1}{\sqrt{2}}\left(c_0\sigma_0 - \frac{x-q_0}{\sigma_0}\right)\right] \tag{18}$$

The complementary error function is defined as $erfc(x) = 1 - erf(x)$[11].

Signal Charge

The signal charge is dependent on the number of photoelectrons produced at the photocathode. The production process is Poissonian and hence the number of photoelectrons follows $P(k) = e^{-\lambda}\lambda^k/k!$. λ, being the mean photoelectron yield per trigger, is identical to the occupancy introduced above. Each photoelectron, upon striking the first dynode, dislodges a number of secondary electrons, with each following individual multiplication step again following a Poissonian distribution. Given that the first stage gain, i.e. the mean number of secondary electrons produced per photoelectron, is sufficiently large, the central limit theorem states that the total number of charge carriers arriving at the anode, given a single initial photoelectron, is well described by a Gaussian distribution. The PDF of the signal yield is then given by

$$P_Z(x) = \sum_{k=1}^{\infty} \frac{1}{\sqrt{2\pi k\sigma^2}} \frac{e^{-\lambda}\lambda^k}{k!} \times exp\left(-\frac{(x-k\mu)^2}{2k\sigma^2}\right) \tag{19}$$

provided $x > 0$. Here the index of summation k corresponds to the number of initial photoelectrons.

Total Charge

Finally the total PDF can be again computed by taking the product of the characteristic functions of the corresponding contributions. Following the naming convention in [68], the normal distribution will be labeled as $N(x;\mu,\sigma)$ and the EMG as $E_N(x;\mu,\sigma,c_0)$:

$$P_Y(x) = \sum_{k=0}^{\infty} \frac{e^{-\lambda}\lambda^k}{k!} \times \Big[(1-w)N(x; k\mu + q_0, \sqrt{k\sigma^2 + \sigma_0^2}) + wE_N(x; k\mu + q_0, \sqrt{k\sigma^2 + \sigma_0^2}, c_0)\Big] \tag{20}$$

An event containing zero photoelectrons will result in a normal distribution centered around q_0. For $k > 0$ the result is a series of equally spaced Gaussians, multiplied by their respective Poisson probability and corrected for by the EMG. The charge distribution is then modelled by a set of seven independent parameters; The average number of initial photoelectrons, referred to as the occupancy λ, the mean and standard deviation q_0 and σ_0 of the baseline fluctuation, the mean and standard deviation of the SPE distribution μ and σ, the dark count probability w and the corresponding rate parameter c_0.

[11] with the error function $erf(x) = {}^2/\sqrt{\pi}\int_0^x exp(-t^2)dt$

Results

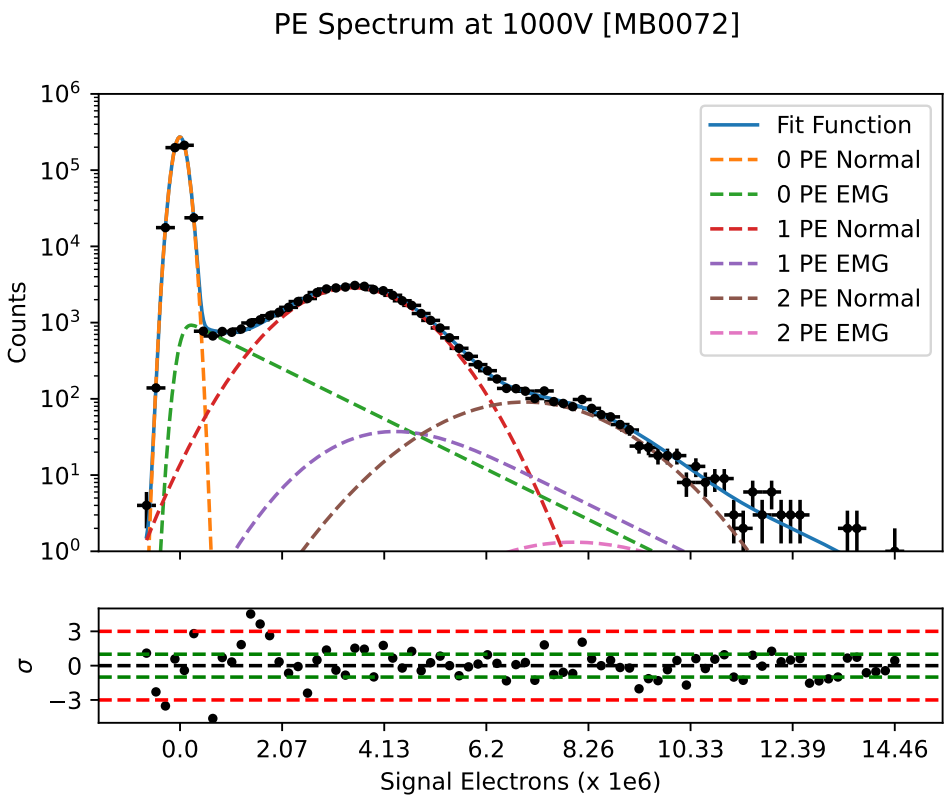

Figure 25: Example of a charge spectrum modelled with the function presented in equation (20) corresponding to the solid blue line with a resulting gain of $(3.49 \pm 0.26) \times 10^6$. The individual contributions are marked by dashed curves. The residuals are shown below, with the green and red dashed horizontal lines indicating deviations from the fit by one and three standard deviations (taken to be Poissonian) respectively.

The charge spectra from low light intensity measurements were modelled in Python implementing the expressions given in equations (18) - (20) [12]. The optimisation was performed by means of a least square fit using the *curve_fit* method implemented in the SciPy [70] library. In order for the fit to converge more reliably the integration window, as depicted in figure 16, was chosen spanning the sample interval $[140, 180]$. Larger windows introduced outliers, for example via inclusion of afterpulses in the charge estimation, that lead to distorted charge spectra. Since the number of fits that are performed is large, and tuning it for each sample individually is very time-consuming, it was more convenient to restrict the integration window and take into account that the charge might be underestimated. For PMT MB0080 specifically, whose time-constant shifted dramatically resulting in a broader waveform, this leads to a grave underestimation of the gain, given that parts of the charge are not being considered. The same is true for the model independent approach, but to a lesser degree, due to the larger integration window. After registering an incident photon, the bias voltage of the offending PMT does not relax back to the median baseline value inside the time frame of the recording.
An example of a modelled charge spectrum is shown in figure 25 [13]. Even after the delicate selection of the integration window outlined above, the quality of the fit varies from data set

[12] For the full code visit [69]
[13] An examplary fit to the charge spectrum of each PMT in provided in the appendix B.

to data set. The results however, are largely consistent overall. However, overestimates of the gain do occur. This is attributed to a systematic underestimation of the occupancy when outliers remain in the data set. To further mitigate the effect of outliers, an additional selection is performed, where only events are considered that fall within the .999-percentile of the recorded distribution. Also, the SPE-response of the individual PMTs is reported as the median of the gains extracted in a given environment. Tables 3 and 4 summarize the main PMT characteristics for each acquisition step and run. The median of the uncertainty estimation on the reported fit parameters, i.e. the gain and occupancy, is supplemented by the arithmetic standard deviation of the reported, given that the values were extracted from up to 38 individual calibration measurements. The characteristics reported here are namely the gain with the corresponding occupancy at which it was recorded, and the SPE-resolution. The systematically lower occupancy of PMTs MA0058, MB0080, and MB0015 are attributable to their placement in the setup. The low-intensity illumination was performed with a single LED voltage per PMT pair. It appears that the sensors placed at the bottom of the setup are less exposed to the light source.
The run 1 data exhibits a clear gain increase when cooling from room temperature down to 174 K of $(13.1 \pm 3.8)\%$ on average. Although expected, this behaviour is absent in the run 2 estimates. This is attributed to the fact that after introducing the xenon to the setup and cooling down to its boiling temperature at 1.8 bar light was no longer detectable at the room temperature light levels. Even after increasing the pulse width to 50 ns the PMTs did not register light at LED voltages below ∼2 Vpp. The resulting waveforms recorded with LED voltage amplitudes above 2 Vpp suffered from switching noise, systematically biasing the gain estimate to lower values. A qualitative examination of this behaviour is still pending.

Run 1

Vacuum (T=296 K)			
PMT	Gain ($\times 10^6$)	Occupancy	SPE Resolution
MA0055	1.953 ± 0.023 (0.489)	0.104 ± 0.010 (0.006)	0.412 ± 0.020 (0.120)
MA0058	3.018 ± 0.056 (0.748)	0.036 ± 0.003 (0.002)	0.398 ± 0.034 (0.115)
MB0072	3.501 ± 0.016 (0.577)	0.084 ± 0.004 (0.004)	0.318 ± 0.009 (0.062)
MB0080	2.180 ± 0.080 (0.408)	0.028 ± 0.004 (0.002)	0.346 ± 0.042 (0.080)
GXe (T=174 K)			
PMT	Gain ($\times 10^6$)	Occupancy	SPE Resolution
MA0055	2.210 ± 0.073 (0.021)	0.053 ± 0.003 (0.005)	0.364 ± 0.032 (0.008)
MA0058	3.450 ± 0.163 (0.045)	0.014 ± 0.004 (0.002)	0.355 ± 0.087 (0.029)
MB0072	4.028 ± 0.028 (0.035)	0.043 ± 0.002 (0.002)	0.300 ± 0.013 (0.007)
MB0080	2.210 ± 0.073 (0.021)	0.053 ± 0.003 (0.005)	0.364 ± 0.032 (0.008)
LXe (T=174 K)			
PMT	Gain ($\times 10^6$)	Occupancy	SPE Resolution
MA0055	2.149 ± 0.070 (0.037)	0.054 ± 0.008 (0.005)	0.386 ± 0.047 (0.013)
MA0058	3.414 ± 0.171 (0.056)	0.031 ± 0.007 (0.003)	0.360 ± 0.065 (0.016)
MB0072	4.072 ± 0.033 (0.031)	0.061 ± 0.004 (0.005)	0.286 ± 0.013 (0.009)

Table 3: Calibration results of the Run 1 data acquisition campaign. The uncertainties reported correspond to the uncertainties on the parameters returned by the fit. The values in brackets are the arithmetic standard deviations over all measurements in a given environment (vacuum, GXe, LXe) combined. The reported gains specifically were calculated as the median gain of the PMT in a given environment, because the estimation produced large outliers biasing the mean towards larger values. The estimates reported for MB0080 were included for completeness, but are gravely underestimated due to the reasons outlined in the above.

Run 2

Vacuum (T=296 K)			
PMT	Gain ($\times 10^6$)	Occupancy	SPE Resolution
MB0015	3.989 ± 0.039 (0.021)	0.038 ± 0.004 (0.002)	0.284 ± 0.019 (0.009)
MB0090	3.264 ± 0.013 (0.015)	0.105 ± 0.004 (0.009)	0.276 ± 0.008 (0.003)
MB0112	3.583 ± 0.029 (0.023)	0.063 ± 0.004 (0.005)	0.295 ± 0.013 (0.004)
GXe (T=174 K)			
PMT	Gain ($\times 10^6$)	Occupancy	SPE Resolution
MB0015	3.670 ± 0.052 (0.026)	0.026 ± 0.004 (0.002)	0.283 ± 0.026 (0.006)
MB0090	2.780 ± 0.014 (0.014)	0.081 ± 0.004 (0.007)	0.281 ± 0.009 (0.005)
LXe (T=174 K)			
PMT	Gain ($\times 10^6$)	Occupancy	SPE Resolution
MB0015	3.684 ± 0.015 (0.022)	0.094 ± 0.004 (0.008)	0.283 ± 0.008 (0.007)
MB0090	2.773 ± 0.009 (0.008)	0.143 ± 0.004 (0.012)	0.279 ± 0.006 (0.003)

Table 4: Calibration results of the run 2 data acquisition campaign. The values in brackets are the arithmetic standard deviations over all measurements in a given environment (vacuum, GXe, LXe) combined. Note that the expected increase in gain when cooling from room temperature to 174 K is absent during this run. The suspicion is that applied voltages above 2 Vpp to the LED introduce a substantial amount of switching noise to the individual waveforms. This results in an underestimate of the overall gain.

Apart from its dependency on temperature, the gain is strongly contingent on the bias voltage. In addition to the regular calibrations, where the nominal negative bias voltage of 1000 V is applied, a separate measurement with variable voltage was conducted. The gains were extracted over a voltage range from 800 V to 1100 V in 50 V steps. The relationship between gain G and bias voltage U is given by [64]:

$$G(U) = a^n \left(\frac{U}{n+1} \right)^{nk} \tag{21}$$

where a and k are constants that determine the relationship between the secondary emission ratio, i.e. the ratio of incoming to outgoing current for a given dynode, and the interstage voltage between dynodes. n is the number of multiplication stages in the PMT (n =10 in the case of the 2" PMT). The data was acquired in vacuum and LXe and is illustrated in figure 26. It is in good agreement with the power-law in equation (21). The SPE resolution is consistent over all applied voltages as depicted in figure 26. The mean SPE response while submerged in LXe over all PMTs tested amounts to a gain of $(3.22 \pm 0.65) \times 10^6$ and a resolution of 0.34 ± 0.04.

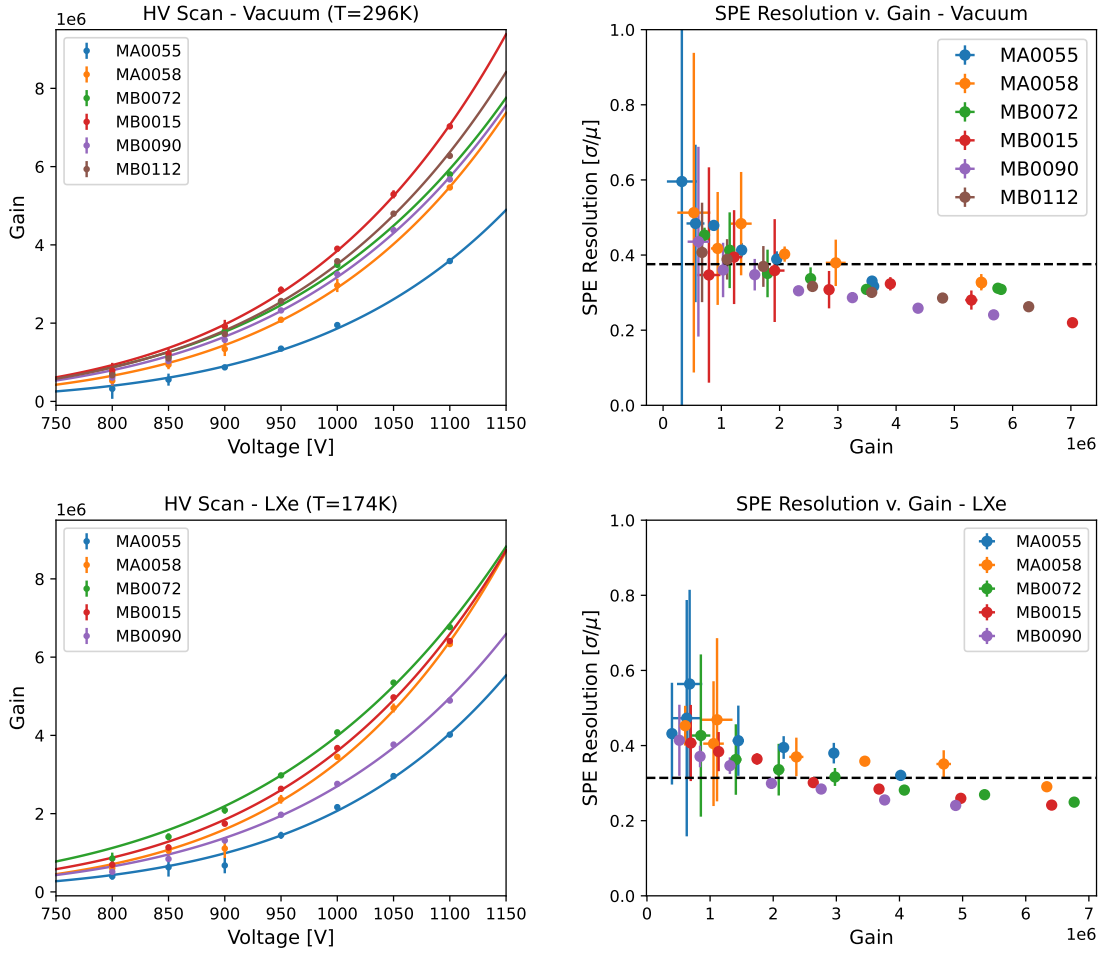

Figure 26: (Left) Gains extracted through fitting the charge spectra recorded at varying bias voltage ranging from 800 V to 1100 V adjusted in 50 V steps. The data was acquired in vacuum at room temperature and LXe at cryogenic temperature. Due to an error during acquisition the values for PMTs MA0055, MA0058 and MB0072 at 1050 V are missing. (Right) Corresponding SPE resolutions as a function of gain. The black dashed lines indicate the mean SPE resolution over all PMTs tested in a given environment.

6.1.2 Model Independent Method

The method outlined in this section was established in [71] and does not assume any specific shape of the SPE distribution or the charge spectrum as a whole. The authors claim that conventional models of the charge spectrum do not take into account the under-amplification of photoelectrons. This is to say that photons and photoelectrons have a non-negligible probability of following a sub-optimal trajectory, such as a photon skipping the photocathode and striking the first dynode, or the photoelectron skipping or inelastically backscattering of the first dynode. These result in a degraded charge arriving at the anode that can skew the mean of the SPE distribution, leading to a reduction of the gain and resolution of the PMT.
Given that the instrument is operated in the linear regime, and that signal and background events are independent from each other, the first two moments of the total charge distribution T are additive:

$$\begin{aligned} E[T] &= E[B] + E[S] \\ V[T] &= V[B] + V[S] \end{aligned} \tag{22}$$

where E and V denote mean and variance of the signal S and background B charge distributions. The signal charge distribution S in terms of the number of photoelectrons p, is given by

$$S(q) = \sum_{p=0}^{\infty} S_p(q) L(p) \tag{23}$$

with the charge distribution $S_p(q)$, given p initial photoelectrons, and a discrete probability distribution $L(p)$ of the number of photoelectrons produced at the cathode. The SPE-response, whose moments are the parameters of interest, is denoted $S_1(q) = \psi(q)$. Under gain linearity, $S_p(q)$ is understood as the p-fold convolution of the SPE-response $\psi(q)$, and their first two moments are related via $E[S_p] = p \cdot E[\psi]$ and $V[S_p] = p \cdot V[\psi]$. Calculating the moments of equation (23) then yields:

$$\begin{aligned} E[S] &= E[\psi] \cdot E[L] \\ V[S] &= V[\psi] \cdot E[L] + E^2[\psi] \cdot V[L] \end{aligned} \tag{24}$$

Plugging this result into equation (22) and solving for the moments of the SPE distribution $E[\psi]$ and $V[\psi]$, and further recognizing that $E[L]$ corresponds to the average number of photoelectrons produced, whereby L is identified again as the Poissonian distribution $L(p) = {}^{\lambda^p}/_{p!} \cdot e^{-\lambda}$ and $E[L] = V[L] = \lambda$, yields:

$$\begin{aligned} E[\psi] &= \frac{E[T] - E[B]}{\lambda} \\ V[\psi] &= \frac{V[T] - V[B] - \lambda E^2[\psi]}{\lambda} \end{aligned} \tag{25}$$

The SPE-response then depends on five parameters; the means and variances of the total and background charge distributions, and the occupancy. The moments of individual charge distributions are calculated as arithmetic mean and variance of a given data sample. In order to properly identify the background events, a separate sample is recorded, where the PMTs are not illuminated. The central moments of the background distribution are then calculated from this *LED-off* sample. The occupancy is estimated from the probability of zero photoelectrons produced:

$$\begin{aligned} L(0) &= e^{-\lambda} \\ \lambda &= -ln(L(0)) \end{aligned} \tag{26}$$

The probability of zero photoelectrons produced can be estimated as the ratio of events, where no light was measured N_0 to the total number of events recorded N in the illuminated sample, i.e. $L(0) = {}^{N_0}/_{N}$. The number of zero light induced PE events N_0 is determined by placing a threshold on the charge spectrum, under which the number of light induced events is expected to be small. The number of empty triggers A_T is then given by the number of events generating a charge below the threshold. The total number of zero PE events is subsequently estimated by placing the same threshold on the blank sample and calculating the fraction f of events, that are background events by construction, below the applied threshold. The estimator of the total number of zero PE events is then $\hat{N}_0 = {}^{A_T}/_{f}$ yielding an occupancy estimator

$$\hat{\lambda} = -ln(\frac{A_T}{fN}) \tag{27}$$

The main source of uncertainty arises from the choice of the threshold. In practice, the threshold is incrementally decreased to find the largest subset of below-threshold events for which the relative error [14] of the occupancy estimator does not surpass 1%.
For all calibration measurements evaluated with this method, the intensity of the illumination was chosen in such a way that the resulting occupancy is $\lambda \sim 2$. This is due to the fact that the variance $V[\hat{E}(\psi)]$ on the SPE mean has a broad minimum at an occupancy of two. The main contribution to the statistical uncertainty on $\hat{E}(\psi)$ stems from the statistical uncertainty on $\hat{\lambda}$.

Results

All results presented in this section, and sections 6.2.1 and 6.2.2, were computed using the *PMT_Analysis* [72] package. It implements the model independent approach to determine the SPE response and features further tools for PMT characterization, which will be outlined in section 6.2.
After setting the light levels, calibration data was taken regularly. The resulting estimates of run 1 and 2 are reported in tables 5 and 6. On average the gains extracted in this fashion increase by $(14.1 \pm 0.7)\%$ after cooling from room temperature down to 174 K, which is consistent with the results stated in the previous section and depicted in figure 31. The HV-dependencies of the gains computed with the model independent approach are illustrated in figure 27. While the estimates on the parameters of equation (21) agree with the model specific results within their respective uncertainties, the estimates on the SPE resolution in LXe exhibit large fluctuations when computed this way. This is attributed to the stronger sensitivity to outliers of the charge spectrum and weaker event selection in the purely statistical approach of the model independent method.

Run 1

Vacuum (T=296 K)

PMT	Gain ($\times 10^6$)	Occupancy	SPE Resolution
MA0055	2.029 ± 0.009 (0.027)	2.330 ± 0.006 (1.051)	0.412 ± 0.009 (0.051)
MA0058	3.076 ± 0.009 (0.224)	2.178 ± 0.004 (0.976)	0.430 ± 0.006 (0.180)
MB0072	3.436 ± 0.015 (0.051)	2.461 ± 0.007 (0.077)	0.404 ± 0.009 (0.016)

GXe (T=174 K)

PMT	Gain ($\times 10^6$)	Occupancy	SPE Resolution
MA0055	2.268 ± 0.015 (0.027)	1.883 ± 0.009 (0.177)	0.427 ± 0.013 (0.012)
MA0058	3.517 ± 0.011 (0.031)	2.120 ± 0.004 (0.164)	0.435 ± 0.006 (0.012)
MB0072	4.033 ± 0.012 (0.057)	1.450 ± 0.003 (0.109)	0.391 ± 0.006 (0.023)

LXe (T=174 K)

PMT	Gain ($\times 10^6$)	Occupancy	SPE Resolution
MA0055	2.233 ± 0.015 (0.029)	2.331 ± 0.010 (0.386)	0.534 ± 0.009 (0.428)
MA0058	3.509 ± 0.011 (0.035)	1.896 ± 0.004 (0.159)	0.428 ± 0.006 (0.330)
MB0072	3.992 ± 0.019 (0.131)	1.974 ± 0.006 (0.292)	0.456 ± 0.009 (0.423)

Table 5: Calibration results of the run 1 data acquisition campaign computed with the model independent approach. Reported are the median gains extracted from regular calibration measurements with the corresponding uncertainties. Given in brackets is the arithmetic standard deviation over the measurements in a given environment.

Finally the calibration campaign is summarized in figure 28, where all operational PMTs remained at constant bias voltage over a period of 10 days for Run 1 and 19 days in Run 2.

[14] For more details on the error estimation see Appendix A

Over the tested duration all instruments behaved stably with an average gain over all PMTs of $(3.26 \pm 0.64) \times 10^6$ and resolution 0.69 ± 0.49 while submerged in liquid xenon (T=174 K, p=1.8 bar), showing again good agreement between the two gain estimation approaches. The average gain fluctuations observed over all PMTs is within ± 1 %, namely within $\pm(0.98 \pm 0.34)$ % and $\pm(0.66 \pm 0.42)$ % in Runs 1 and 2 respectively, which is comparable to the uncertainties on the estimates themselves and showing good agreement between estimation methods. The average gain extracted from fits to the charge spectra is ∼2% lower than from the purely statistical approach. This is to be expected, however. Firstly, this coincides with the aforementioned claim that the disregard of the under-amplified photoelectrons leads to a degradation of the gain estimate. Secondly, the tight integration window chosen in modelling the SPE distribution could also lead to an overall loss in charge.

Run 2

Vacuum (T=296 K)

PMT	Gain ($\times 10^6$)	Occupancy	SPE Resolution
MB0015	3.952 ± 0.013 (0.012)	2.687 ± 0.006 (0.140)	0.396 ± 0.007 (0.004)
MB0090	3.177 ± 0.042 (0.093)	1.966 ± 0.019 (0.121)	0.405 ± 0.026 (0.038)
MB0112	3.448 ± 0.016 (0.085)	2.455 ± 0.008 (0.151)	0.396 ± 0.010 (0.034)

GXe (T=174 K)

PMT	Gain ($\times 10^6$)	Occupancy	SPE Resolution
MB0015	3.802 ± 0.011 (0.012)	1.749 ± 0.003 (0.169)	0.401 ± 0.006 (0.005)
MB0090	2.879 ± 0.023 (0.066)	1.729 ± 0.010 (0.154)	0.391 ± 0.018 (0.035)

LXe (T=174 K)

PMT	Gain ($\times 10^6$)	Occupancy	SPE Resolution
MB0015	3.818 ± 0.012 (0.016)	1.524 ± 0.003 (0.115)	0.565 ± 0.004 (0.480)
MB0090	2.817 ± 0.021 (0.052)	1.666 ± 0.008 (0.131)	0.583 ± 0.009 (0.693)

Table 6: Calibration results of the run 2 data acquisition campaign computed with the model independent approach.

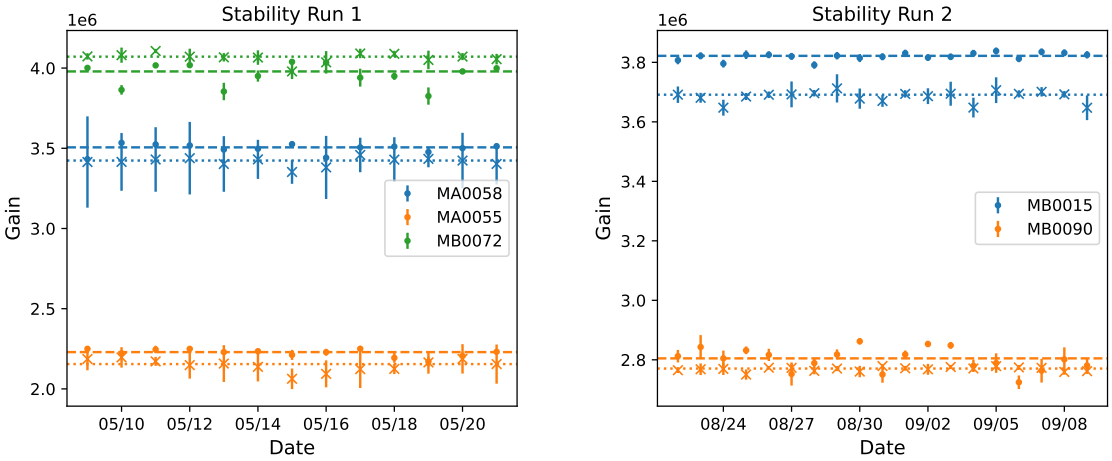

Figure 28: Gains recorded over a period of 13 (19) days in run 1 (run 2). The dots (crosses) correspond to estimates calculated via the model independent (fitting) approach. The dashed (dotted) lines indicate the median gains over the stability period, where the bias voltage was kept constant, as calculated by the model independent (fitting) approach.

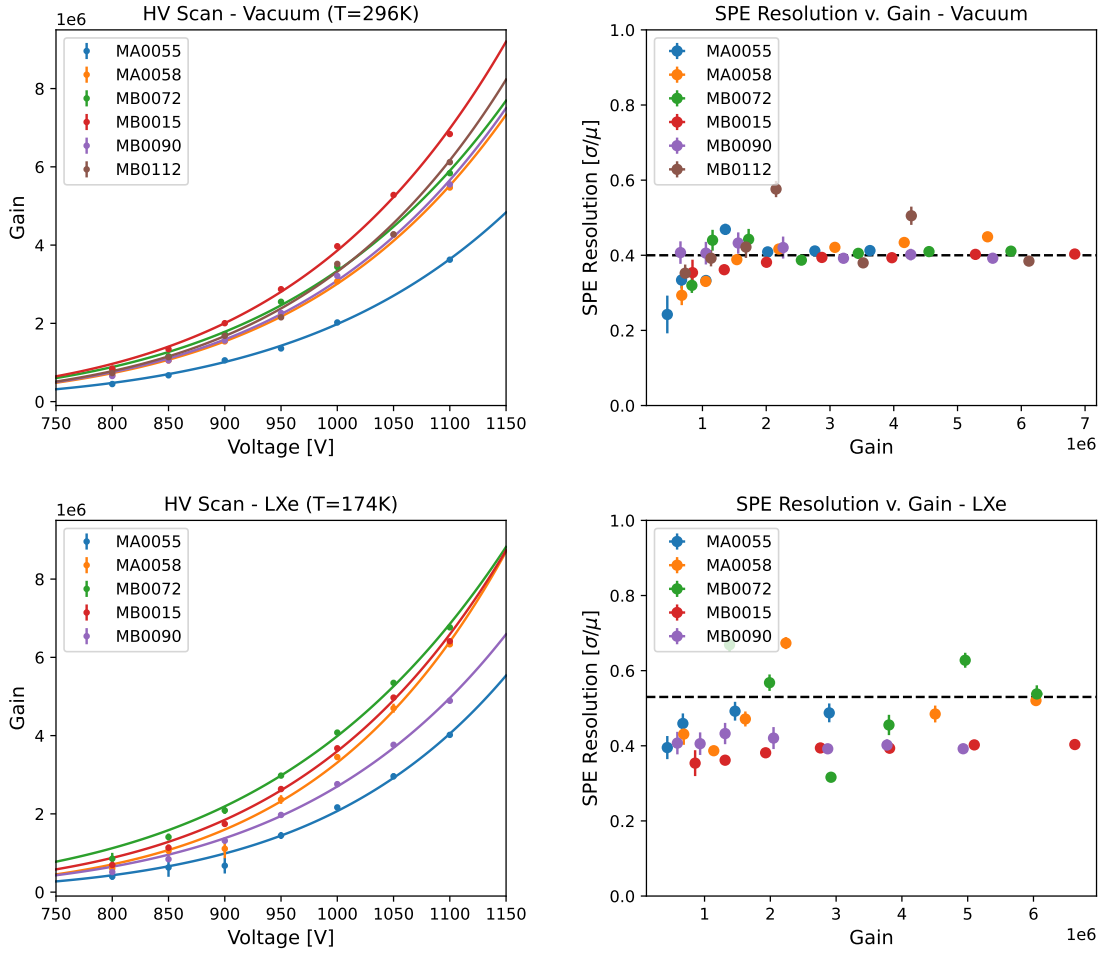

Figure 27: (Left) Gains recorded at varying bias voltage and computed with the model independent approach. The data was acquired in vacuum at room temperature and LXe at cryogenic temperature. Due to an error during acquisition the values for PMTs MA0055, MA0058 and MB0072 at 1050 V are missing. (Right) Corresponding SPE resolutions as a function of gain. The black dashed lines indicate the median SPE resolution over all PMTs tested in the respective environment at the nominal voltage.

6.2 Dark Current Estimation

To determine the intrinsic background contributions of the individual PMTs outlined in section 4.2 a series of measurements were performed. The underlying concept of each is to scan a number of waveforms for deviations of the baseline larger than a given threshold. The choice of threshold relies on the assumption that the amplitude of an induced signal is linearly proportional to the extracted charge. As such, the threshold is conventionally chosen to correspond to a quarter PE-amplitude. Thresholds for each PMT were determined by mapping the measured amplitudes versus the corresponding areas and performing a linear regression, as depicted in figure 29 . The vertical and horizontal dashed lines in figure 29a indicate the area corresponding to 0.25×gain and the respective quarter PE amplitude. The slope of the line governing the area dependence of the amplitude is mainly determined by the time constant of the read-out chain. The observed consistency between all tested PMTs in figure 29b indicates that at the time of this recording, all PMTs operated successfully. The degradation observed in MB0080 became noticeable at a later stage.

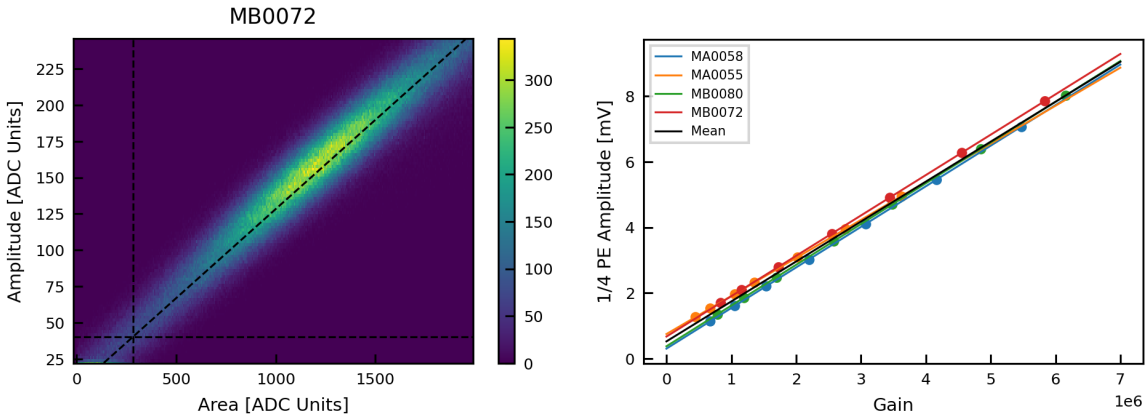

(a) (b)

Figure 29: (a) Histogram of signal amplitude mapped against the corresponding area. The slope of the tilted dashed line determines the linear relationship between a signal's amplitude and the collected charge. The horizontal dashed line indicates the quarter PE-amplitude and the vertical dashed line the corresponding area in ADC units. (b) The quarter PE amplitude as a function of the gain. This plot serves as a sanity check, given that the slope is determined by the read-out chains' time constant.

6.2.1 Dark Counts

DCs are understood as single instances of the dark current. This includes any deviation from the baseline, larger than the given threshold, that is not associated to an induced light pulse. Here, no distinction is made between the exact causes, stated in section 4.2. The data sets recorded for DC rate estimation consist of waveforms of 1000 samples each triggered by the pulse generator at 700 Hz but with no illumination by the LEDs. The waveforms are then scanned for peaks. If a deviation from the baseline is detected, it is registered as a DC. Disentangling the precise origin of the event, however, is not a trivial matter. The contributions from external sources, such as cosmic muons or ambient radiation, influence the overall estimates. To gauge the impact, a series of measurements were conducted, triggering on PMT signals. This was achieved by use of the discriminator. It converts above-threshold signals (in this case signals exceeding

the quarter PE amplitude) into trigger signals that are then fed to the ADC. During the scope of this work, the trigger signal was provided based on signals of a single PMT. The data is then recorded for the PMT pairs facing each other to probe for coincidences. Figure 30 illustrates the coincidences recorded for PMTs MA0058 and MA0055 and triggered on the former. Three main populations can be identified. In figure 30a the overall maximum of the 2D distribution, marked by the red dashed rectangle, distinguishes itself by the fact that PMT MA0058, providing the trigger, records incidences corresponding to $\sim 1\,\mathrm{PE}$, while its neighbour MA0055 registers charges in line with the baseline fluctuations. The vast majority of the instances in this region can therefore be attributed to thermionic emissions of the photocathode of MA0058. The more diffuse population enveloping it is believed to be mainly due to ambient radiation, originating from radioactive isotopes either in the surrounding area or within the PMTs themselves. The final population marked by the orange dashed rectangle in figure 30b and exhibiting large numbers of photoelectrons produced are most likely caused by cosmic muons passing through both PMT windows, creating strongly correlated events in both PMTs. While the cosmogenic events clearly have their origins outside of the PMTs, this sort of distinction cannot be made for the radiogenic events. The distinguishable high PE events contribute less then 10% in the presented sample, recorded in GXe at cryogenic temperatures. Therefore no distinction has been made in estimating the DC rate for each PMT. All instances of baseline deviations larger than the set thresholds were considered as DCs. This results in a conservative estimate of the already low DC rates recorded at cryogenic temperatures.

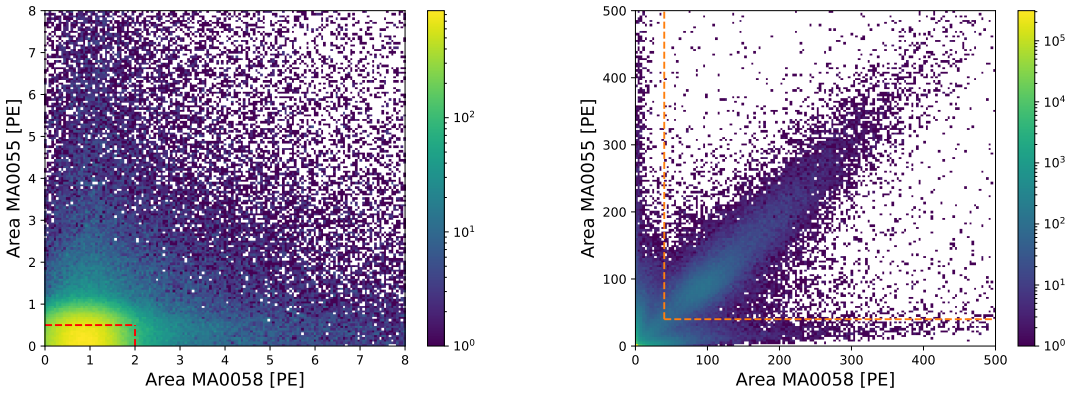

(a) (b)

Figure 30: Instances of DCs recorded by triggering on signals of MA0058 with a discriminator and mapped for coincidences with MA0055 in GXe. (a) The region marked by the red dashed rectangle contains the large majority of counts, which are most likely due to thermionic emissions in MA0058's photocathode. The diffuse population surrounding it is presumed to originate from ambient radiation. (b) The strongly correlated population within the orange dashed rectangle is attributed to cosmic muons.

Finally, to quantify the DC rate estimate a randomly triggered waveform, i.e. triggered by an unilluminated pulse generator trigger, is counted if at any given point the voltage deviates from the baseline by more than the fixed quarter PE threshold. A single waveform, however, can contain more than a single DC event, which is not considered by the applied algorithm. To correct for this matter, the probability of DCs to occur is assumed to be Poissonian. The probability of a waveform to register no event is $P(0;\lambda) = 1 - P(k;\lambda)$, where $k > 0$ and $P(n;\lambda) = \lambda^n/n! \cdot exp(-\lambda)$. An estimate of $P(k;\lambda)$ is given by the ratio of the number of

waveforms containing an above-threshold deviation over the total number of recorded waveforms $^{N_{DC}}/_{N}$. The estimated expectation value λ is then given by

$$\lambda = -ln(1 - \frac{N_{DC}}{N}) \tag{28}$$

It is worth mentioning that given the low DC rate observed during the characterization campaign, the probability of multiple DCs occurring in a single waveform is extremely small. As such the expectation value λ is well described by $\lambda \sim N_{DC}/N$ in retrospect. The overall estimate of the DC rate is computed as the expectation value divided by the time span over which the waveform was recorded, i.e. the number of samples times the temporal resolution of the ADC (2 ns):

$$r_{DC} = \frac{\lambda}{\Delta t} \tag{29}$$

Furthermore, to allow for comparison between different PMT models, the rate is normalized over the effective area of the tube. A comparison with the 3" PMT is presented in section 7. The individual rates are compiled in table 7. The thermal dependence of the rate is illustrated in figure 31. On average the DC rate of a PMT drops to about 3 % of its value at room temperature, when cooled down to 174 K, resulting in a rate of $(0.47 \pm 0.25)\,\mathrm{Hz\,cm^{-2}}$. This behaviour is expected given the thermal nature of the largest contribution to the dark current. The error is given as the spread over all PMTs considered.

DC Rates in $[\mathrm{Hz\,cm^{-2}}]$	MA0058	MA0055	MB0080	MB0072
Room Temp.	24.31 ± 0.45	6.40 ± 0.23	40.57 ± 0.55	57.52 ± 0.66
GXe	0.47 ± 0.06	0.34 ± 0.05	/	0.95 ± 0.08
LXe	0.79 ± 0.08	0.86 ± 0.09	/	0.90 ± 0.09
	MB0015	MB0090	MB0112	
Room Temp.	82.81 ± 0.75	138.45 ± 1.09	105.25 ± 0.95	
GXe	0.25 ± 0.05	0.31 ± 0.05	/	
LXe	0.69 ± 0.08	0.71 ± 0.08	/	

Table 7: Compilation of the estimated DC rates from both characterization campaigns. The Rate was normalized over the effective area of the R12699 2"-PMT to allow for better comparison with other candidate PMTs, provided in chapter 7.

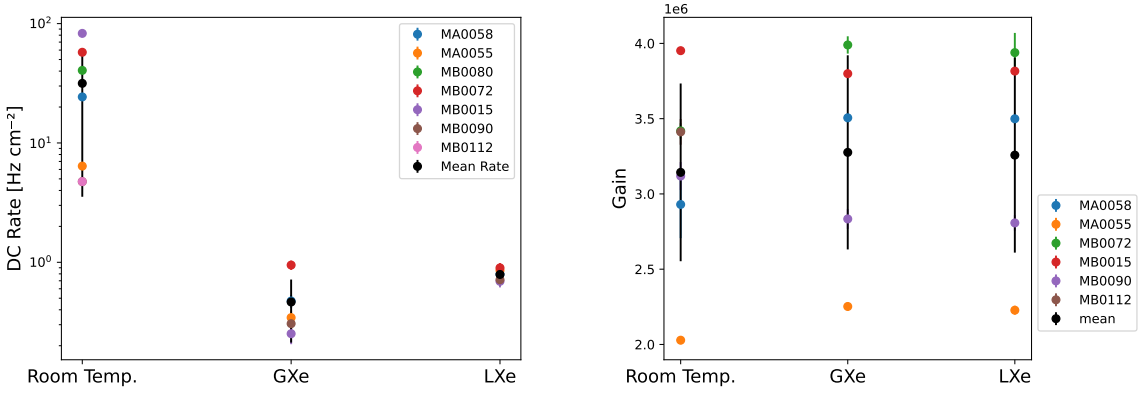

(a) (b)

Figure 31: DC rates (a) and gains (b) as recorded in the different experimental conditions. Given in black are the mean and standard deviations over all units considered in the analysis.

6.2.2 Afterpulsing

The dark current contribution from APs merits a separate investigation, because by definition they occur following an event and are not readily distinguishable from actual signal events. As such they will contribute to the registered charge and bias it to larger values, if not properly identified and separable from the main event preceding them. In rare event searches this is problematic, given that very low statistics are available to reconstruct the energy of the events. This is especially inhibiting if the sought-after event is expected to be of low energy. In order to properly quantify this potential bias, a precise knowledge of the rate at which APs occur is required.
As APs are produced through ionization of residual gases or inelastic backscattering of the first dynode stage, the absolute rate at which they occur can be boosted through an increase in occupancy. The reasoning behind it is that a larger number of electrons traversing the PMT have a higher chance of striking the residual gases or backscattering from the first dynode. The data taken for AP rate estimation is therefore recorded at occupancies ≥ 4 and consists of 1000 samples per waveform, corresponding to a time window of 2 µs to accommodate delayed pulses. The waveforms are processed by a dedicated algorithm included in the PMT_Analysis package. In a first step waveforms not containing a pulse coincident with the trigger, referred to as the main pulse, are discarded. The presence of a pulse is again determined by checking for deviations from the baseline greater than the quarter PE amplitude. In a second step, the waveforms are scanned for a second pulse following the main pulse. This is performed using SciPy's *find_peaks* [70] method. The find_peaks method requires a parameter, corresponding to the deviation of the amplitude of the peak from the baseline. It is given as the number of baseline standard deviations and referred to as prominence. The optimal prominence and minimal time separation between the main and secondary peak was determined to be nine standard deviations and $\Delta t = 10\,\text{ns}$. The optimal values were taken from work [73] preceding this one.

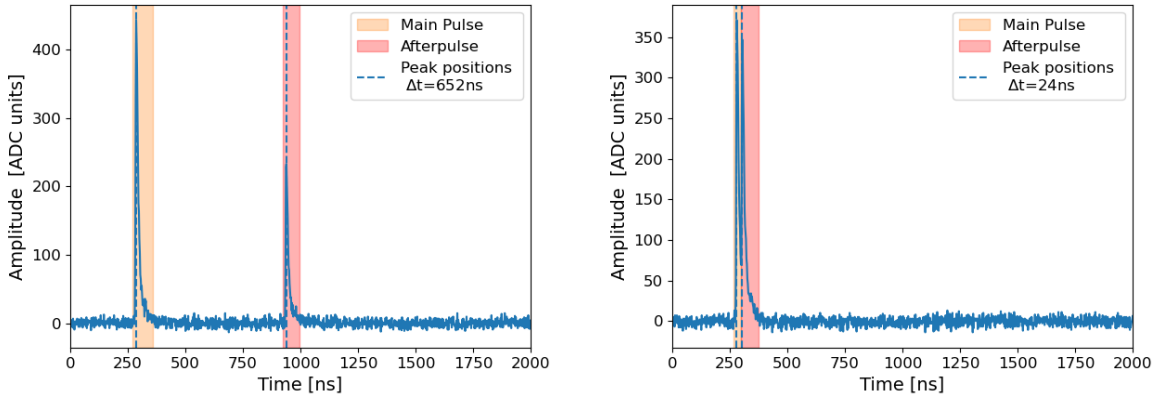

(a) (b)

Figure 32: Side-by-side comparison between separable (a) and unseparable (b) APs. The waveforms were inverted and the units on the y-axis correspond to baseline subtracted ADC bins.

The afterpulse rate is ideally reported in %/PE to have a quantity that does not depend on the occupancy of the recorded data set. The absolute rate is therefore normalized with the occupancy of the main pulse. To quantify the charge generated in the secondary pulse in an unbiased fashion, the separation between the main and secondary pulse needs to be sufficiently large. The requirement implemented in the algorithm is that the main pulse relaxes back to at most 5% of its amplitude before the secondary pulse takes place. Figure 32 illustrates the

merging of unseparable pulses as compared to separable ones. Based on the reduced distance between the photocathode and first dynode of the 2" PMT as compared with its 3" counterpart, the afterpulsing is expected to occur at an order of magnitude faster in the model under study.

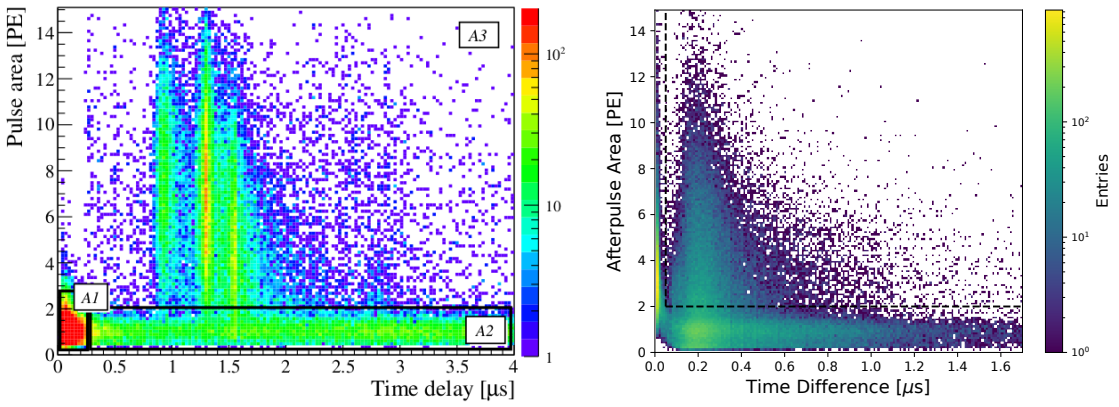

(a) (b)

Figure 33: Side-by-side comparison of AP area v. time spectra of a 3" (a) and 2" PMT (b) recorded at room temperature. (a) The populations marked A1-3 correspond to fast afterpulses (A1) with areas $\leq 2\,\mathrm{PE}$, a steady population over all times with areas $\sim 1\,\mathrm{PE}$, most likely due to DCs entering the waveform at random, (A2) and large area events at distinct times (A3). The distinct populations in A3 are due to specific residual gases. The different timings arise from their different masses, governing the time delay between ionization and arrival time at the photocathode. Figure from [74]. (b) AP area v. time spectrum of a 2" PMT. No populations are distinguishable in the A3 area indicated by the dashed black line. The vast majority of pulses is located in the time interval $0 \leq \Delta t \leq 0.05\,\mu\mathrm{s}$.

This has an adverse effect on the rate estimation as depicted in figure 33, given that only ∼70% of all registered APs recorded in vacuum are separable. The large percentage of unseparable events leads to an overall underestimate of the reported rates in table 8 amounting to an average rate of $(1.17 \pm 0.51)\,\%/\mathrm{PE}$ at room temperature in vacuum and $(1.11 \pm 0.54)\,\%/\mathrm{PE}$ in LXe, with the reported error corresponding to the observed spread over all tested units. Furthermore, the time delay between the main pulse and the afterpulse is dependent on the mass of the ionized residual gas inside the tube. In figure 33a this manifests itself as the three distinct populations at different time delays. The specific offending residual gas can thus be identified. These populations are absent in figure 33b due to the very fast afterpulsing. The individual populations cannot be resolved.

	AP Rate	[%/PE]
PMT	Room Temp.	LXe
MA0058	1.03 ± 0.05	0.71 ± 0.03
MA0055	0.66 ± 0.03	0.78 ± 0.04
MB0072	0.91 ± 0.04	2.17 ± 0.09
MB0015	1.17 ± 0.05	0.81 ± 0.35
MB0090	0.97 ± 0.04	1.07 ± 0.48
MB0112	2.26 ± 0.08	/

Table 8: AP rates recorded during run 1 and 2 in vacuum at room temperature und LXe. The uncertainties are estimated through Gaussian propagation of the Poissonian error on the number of recorded AP-events and occupancy uncertainties. For the run 2 LXe data the light levels where set too high. The model independent method failed to estimate an occupancy. The occupancy was determined through extrapolation from a fit applied to data as depicted in figure 24a. The large errors on the data presented are due to a conservative error set on the occupancy determined in this fashion.

7 Conclusions & Outlook

7.1 Conclusion

A set of 8 units of Hamamatsu R12699-406-M4 multianode photomultiplier tubes was characterized in terms of SPE response and dark current. The goal of characterizing the instruments in an environment closely resembling the TPC scenario was mostly achieved. Five units of the Hamamatsu R12699 flat-panel multianode PMT were successfully characterized in vacuum, GXe, and LXe, and two more in vacuum only. Their SPE response amounts to an average gain of $(3.26 \pm 0.64) \times 10^6$ ($(3.22 \pm 0.65) \times 10^6$), and a mean resolution of (68.91 ± 49.15) % ((31.3 ± 4.5) %) from a model independent (fit) estimation extracted from LXe-data at nominal bias voltage of 1000 V. A similar campaign held in a previous version of the MarmotX test facility, studying the performance of the Hamamatsu R11410 3" PMTs will be used as a base for comparison. The authors tested the 3" PMTs over a period of several months in LXe to finally reach a judgement on the suitability of the sensor for application in the XENON1T experiment [75, 76]. The SPE response reported amounts to a typical gain of $(5.4 \pm 2.1) \times 10^6$ at a nominal bias voltage of 1500 V and SPE resolution of $\sim$27 %, at gains between 2×10^6 to 3×10^6 .
In terms of the dark current the R12699 2" PMT outperforms its cylindrical counterpart by a nearly three times lower DC rate of on average $(0.47 \pm 0.25)\,\mathrm{Hz\,cm^{-2}}$ as compared to the R11410 3" PMTs $(1.37 \pm 0.71)\,\mathrm{Hz\,cm^{-2}}$. The only noticeable drawback is observed in the AP rate. Although the estimated rates are comparatively low, it has to be stressed that the rates reported only include separable APs. The shorter distance between the first dynode and the photocathode of the 2" PMT, as compared to the 3" tube, results in a reduced separation of the main- and afterpulse. As a consequence, a large portion of detected APs are not well separated from the main pulse. The average rate of separable APs observed over all PMTs tested amounts to (1.11 ± 0.54) %/PE in LXe. Whereas the 3" PMTs exhibited an average rate of (8.6 ± 2.2) %/PE. A comparison of the most relevant characteristics of the R12699 and R11410 tubes is summarized in table 9.

PMT type	Gain [$\times 10^6$]	SPE Resolution [%]	DC rate [$\mathrm{Hz\,cm^{-2}}$]	AP rate [%/PE]
R12699	3.22 ± 0.65	31.3 ± 4.5	0.47 ± 0.25	1.11 ± 0.54
R11410	5.4 ± 2.1	$\sim$27	1.37 ± 0.71	8.6 ± 2.2

Table 9: Average SPE response and dark current estimations of the R12699 and R11410 [75] PMTs. The SPE response reported here was calculated by applying the model outlined in section 6.1.1. All results were obtained from data recorded for PMTs submerged in LXe with the exception of the DC rate, which was determined in the gas phase at cryogenic temperatures. The value reported for the 3" PMTs was estimated for data recorded at gains ranging from 2×10^6 to 3×10^6

Although some key requirements still need to be tested, the R12699 appears to be a promising candidate for future DM observatories. It exhibits a comparable ability to resolve the SPE response while outperforming its counterpart in terms of the DC rate. During the stability tests in LXe, albeit cut short by external factors, all PMTs tested exhibited satisfactory gain stability. The caveat introduces itself in the form of its quick time response, tending to merge APs into the main signal and thus creating a potential bias in energy reconstruction. The bias would take place, if an AP merges with the main pulse while remaining undetected, resulting in an increase of the registered charge. For rare low-energy event searches, this could prove to be problematic and further insight is required to properly quantify this effect.

7.2 Outlook

The next steps to complete the characterization of the R12699 tube include a dedicated test of the separate anode readout and a calibration with a radioactive source, as a proof of concept of the instrument's ability to record and reconstruct physical events of known energy. In preparation for these undertakings, however, debugging of the two PMTs, namely MB0080 and MB0113, exhibiting faulty behaviour, is required. It is important to stress that the PMTs themselves aren't defective, as verified by dedicated tests at room temperature in a dark room with a replacement base, but that more likely the polarity of the voltage applied to the instruments is at the root of the problem. Applying a negative bias voltage, as is recommended by the manufacturer, results in the casing of the PMT being at voltage instead of at ground potential. The defect in the output impedance could therefore be due to sparking from the casing to the base, resulting in a momentary rise in current large enough to damage the resistor. The question as to why it happened repeatedly for the same two units while the rest was unaffected remains. The two offending units were placed in different locations inside the setup and multiple internal connections to the power supply and read-out were tested during the initial troubleshooting. The one thing the units have in common is a comparatively higher gain. Also, circumstantial causes cannot be ruled out at the moment. Such as a repeated placement of the base at an angle to the PMT body, resulting in decreased distance between the body and the circuitry, mounted via THT. A measure that was attempted was the placement of fine sheets of PTFE, placed between the body and the base to provide further insulation. The problem, however, persisted. As an additional measure, an update to the bases, changing from THT to SMD, could be implemented, to further increase the distance and isolation between the body and the components on the PCB.

A second preliminary step before the continuation of the characterization campaign could be an upgrade of the test setup. The inner vessel of the MarmotX cryostat has sufficient space to host all eight units of 2" PMTs available at this time. A simple modification of the Al-filler plate and -holder crown, as well as the PTFE reflector, described in section 5.4, would effectively halve the time required to characterize all units in realistic TPC environments.

The calibration by radiation will be performed by introducing meta-stable krypton isotopes (^{83m}Kr), emanating from a rubidium-83 source, into the inner vessel. The source is placed in a chamber integrated in the recirculation system depicted in figure 20. The ^{83m}Kr diffuses into the xenon and is transported to and uniformly distributed inside the inner vessel. It de-excites into ^{83}Kr in a two-step process, emitting in the first step conversion and auger electrons. In the second step, γ-radiation is emitted, resulting in two low energy spectral lines of 32.1 keV and 9.4 keV. The intermediate excited state of ^{83}Kr has a half-life of 154 ns, allowing the observation of correlated events, while the half-live of ^{83m}Kr is < 2 h. The comparatively short half-life of the meta-stable state and its two distinct and subsequent decays make it a good probe, given that a few hours after the calibration the vast majority will have decayed, leaving no lingering radioactive contamination in the xenon [77]. The remaining inert ^{83}Kr is collected by the getter, used for purifaction.

Finally, the individual anode read-out will be employed in a kg-scale TPC designed for the MarmotX PMT testing facility. A preliminary design is depicted in figure 34. This serves an additional purpose of testing the 2" PMTs' functionality within an aspect so far neglected in this work. Two-phase TPCs require the PMTs to operate close to, or in strong electric fields, e.g. $\mathcal{O}(10\,\mathrm{kV\,cm^{-1}})$ [59] between the gate and the anode. The TPC will feature an aspect ratio of 2:1 and a target mass of roughly 10.7 kg of xenon within the current inner vessel. It is 23.2 cm in diameter and has a separation from cathode to anode of 7.0 cm. Four 2" PMTs each will be affixed in an array at the top, as well as at the bottom of the detector. The anodes of the sensors placed in the top array will be read out separately for a total of 16 channels. Seven copper field-

shaping rings are in place to ensure field uniformity at the fringes of the active mass, which will be surrounded by a cylindrical PTFE reflector. Given the square shape of the instruments, it is unfortunately not possible to exploit their full photocathode coverage within the confines of the inner vessel. The radius of the reflector was therefore chosen in such a manner that only the PMT pixels furthest from the central axis are covered, while at the same time minimizing the ratio of dead v. active area. The height of the GXe/LXe interface will be controlled by a weir, adjustable via a motion feed-through. The liquid is then collected in a cup and extracted into a heat exchanger to vaporize before entering the recirculation system.
In addition to its purpose as a proof of concept for the 2" PMTs, the TPC is expected to be able to accurately measure key features in LXe-based TPCs, such as the electron drift velocity and the W-factor in equation (15). A new independent measurement of the latter could shed some light on the tension that arose recently, described in section 3.2. A base design, depicted in figure 34, was already established in CAD within the scope of this project, missing only the meshes of the dynodes responsible for the drift and extraction fields. The majority of necessary materials are in place and production is expected to start in the first half of 2024.

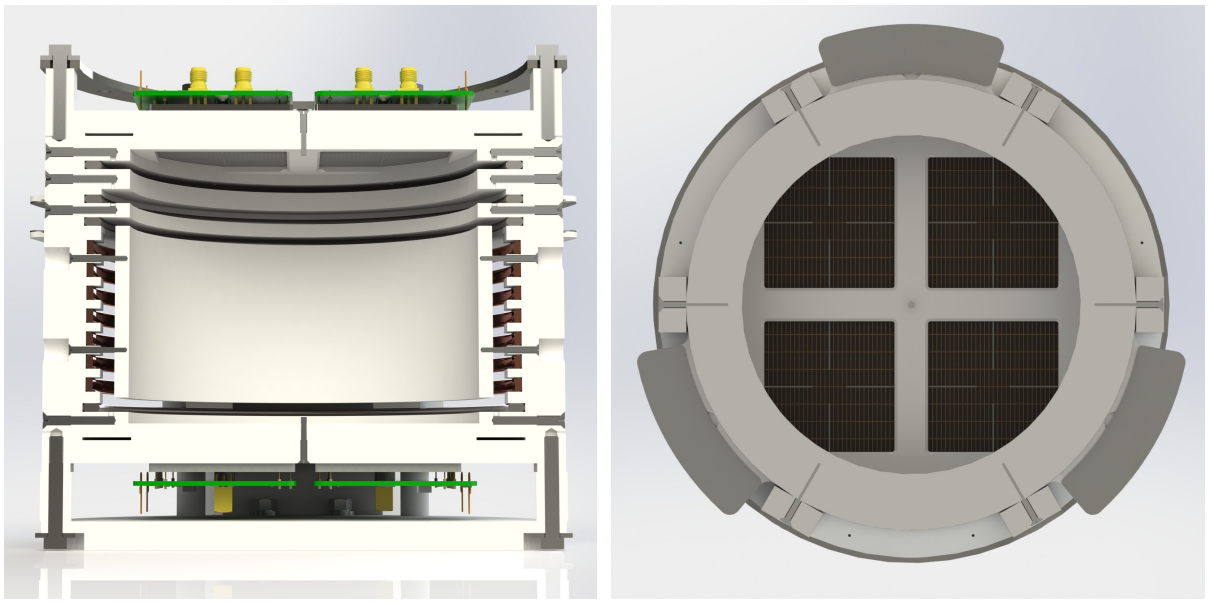

(a) (b)

Figure 34: CAD renders of the preliminary design of the kg-scale TPC for MarmotX. (a) Cross section illustrating the ∼7 cm maximum drift length of the TPC. (b) Bottom view of the top array.

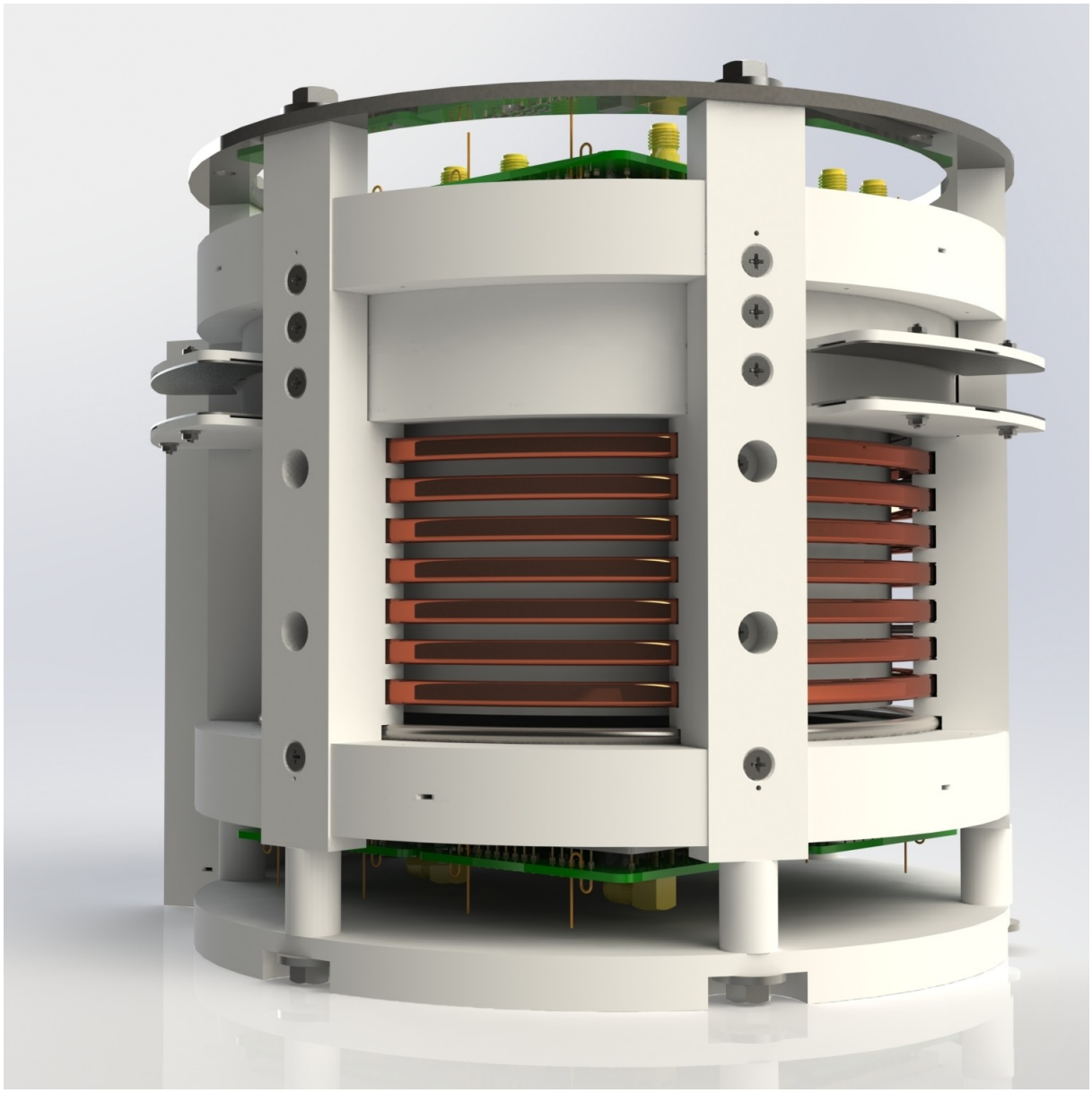

Figure 35: CAD render of the preliminary design of the kg-sclae TPC for MarmotX

Appendix

A Uncertainty Estimation

In the following an outline is provided for the uncertainty estimations of the different approaches and characteristics. The errors on the reported averages over all PMT units correspond to the observed spread and are given as the square roots of the arithmetic variance.

Modelling the SPE response

The uncertainties reported in section 6.1.1 correspond to the parameter $\hat{a}$ uncertainties returned by the applied least-squares fit, as the deviation from the minimum of the χ^2-distribution:

$$\chi^2(a \pm \hat{\sigma}) = \chi^2(\hat{a}) + 1 = \chi^2_{min} + 1$$

Given that upon visual inspection the quality of the individual fits exhibited a degree of variation not reflected in the estimated uncertainties, the observed spread of the reported estimates over each individual data acquisition is further provided. This should serve as a cross check and base for comparison.

Model Independent Method

The statistical uncertainties in the model independent approach are computed as in [71]:

$$\begin{aligned} V\left[\hat{E}[\psi]\right] &\simeq \frac{\lambda(E^2[\psi] + V[\psi]) + 2V[B]}{N\lambda^2} + \frac{E^2[\psi](e^\lambda + 1 - 2f)}{fN\lambda^2} \\ V\left[\hat{V}[\psi]\right] &\simeq \frac{(E^2[\psi] - V[\psi])^2(e^\lambda + 1 - 2f)}{fN\lambda^2} \\ V\left[\hat{\lambda}\right] &\simeq \frac{e^\lambda + 1 - 2f}{fN} \end{aligned}$$

with the estimated SPE responses $\hat{E}[\psi]$ and $\hat{V}[\psi]$. An additional contribution from propagating the uncertainty of the occupancy into the mean of the SPE distribution as given in equation 25 is included also. The overall reported uncertainty amounts to the sum of squares of the individual contributions.

Dark Counts & Afterpulsing

Given that DC and AP rate estimation are both counting experiments ,the uncertainties reported for the DC and AP rates are given as their respective Poissonian uncertainties, with error propagation where appropriate.

B Supplementary Plots

B.1 Exemplary Fits

In the following a number of fits to the charge spectra of each PMT included in the analysis is shown. Note that for units with comparatively higher gain, i.e. units MB0072 and MB0015, the function presented in equation 20 struggles to properly model the pedestal between the SPE peak and the baseline normal. This supports the assumption made by the authors of [71], that under amplified electrons are not properly taken into account by analytic descriptions of the charge spectrum.

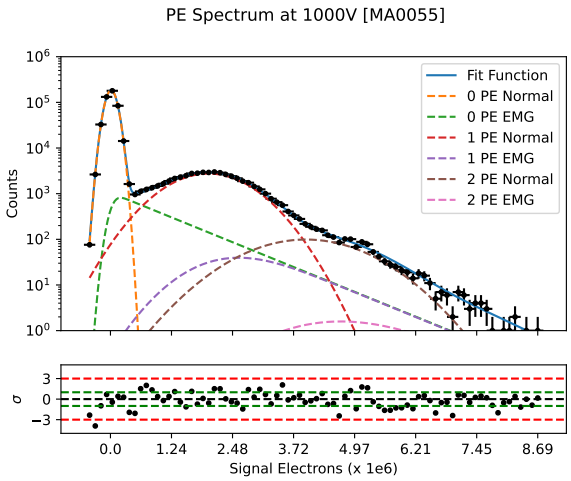

(a) Room Temp.

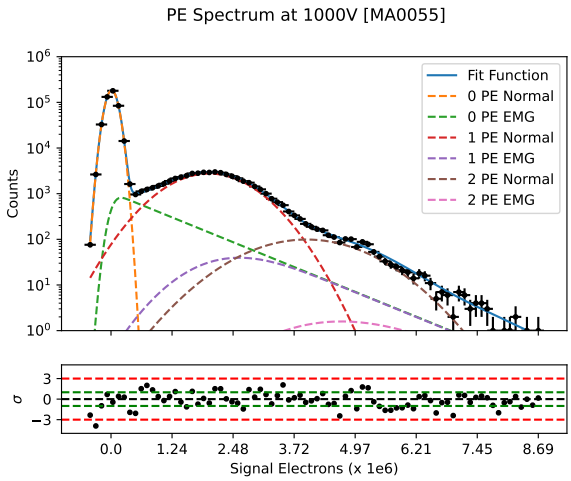

(b) LXe

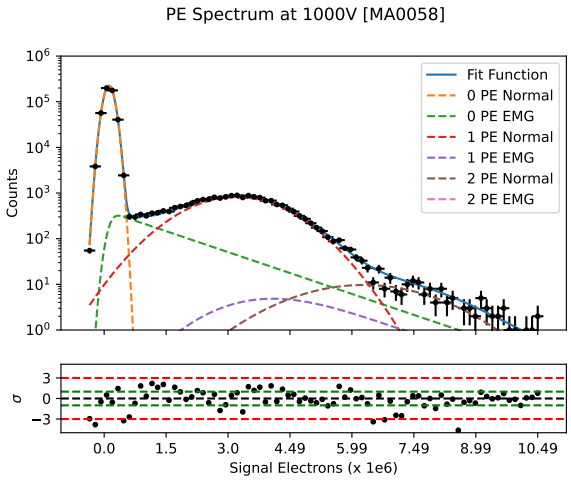

(a) Room Temp.

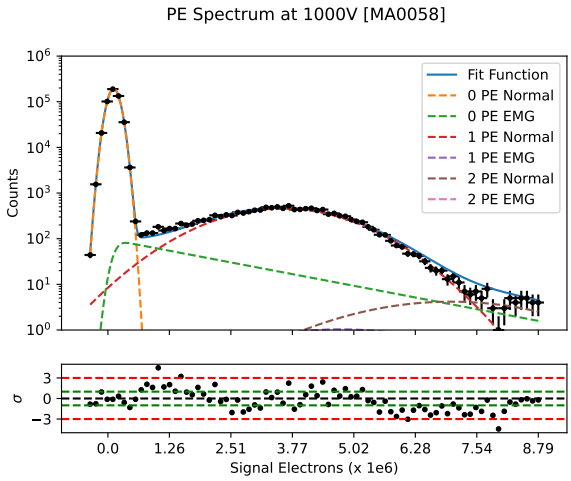

(b) LXe

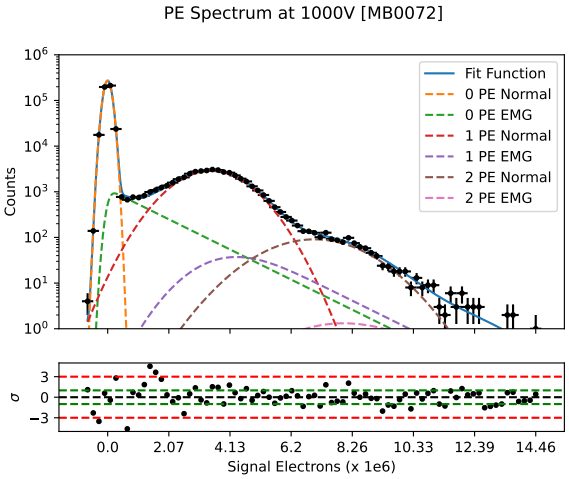

(a) Room Temp.

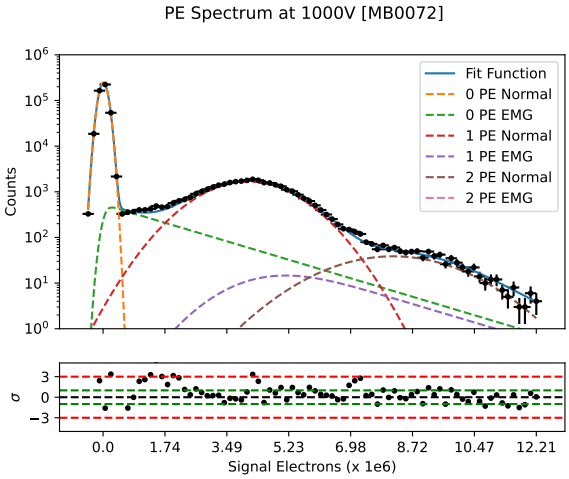

(b) LXe

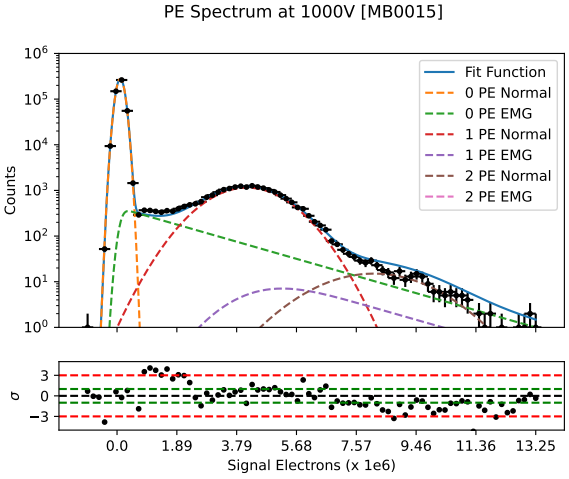

(a) Room Temp.

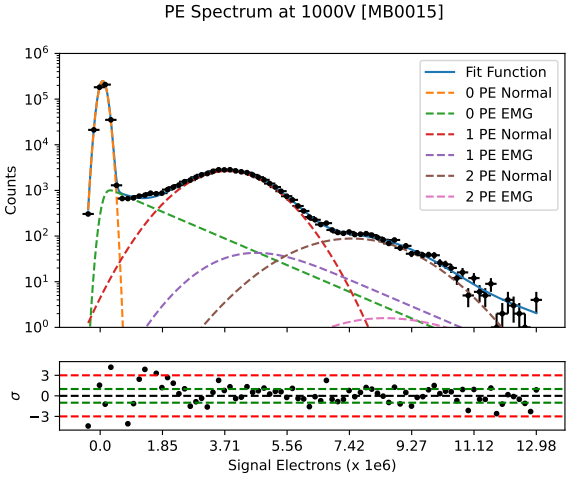

(b) LXe

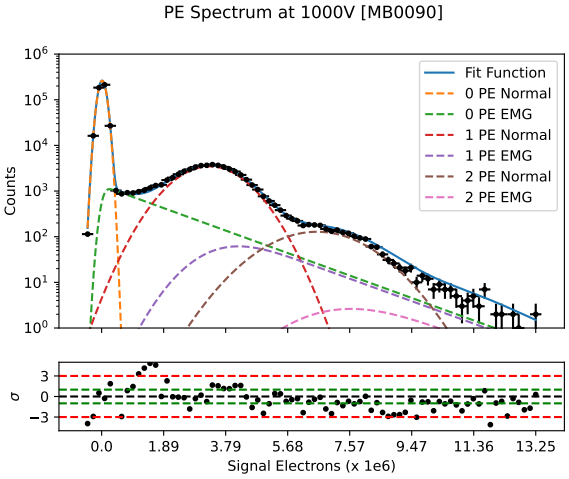

(a) Room Temp.

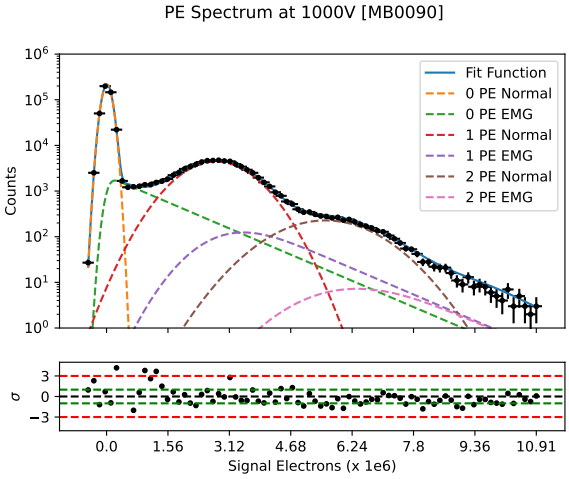

(b) LXe

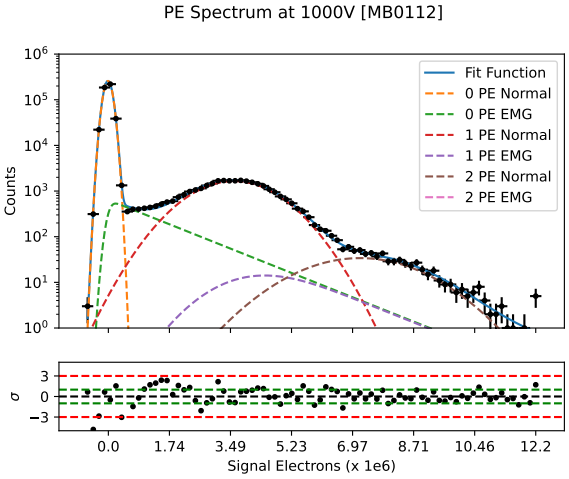

(a) Room Temp.

B.2 Waveform Broadening

Depicted below are the mean waveforms of the two units that exhibited an increase in their read-out time constant after first commissioning. The blue curves were recorded during the first few days of operation in the context of light level estimation. The orange curves are the recordings of the first calibration measurements.

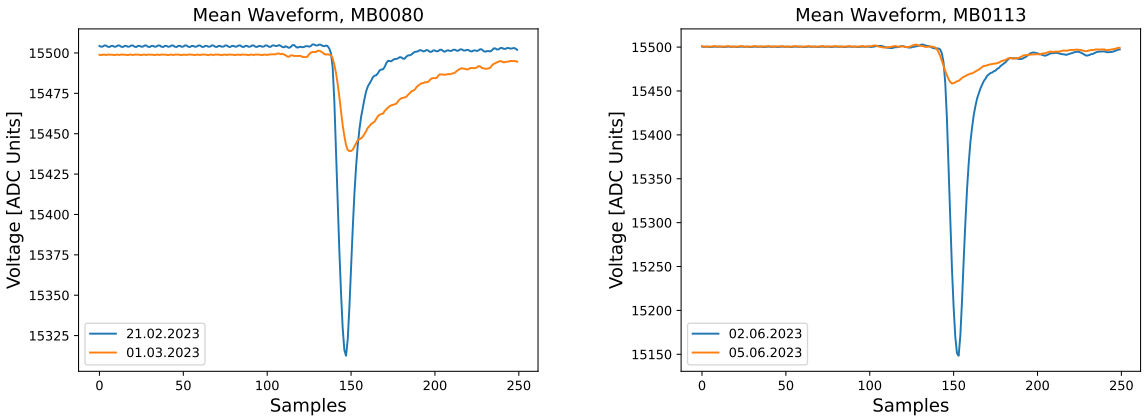

C Voltage Divider Circuit

Schematic of the voltage divider circuit with summed read-out of the four individual anodes.

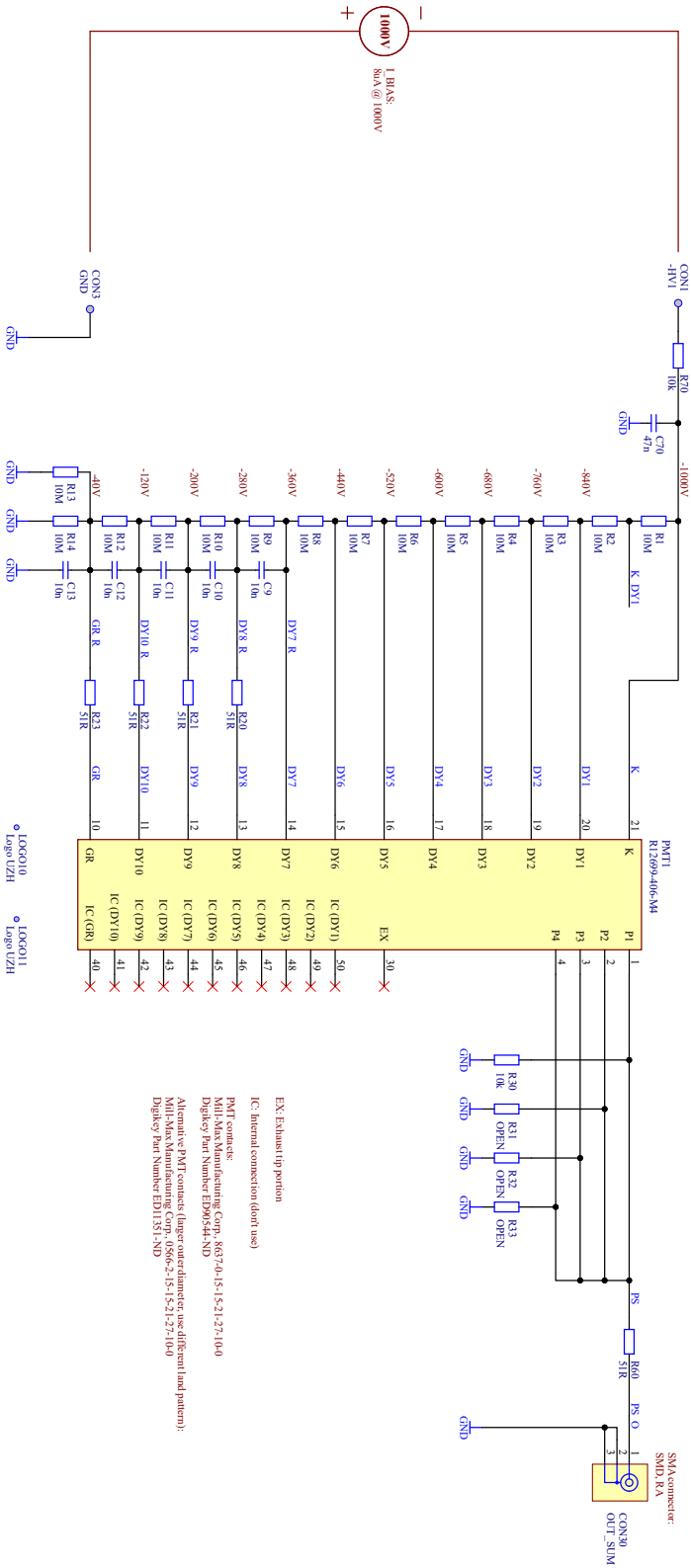

References

[1] Particle Data Group collaboration, *Review of Particle Physics*, PTEP **2022** (2022) 083C01.

[2] G. Bertone, D. Hooper and J. Silk, *Particle dark matter: evidence, candidates and constraints*, Physics Reports **405** (2005) 279.

[3] Y. Fukuda, T. Hayakawa, E. Ichihara, K. Inoue, K. Ishihara, H. Ishino et al., *Evidence for oscillation of atmospheric neutrinos*, Physical Review Letters **81** (1998) 1562.

[4] ATLAS collaboration, *Observation of a new particle in the search for the Standard Model Higgs boson with the ATLAS detector at the LHC*, Physics Letters B **716** (2012) 1.

[5] G. F. Giudice, *Naturally speaking: The naturalness criterion and physics at the LHC*, in *Perspectives on LHC Physics*, pp. 155–178, WORLD SCIENTIFIC, (jan, 2008), DOI.

[6] S. Dodelson, *Modern Cosmology*. Academic Press, Amsterdam, 2003.

[7] S. Perlmutter, G. Aldering, G. Goldhaber, R. A. Knop, P. Nugent, P. G. Castro et al., *Measurements of* Ω *and* Λ *from 42 high-redshift supernovae*, The Astrophysical Journal **517** (1999) 565.

[8] F. Zwicky, *Die Rotverschiebung von extragalaktischen Nebeln*, Helvetica Physica Acta **6** (1933) 110.

[9] V. C. Rubin and J. Ford, W. Kent, *Rotation of the Andromeda Nebula from a Spectroscopic Survey of Emission Regions*, The Astrophysical Journal **159** (1970) 379.

[10] D. Clowe, A. Gonzalez and M. Markevitch, *Weak-lensing mass reconstruction of the interacting cluster 1E 0657–558: Direct evidence for the existence of dark matter*, The Astrophysical Journal **604** (2004) 596.

[11] R. Massey, T. Kitching and J. Richard, *The dark matter of gravitational lensing*, Reports on Progress in Physics **73** (2010) 086901.

[12] M. Milgrom, *A modification of the newtonian dynamics as a possible alternative to the hidden mass hypothesis.*, The Astrophysical Journal **270** (1983) 365.

[13] D. Clowe, M. Bradač, A. H. Gonzalez, M. Markevitch, S. W. Randall, C. Jones et al., *A direct empirical proof of the existence of dark matter*, The Astrophysical Journal **648** (2006) L109.

[14] A. Einstein, *Die Grundlage der allgemeinen Relativitätstheorie*, Annalen der Physik **354** (1916) 769.

[15] R. Gavazzi, T. Treu, L. V. E. Koopmans, A. S. Bolton, L. A. Moustakas, S. Burles et al., *The Sloan Lens ACS Survey. VI. Discovery and Analysis of a Double Einstein Ring*, **677** (2008) 1046.

[16] M. Bartelmann and P. Schneider, *Weak gravitational lensing*, Physics Reports **340** (2001) 291.

[17] A. Jenkins, *Frontier fields - archived blog*, [Online] available on https://frontierfields.org/category/new-data/, (accessed: Oct. 2023) .

[18] S. Jha, *Molten ring galaxy*, [Online] Rutgers, The State University of New Jersey, available on https://hubblesite.org, (accessed: Oct. 2023) .

[19] A. A. Penzias and R. W. Wilson, *A measurement of excess antenna temperature at 4080 Mc/s.*, The Astrophysical Journal **142** (1965) 419.

[20] R. A. Alpher, H. Bethe and G. Gamow, *The origin of chemical elements*, Phys. Rev. **73** (1948) 803.

[21] W. Hu and S. Dodelson, *Cosmic microwave background anisotropies*, Annual Review of Astronomy and Astrophysics **40** (2002) 171.

[22] D. J. Fixsen, *The temperature of the cosmic microwave background*, The Astrophysical Journal **707** (2009) 916.

[23] PLANCK collaboration, *Planck legacy archive*, [Online] available on https://wiki.cosmos.esa.int/planck-legacy-archive/index.php/CMB_maps (accessed: Oct. 2023) .

[24] PLANCK collaboration, *Planck 2018 results*, Astronomy & Astrophysics **641** (2020) A6.

[25] S. D. McDermott, H.-B. Yu and K. M. Zurek, *Turning off the lights: How dark is dark matter?*, Physical Review D **83** (2011) 063509.

[26] B. Bozek, D. J. E. Marsh, J. Silk and R. F. G. Wyse, *Galaxy UV-luminosity function and reionization constraints on axion dark matter*, Monthly Notices of the Royal Astronomical Society **450** (2015) 209.

[27] M. A. Monroy-Rodríguez and C. Allen, *The end of the macho era, revisited: new limits on macho masses from halo wide binaries*, The Astrophysical Journal **790** (2014) 159.

[28] A. M. Green and B. J. Kavanagh, *Primordial black holes as a dark matter candidate*, Journal of Physics G: Nuclear and Particle Physics **48** (2021) 043001.

[29] M. Lisanti, *Lectures on dark matter physics*, in *New Frontiers in Fields and Strings*, WORLD SCIENTIFIC, Nov., 2016, DOI.

[30] J. I. Read, *The local dark matter density*, Journal of Physics G: Nuclear and Particle Physics **41** (2014) 063101.

[31] D. Baxter, I. M. Bloch, E. Bodnia, X. Chen, J. Conrad, P. D. Gangi et al., *Recommended conventions for reporting results from direct dark matter searches*, The European Physical Journal C **81** (2021) .

[32] J. Lewin and P. Smith, *Review of mathematics, numerical factors, and corrections for dark matter experiments based on elastic nuclear recoil*, Astroparticle Physics **6** (1996) 87.

[33] M. C. Smith, G. R. Ruchti, A. Helmi, R. F. G. Wyse, J. P. Fulbright, K. C. Freeman et al., *The RAVE survey: constraining the local Galactic escape speed*, Monthly Notices of the Royal Astronomical Society **379** (2007) 755.

[34] R. A. Ibata, G. Gilmore and M. J. Irwin, *A dwarf satellite galaxy in Sagittarius*, **370** (1994) 194.

[35] M. Kuhlen, N. Weiner, J. Diemand, P. Madau, B. Moore, D. Potter et al., *Dark matter direct detection with non-maxwellian velocity structure*, Journal of Cosmology and Astroparticle Physics **2010** (2010) 30.

[36] E. Kolb and M. S. Turner, *The Early Universe*. CRC Press, 1st ed., 1990.

[37] Particle Data Group, R. L. Workman, V. D. Burkert, V. Crede, E. Klempt, U. Thoma et al., *Review of Particle Physics*, Progress of Theoretical and Experimental Physics **2022** (2022) 083C01.

[38] G. Jungman, M. Kamionkowski and K. Griest, *Supersymmetric dark matter*, Physics Reports **267** (1996) 195.

[39] T. D. Brandt, *Constraints on macho dark matter from compact stellar systems in ultra-faint dwarf galaxies*, The Astrophysical Journal Letters **824** (2016) L31.

[40] A. Boyarsky, J. Lesgourgues, O. Ruchayskiy and M. Viel, *Realistic sterile neutrino dark matter with keV mass does not contradict cosmological bounds*, Phys. Rev. Lett. **102** (2009) 201304.

[41] A. Ringwald, *Exploring the role of axions and other WISPs in the dark universe*, Physics of the Dark Universe **1** (2012) 116.

[42] F. Zimmerman, *Towards a circular higgs and electroweak factory*, The European Physical Society Conference on High Energy Physics (EPS-HEP2021) (2021) .

[43] ATLAS collaboration, *Combination of searches for invisible higgs boson decays with the ATLASexperiment*, Phys. Rev. Lett. **122** (2019) 231801.

[44] C. P. de los Heros, *Status of direct and indirect dark matter searches*, European Physical Society Conference on High Energy Physics, Jul., 2020.

[45] M. Schumann, *Direct detection of WIMP dark matter: concepts and status*, Journal of Physics G: Nuclear and Particle Physics **46** (2019) 103003.

[46] E. Armengaud, Q. Arnaud, C. Augier, A. Benoît, L. Bergé, T. Bergmann et al., *Performance of the EDELWEISS-III experiment for direct dark matter searches*, Journal of Instrumentation **12** (2017) P08010.

[47] SuperCDMS collaboration, *SuperCDMS SNOLAB - Status and Plans*, J. Phys. Conf. Ser. **1342** (2020) 012077.

[48] A. Abdelhameed, G. Angloher, P. Bauer, A. Bento, E. Bertoldo, C. Bucci et al., *First results from the CRESST-III low-mass dark matter program*, Physical Review D **100** (2019) .

[49] M. Lai, *Recent results from DEAP-3600*, Journal of Instrumentation **18** (2023) C02046.

[50] E. Aprile, J. Aalbers, F. Agostini, M. Alfonsi, L. Althueser, F. Amaro et al., *Projected WIMP sensitivity of the XENONnT dark matter experiment*, Journal of Cosmology and Astroparticle Physics **2020** (2020) 31.

[51] D. Akerib, C. Akerlof, D. Akimov, A. Alquahtani, S. Alsum, T. Anderson et al., *The LUX-ZEPLIN (LZ) experiment*, Nuclear Instruments and Methods in Physics Research Section A: Accelerators, Spectrometers, Detectors and Associated Equipment **953** (2020) 163047.

[52] J. Aalbers, D. Akerib, C. Akerlof, A. A. Musalhi, F. Alder, A. Alqahtani et al., *First dark matter search results from the LUX-ZEPLIN (LZ) experiment*, Physical Review Letters **131** (2023) .

[53] R. Abbasi, M. Ackermann, J. Adams, J. Aguilar, M. Ahlers, M. Ahrens et al., *Search for GeV-scale dark matter annihilation in the sun with IceCube DeepCore*, Physical Review D **105** (2022) .

[54] D. Durnford and M.-C. Piro, *The search for light dark matter with NEWS-G*, Journal of Physics: Conference Series **2156** (2021) 012059.

[55] PICO Collaboration collaboration, *Dark matter search results from the PICO-2L* C_3F_8 *bubble chamber*, Phys. Rev. Lett. **114** (2015) 231302.

[56] C. Amole, M. Ardid, I. Arnquist, D. Asner, D. Baxter, E. Behnke et al., *Data-driven modeling of electron recoil nucleation in PICO* C_3F_8 *bubble chambers*, Physical Review D **100** (2019) .

[57] K. Fujii, Y. Endo, Y. Torigoe, S. Nakamura, T. Haruyama, K. Kasami et al., *High-accuracy measurement of the emission spectrum of liquid xenon in the vacuum ultraviolet region*, Nuclear Instruments and Methods in Physics Research Section A: Accelerators, Spectrometers, Detectors and Associated Equipment **795** (2015) 293.

[58] M. L. H. Eric W. Lemmon, Ian H. Bell and M. O. McLinden, *Thermophysical properties of fluid systems*, NIST Chemistry WebBook, NIST Standard Reference Database Number 69 (2023) .

[59] P. Di Gangi, *The xenon road to direct detection of dark matter at LNGS: The xenon project*, Universe **7** (2021) 313.

[60] M. Szydagis, N. Barry, K. Kazkaz, J. Mock, D. Stolp, M. Sweany et al., *NEST: a comprehensive model for scintillation yield in liquid xenon*, Journal of Instrumentation **6** (2011) P10002.

[61] L. Baudis, P. Sanchez-Lucas and K. Thieme, *A measurement of the mean electronic excitation energy of liquid xenon*, The European Physical Journal C **81** (2021) .

[62] J. Heise, *The Sanford underground research facility*, Journal of Physics: Conference Series **2156** (2021) 012172.

[63] J. Aalbers, F. Agostini, M. Alfonsi, F. Amaro, C. Amsler, E. Aprile et al., *DARWIN: towards the ultimate dark matter detector*, Journal of Cosmology and Astroparticle Physics **2016** (2016) 17.

[64] Hamamatsu Photonics K. K., *Photomultiplier Tubes: Basics and Applications*, 4 ed., 2017.

[65] Hamamatsu Photonics K. K., *R12699-406-M4 Flat Panel Type Multianode Photomultiplier Tube*, 2020.

[66] G. R. Araujo, L. Baudis, Y. Biondi, A. Bismark and M. Galloway, *The upgraded low-background germanium counting facility Gator for high-sensitivity γ-ray spectrometry*, Journal of Instrumentation **17** (2022) P08010.

[67] A. M. Brown, *Search for Elastic and Inelastic Dark Matter Interactions in XENON1T and Light Detection for XENONnT*, Ph.D. thesis, University of Zurich (2020).

[68] M. Diwan, *Statistics of the charge spectrum of photo-multipliers and methods for absolute calibration*, Journal of Instrumentation **15** (2020) P02001.

[69] M. Adrover, *A framework for analysing low illumination chargespectra of photomultiplier tubes*, [Online] Available on https://github.com/MaxiA04/pmt_gain_fitting (accessed: Nov. 2023) .

[70] P. Virtanen, R. Gommers, T. E. Oliphant, M. Haberland, T. Reddy, D. Cournapeau et al., *Scipy 1.0: Fundamental algorithms for scientific computing in python*, Nature **17** (2020) 261.

[71] R. Saldanha, L. Grandi, Y. Guardincerri and T. Wester, *Model independent approach to the single photoelectron calibration of photomultiplier tubes*, Nuclear Instruments and Methods in Physics Research Section A: Accelerators, Spectrometers, Detectors and Associated Equipment **863** (2017) 35.

[72] A. Bismark, *Comprehensive processing and analysis for photomultiplier tube characterization data*, [Online] Available on https://github.com/a1exndr/PMT_Analysis/ (accessed: Nov. 2023) .

[73] Y. van der Burg, *Characterisation of Hamamatsu R12699-406-M4 photomultiplier tubes for the DARWIN experiment*, Bachelor thesis, University of Zurich (2022) .

[74] L. Baudis, A. Behrens, A. Ferella, A. Kish, T. M. Undagoitia, D. Mayani et al., *Performance of the Hamamatsu R11410 photomultiplier tube in cryogenic xenon environments*, Journal of Instrumentation **8** (2013) P04026.

[75] P. Barrow, L. Baudis, D. Cichon, M. Danisch, D. Franco, F. Kaether et al., *Qualification tests of the R11410-21 photomultiplier tubes for the XENON1T detector*, Journal of Instrumentation **12** (2017) P01024.

[76] E. Aprile, J. Aalbers, F. Agostini, M. Alfonsi, F. D. Amaro, M. Anthony et al., *Physics reach of the XENON1T dark matter experiment.*, Journal of Cosmology and Astroparticle Physics **2016** (2016) 027.

[77] A. Manalaysay, T. M. Undagoitia, A. Askin, L. Baudis, A. Behrens, A. D. Ferella et al., *Spatially uniform calibration of a liquid xenon detector at low energies using* ^{83m}Kr, Review of Scientific Instruments **81** (2010) .